

## **GHRIS Instrument and Calibration Status: 1990-1993**

Stephen J. Hulbert<sup>1</sup>

### **Abstract**

The Goddard High Resolution Spectrograph is an ultraviolet spectrograph onboard the *HST*. While the instrument has been without the use of one of its two detectors due to hardware problems, the remaining detector has functioned well. This report provides a summary of the instrument and calibration status since launch.

### **I. Introduction**

The Goddard High Resolution Spectrograph (GHRIS) is a modified Czerny-Turner spectrograph onboard *HST*. GHRIS consists of seven gratings and four target acquisition mirrors all of which are mounted on a rotating carrousel. The gratings and mirrors are divided into two groups with each group having its own Digicon detector. The two groupings are known as Side 1 and Side 2. Side 1 can obtain spectra spanning a wavelength range from 1100 to 1700 Å; Side 2 detects from 1100Å to 3200Å. The high, medium, and low resolutions gratings have resolving powers of 80000, 25000, and 2000. Light from astronomical targets enters the GHRIS through one of two apertures—the large science aperture (LSA) is a square aperture 2.0 arc seconds on a side; the small science aperture (SSA) is also square but measures only 0.25 arc seconds on a side. The target acquisition mirrors are used to find and center targets in one of the two apertures of GHRIS.

### **II. Major Instrumental Changes**

During the first three years of operation, GHRIS has experienced several serious hardware anomalies, and Figure 1 shows a time line.

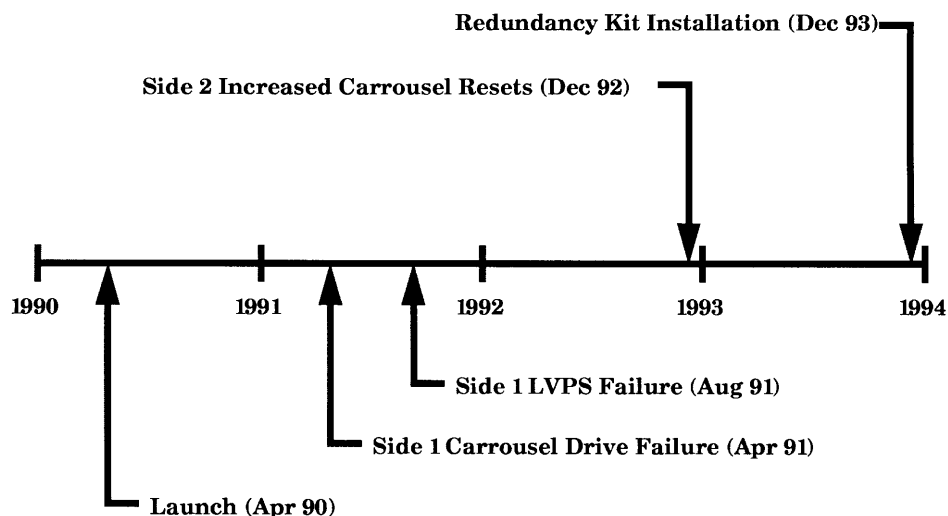
#### *Side 1 Carrousel Drive Failure*

Approximately one year after launch, GHRIS experienced a series of carrousel configuration failures that resulted in the GHRIS being safed. In each instance the carrousel failed to lock in its commanded position. The engineering symptoms were similar to a prelaunch problem with a loss of drive power to the carrousel motor and it has been concluded that a carrousel drive failure is responsible for the in-orbit behavior. GHRIS has redundant drive motors, fortunately, and changes in the commanding of GHRIS will permit the Side 1 activities to be driven by the Side 2 motor. This workaround will be tested as part of the Cycle 4 calibration activities.

---

1. Space Telescope Science Institute, Baltimore, MD 21218

Figure 1: Key GHRS Mechanical Events



### *Side 1 LVPS Failure*

A catastrophic failure in the Side 1 LVPS (low voltage power supply) forced observations with Side 1 to be halted in the summer of 1991. The failure, which has been traced to an intermittent contact within the LVPS, manifested itself by a failure of the science data formatter (SDF-A) which handles the data flow between the GHRS and the spacecraft. The real difficulty for GHRS is that communications from both sides are routed through Side 1. While it is possible for both sides to communicate with the telescope through Side 2, a change of this sort would also have an impact on the other instruments. As a workaround, as much of the electrical load on Side 1 has been removed as possible, and Side 1 science operations have been halted. Since the time of the failure there have been no problems obtaining data from Side 2. A permanent fix is planned during the December 1993 servicing mission; see section 2.4 for details.

### *Side 2 Carrousel Reset Events*

During December 1992 the rate of carrousel lock failures on Side 2 (sometime precipitating a loss of science data) increased from about 1 in 300 to 1 in 100. Since then the frequency has returned to nominal values. At this time there is no good hypothesis to explain this behavior.

### *GHRS Redundancy Kit Installation*

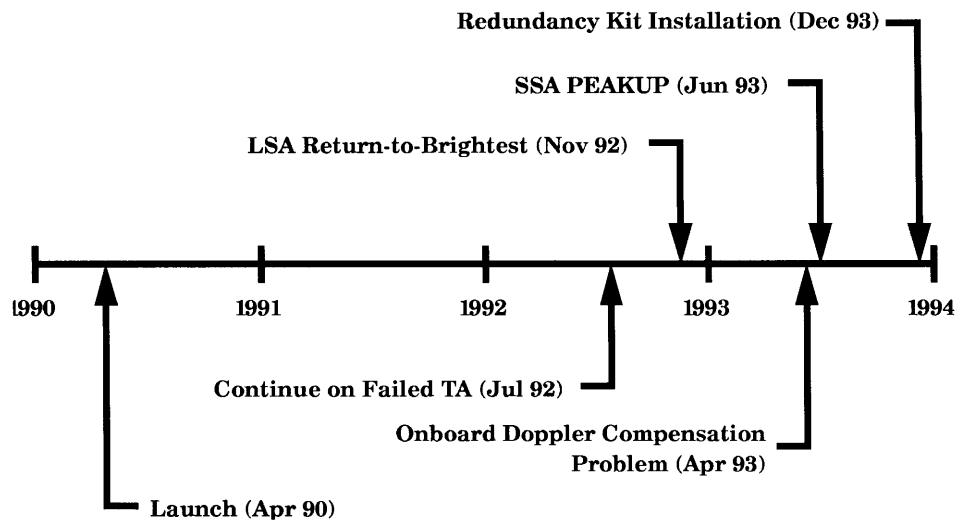
A permanent workaround to the communication problem will be installed on GHRS during the servicing mission in December 1993. A "redundancy kit" consisting of a set of relays will be installed at this time. This relay box will allow data paths to be

switched so that Side 2 is connected to SDF-A. Once the integrity of Side 2 is ensured, an attempt will be made to reactivate Side 1.

### III. Major Operational Changes

During the first three years of operation, GHRIS also has experienced significant operational changes, all but one of which improved the ability of the instrument to collect science data. Figure 2 shows a time line of major operational events for GHRIS.

Figure 2: Key GHRIS Operation Events



#### *Continue on Failed Target Acquisition*

Early use of onboard target acquisitions required an accurate knowledge of the brightness of the target. During the search phase of the target acquisition, a predefined series of slews was made in the shape of a square spiral. At each new slew point a flux measurement was made and compared to preset bright and faint limits. If the target flux was between the limits, the target was 'found'. If not, the search continued. The extended aberrated PSF often led, however, to the target brightness being outside the predicted limit. In this case not only did the target acquisition fail, but also the GHRIS flight software hung, with subsequent science observations being lost until the instrument could be recovered. This feature of the flight software was corrected such that observations continued in spite of the failed acquisition. While the science data obtained after such a failed acquisition may have been degraded, subsequent target acquisitions and spectra were able to be executed.

#### *LSA Return-to-Brightest Target Acquisition*

As mentioned, the extended PSF made it difficult to predict the brightness of a target (as seen by GHRIS). To increase the ease and reliability of target acquisitions, flight software and commanding changes were implemented for the target acquisition

process to return to the position of greatest flux in the spiral search phase of the acquisition. Since then, successful acquisitions and, subsequently, good spectra have become routine.

#### *Onboard Doppler Compensation Problem*

One operational difficulty was discovered in early 1993—a problem that had been present in the flight software since before launch. Since the *HST* orbits the earth with a velocity of about 7.5 km/sec, the spectra being obtained with GHRS may see a Doppler shift of up to 15 km/sec. To correct for this, the image of the spectrum is deflected by an amount equal to the Doppler shift such that the spectrum appears fixed with respect to the diode array which is recording the spectrum. The algorithm used for this correction made use of a table of sine values. Unfortunately, a bug in the code allowed the software to index outside of the table. In the one case where a maximum value was to have been found in the table, a value of zero was being found outside the table! So instead of producing a maximum shift, a zero shift was applied. Now for most observations this was not an obvious problem, a combination of the grating resolution and exposure time minimized the effects. However, in the case of high dispersion spectra obtained with short exposure times, one could actually see a doubling of spectral features corresponding to the different Doppler shifts applied. This insidious bug has now been repaired. The current solution does allow, however, for a cumulative error in the onboard Doppler compensation—while a new algorithm is being discussed, it is recommended that short exposures be made to minimize this problem. The OBSUM task in STSDAS identifies potentially corrupted data.

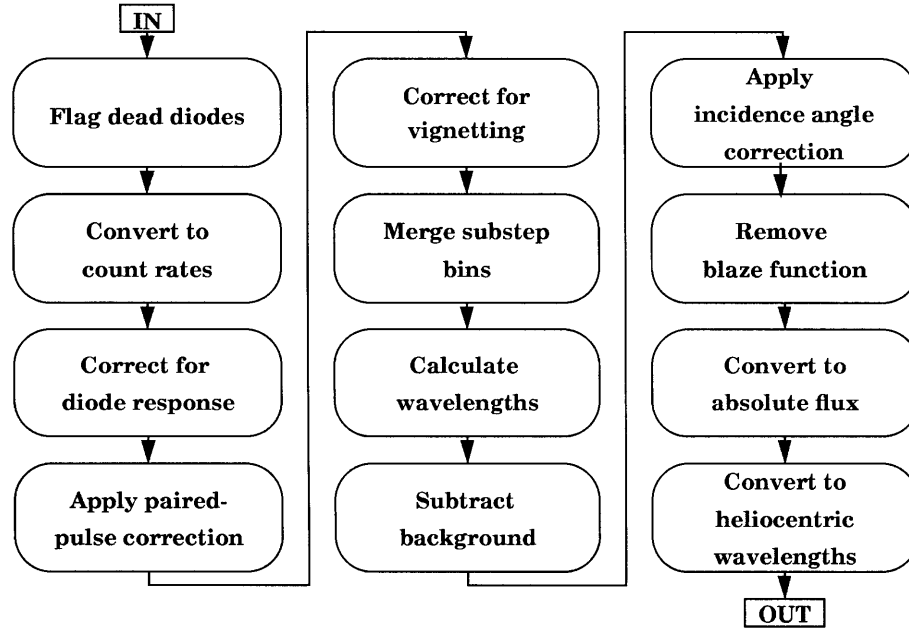
#### *SSA ACQ/PEAKUP Target Acquisition*

The aberrated PSF rendered useless the original algorithm that centers targets in the SSA. To circumvent this problem the double locate strategy evolved, whereby an object was centered twice in the LSA prior to a blind slew to the SSA. This technique was shown to be less than ideal—errors of 0.125 arc seconds were found for acquisitions using MIRROR-A2 mirror. Subsequently, flight software and commanding changes make it possible to use a new algorithm that is just a scaled-down version of the search algorithm used for onboard acquisitions in the LSA to function as a locate (centering) phase of SSA ACQ/PEAKUPS. This is working well for the A2 mirror and a fine-tuning is underway for acquisitions using the N2 mirror.

### **IV. Pipeline Calibration**

The calibration process has two basic goals: to assign net flux and wavelength values to each raw data point. The pipeline calibration takes the raw data stream from the spacecraft, parcels it up into raw data files, runs these files through a calibration process (called CALHRS), and finally produces a set of calibrated data files. The flux calibration has been constant to within 4 percent despite two secondary mirror moves. The wavelength scales have been relatively stable but show a systematic zero-point shift of about 1 diode since Side 1 was disabled. See Figure 3 for a flow diagram of the calibration processing steps.

Figure 3: GHRIS Calibration Processing



### *Flux Calibration*

The flux calibration consists of the following steps:

- **Flag Dead Diodes**—Identify known dead diodes to correct comb-added data values. Currently, Side 1 has diodes 268, 279, 451, and 493 disabled and Side 2 has diodes 110, 150, 279, 348, and 448 disabled.
- **Convert to Count Rates**—Divide by exposure time to convert from counts to counts/s.
- **Correct for Diode Response**—Correct for diode-to-diode variations.
- **Apply Paired-Pulse Correction**—Correct for deadtime in the detector electronics that results in nonlinear detector response at high count rates.
- **Correct for Vignetting**—Correct for low-frequency variations due to optical obscurations and the quantum efficiency of the photocathode.
- **Subtract Background**—Calculate background, smooth, and subtract from object spectrum. By default, the smoothing of the background is mean of the background data obtained. This mean background is then subtracted from the object spectrum.
- **Remove Blaze Function**—Correct for the low-frequency response along an order of the echelle grating.
- **Convert to Absolute Flux**—Convert corrected count rates to absolute flux. This conversion is based on ratio of the empirical count rates to a set of established fluxes of a spectrophotometric standard star.

### *Wavelength Calibration*

- **Calculate Wavelengths**—Calculate wavelengths based on carousel position of the grating being used. A zero-order correction is also made to account for thermal drifts.
- **Apply Incidence Angle Correction**—Correct the wavelength scale to account for the geometric offset between apertures. Since the default wavelengths are determined for the SSA, observations in the LSA (or spectral cal lamp apertures) must be adjusted.
- **Convert to Heliocentric Wavelengths**—Correct wavelength scale to account for the earth's motion around the sun.

## **V. Post-Pipeline Processing**

Some improvements can be made to the calibration of your data as your science requires and if you had planned your observations to obtain the additional necessary information.

### *Flux Calibration*

One correction missing from the pipeline calibration is the removal of high-frequency variations across the photocathode (i.e., the photocathode granularity). Since calibrated flat field files are not produced for GHRS, observers must use a strategy known as FP-SPLIT to plan (and execute) their observations. The FP-SPLIT technique obtains multiple spectra at slightly different carousel positions which provide measures of the intrinsic spectrum as well as the underlying photocathode structure. The POFSETS and SPECALIGN tasks in the STSDAS package can be used to combine the individual datasets into a single spectrum that has been effectively flat-fielded. Other papers in this proceedings describe methods for improving the fixed pattern noise.

### *Wavelength Calibration*

Default wavelengths are typically accurate to about 1-2 diodes. Up until now, a separate observation of the spectral calibration lamp was needed to permit the wavelength scale to be improved to better than a diode. The STSDAS task WAVECAL is used to make this improvement. At the present time, a new algorithm is being tested which should greatly improve the default accuracy, all but eliminating the need for additional spectral cal observations. Other papers in this proceedings describe improved methods for wavelength calibration.

# Line Spread Functions for GHRS Spectra with the LSA (Pre-COSTAR)

Ronald L. Gilliland<sup>1</sup>

## Abstract

The spherically aberrated point spread function of the *HST* provides input to the 2.0 arcsec LSA that is characterized by a sharp core and broad wings. The extended PSF wings contribute to a significant resolution degradation for spectra acquired through the LSA. The 0.25 arcsec SSA is matched in size to the spectroscopic resolution element; spectra taken in the SSA suffer a loss of throughput, but no significant resolution degradation. Through comparing spectra of a sharp-lined star acquired through both the LSA and SSA it is possible to derive the added line spread function (LSF) blurring of the LSA relative to the SSA. We report on empirical determination of the LSA spectral resolution degradation for three different wavelengths and four spectral elements of the GHRS.

## I. Introduction

Knowledge of the differential LSA to SSA line spread function is of use for any quantitative analyses of spectral features in LSA spectra. The LSF is required to separate intrinsic line broadening from that imposed by the spectrograph and telescope. Any deconvolution of LSA spectra requires good knowledge of the line spread function. Since the SSA line spread function is known separately (arises primarily from the diode sampling, see e.g., Gilliland et al. 1992), then deriving empirical and differential LSA to SSA line spread functions provides the full LSF for both of the GHRS apertures to high accuracy.

A technique for deriving the differential blurring function if the true (SSA) and degraded (LSA) spectra are available was presented in Gilliland et al. (1992).

The following equation relates the observed spectrum,  $\phi(x)$ , the assumed point-spread-function,  $P(y)$ , blurring the true spectrum,  $\psi(x)$ :

$$\phi(x) = \int \psi(x-y) P(y) dy \quad (1)$$

This equation may be solved for the differential blurring function, if the true (SSA in this case) and observed (LSA) spectra are available.

The solution of equation (1) for the differential LSF can be expressed as the least-

---

1. Space Telescope Science Institute, Baltimore, MD 21218

squares solution which minimizes  $\chi^2$  in the discretized case:

$$\chi^2 = \sum_i w_i \left( L_i - \sum_j P_j S_i \right)^2 \quad (2)$$

where  $L_i$  and  $S_i$  are the as-observed LSA and SSA spectra, and  $P_j$  is the desired differential LSF. Weights at the high S/N levels used here are set assuming Poisson statistics on the total number of counts per pixel. The extent of  $P_j$  is set by the projected size (in pixels) of the LSA. For the first order gratings this is 32, for the echelles a smaller number results because of internal demagnification. As discussed in Wahlgren et al. (1991) the extremely sharp-lined star  $\chi$  Lupi (HD 141556) is ideal for defining the LSF for all GHRS spectral elements.

The solution given by equation (2) gives mathematically correct LSFs, but sometimes fails to yield a physically reasonable solution. Our observations use quarter-stepped spectra in which adjacent points are not independent. When relating LSA and SSA spectra through equation (2) solutions for  $P_j$  would sometimes exhibit a sawtooth instability which could reach large amplitude with alternate points in the LSF taking (non-physical) negative values. A simple and quite effective solution is to add a 2nd difference penalty term to equation (2) that enforces smoothness on the  $P_j$ :

$$+ \sum_j wp (P_{j-1} - 2P_j + P_{j+1})^2 / (P_{j-1} + P_j + P_{j+1}) . \quad (3)$$

Choosing the relative weight contribution,  $wp$ , too small (or zero) allows a sawtooth instability on the  $P_j$ ; taking  $wp$  too large leads to a broader core than appropriate for the differential LSF ( $P_j$ ) and leads to an increase of the sum of equation (2). Through trial and error it was easy to find a value of  $wp$  that gave smooth  $P_j$  without degrading the fit of LSA and convolved SSA and LSF spectra. Solution for the  $P_j$  was obtained using a non-linear least-squares approach from Bevington (1969).

## II. Differential LSA to SSA Line Spread Functions.

Figures 1 and 2 illustrate the LSF solution — specifically for ECH\_B 2682Å paired LSA and SSA spectra acquired on 15 January 1993. Figure 1 shows the differential LSF that when convolved with the observed SSA spectrum yields the best match to the directly observed LSA spectrum. The LSA, convolved SSA and resulting difference spectra are shown in Figure 2. The rms of the difference spectrum is 1.7 percent of the mean intensity level. Given a S/N of about 100 per pixel for both the LSA and SSA spectra the difference error assuming only Poisson statistics should be ~1.4 percent. The derived LSF provides a near-Poisson limited result in this case. The minor excess noise could be attributed to residual flat-fielding errors from the FP-SPLIT solutions and possibly intrinsic changes in the stellar spectra.

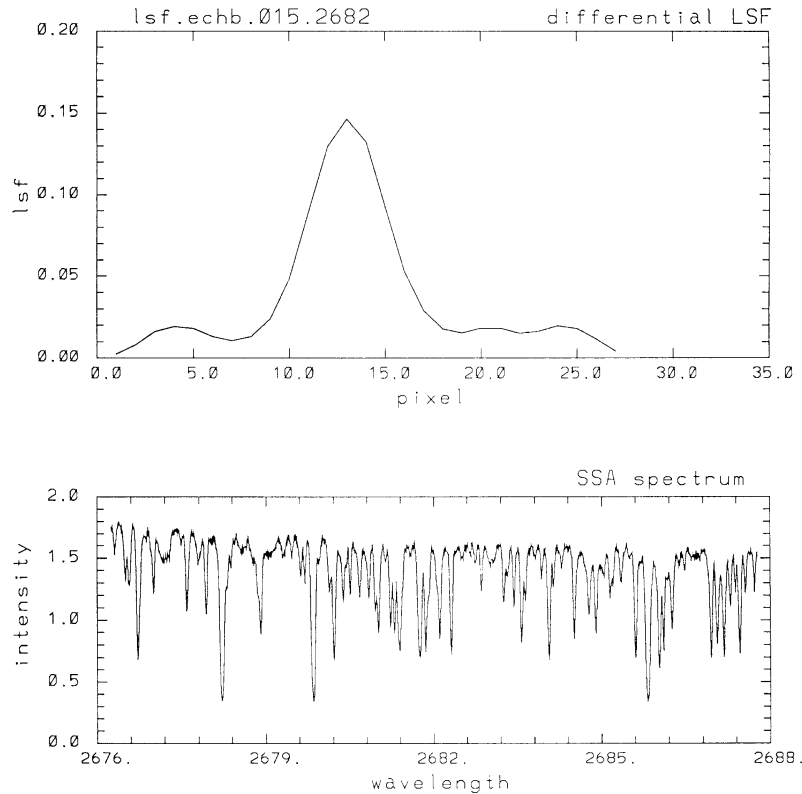


Figure 1: Differential LSF solution for ECHB data at 2682Å from 15 January 1993 is shown in the upper panel. Lower panel shows the observed SSA spectrum.

The Cycle 2 observations of CAL/HRS 3372 conducted on 15 Jan 1993 and 19 Feb 1993 gave good input to deriving differential LSA to SSA LSFs for the following wavelength-spectral element combinations: G160M—1360Å, G160M—1860Å, G200M—1860Å, G270M—2680Å, ECH\_B—1868Å, and ECH\_B—2682Å. The LSFs for these six cases are shown in Figure 3.

### III. Full LSA Line Spread Function.

All of the above discussion was for the added blurring that results only from the large size (2.0 arcsec) of the LSA coupled with the spatial extent of light over the aperture. If one wishes simply to know the total LSF for the LSA (e.g., the observed profile given a spatial and spectral delta function source), then the intrinsic blurring of the spectrograph must be taken into account. The intrinsic spectrograph LSF may be referred to as the LSF of the SSA. Given the derived differential LSA to SSA LSF, the full LSA LSF is just the convolution of this differential LSF and the LSF of the SSA. Gilliland et al (1992) argued that the SSA line spread function could be well represented by a Gaussian of ~3.75 pixels FWHM (the Echelle LSF is similar but with slight additional wings).

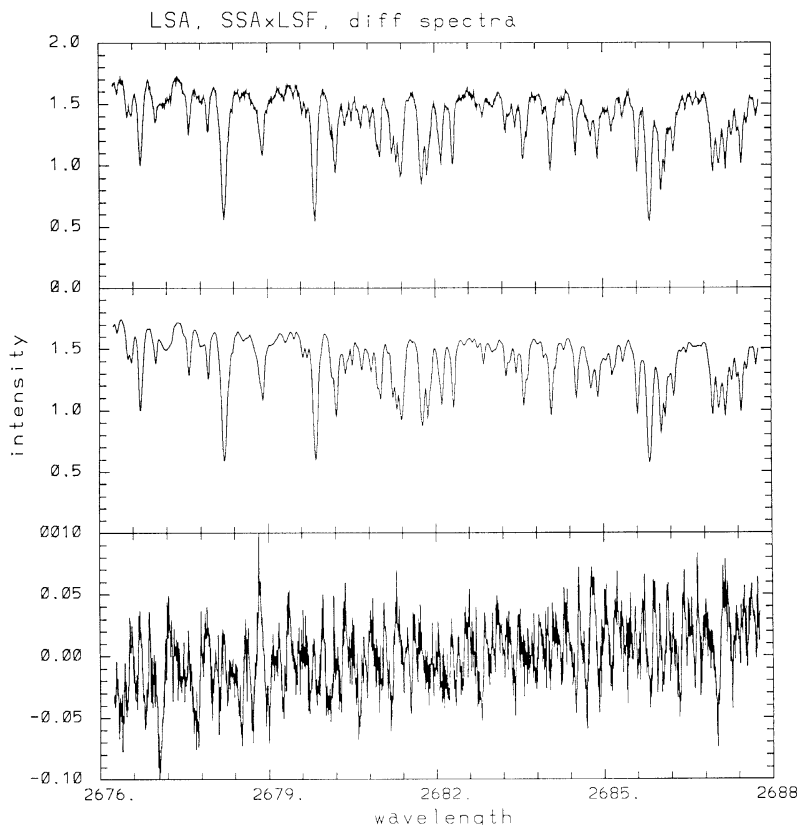


Figure 2: Upper panel shows the observed LSA spectrum of 15 January 1993. The middle panel shows the SSA spectrum after convolution with the LSF which should closely reproduce the LSA observations. Bottom panel is the difference spectrum showing errors only a little larger than expected from Poisson statistics.

#### IV. Discussion

By observing a sharp-lined stellar spectrum in both the LSA and SSA of the GHRS we have been able to reliably determine the large aperture differential line spread function which is assumed to represent the spatial PSF (contracted to one dimension along the spectrograph dispersion) at the aperture. The first order grating LSFs exhibit only minor changes with wavelength. There is no indication of a significant difference between the G160M and G200M LSFs at the common wavelength checked. Little difference is seen between these LSFs, and those derived separately using early 1991 data.

The ECH\_B LSFs show significant differences at the two wavelengths. From comparison with a 1991 measurement it appears that the difference depends on position within an order ( $m\lambda$ ). At  $1868\text{\AA}$  ( $m\lambda$  8 percent below blaze peak) the internal demagnification in the echelle mode results in an LSF 23 pixels (70 percent of first order case) wide. At  $2682\text{\AA}$  (more relevantly at  $m\lambda$  of 5 percent above blaze peak) the LSF is 27 pixels (82 percent of the first order case) wide.

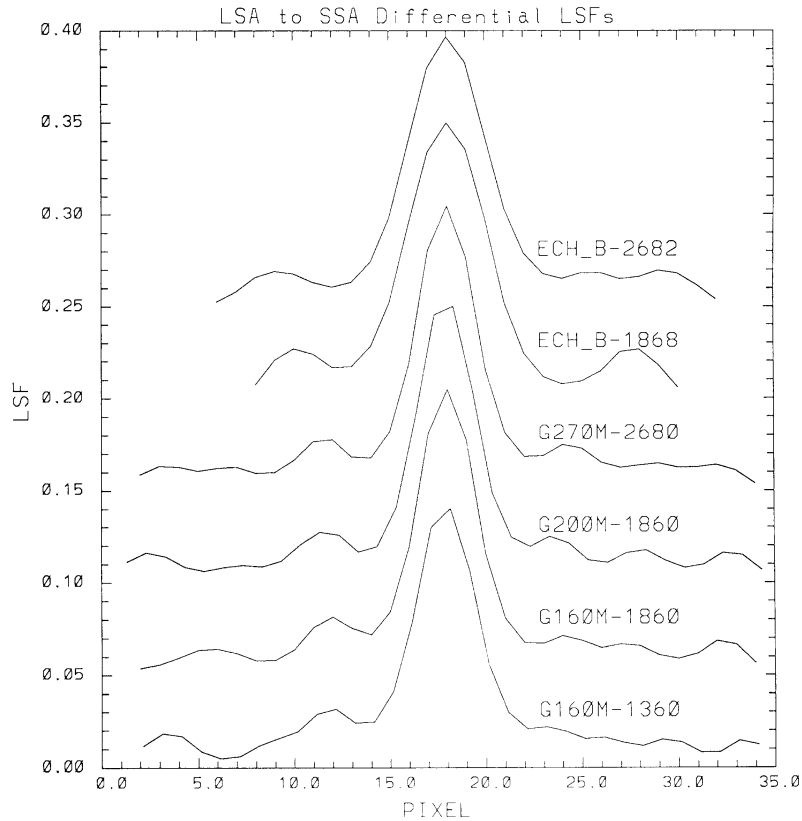


Figure 3: Differential LSFs (LSA to SSA) for the several wavelength-element combinations calibrated in 1993. LSFs for the first order gratings show only minor differences. The two echelle observations show significant differences; probably correlated with  $m\lambda$ .

The line spread functions derived for this report should be of use for studies that require line profile information and for deconvolution of LSA spectra. A more complete presentation of results may be found in the GHRS Instrument Science Report 055. The LSFs shown in Figure 3 should be used for GHRS data acquired at any time prior to the use of COSTAR.

## References

- Bevington, P.R. 1969. *Data Reduction and Error Analysis for the Physical Sciences*, (New York: McGraw-Hill)
- Gilliland, R.L., Morris, S.L., Weymann, R.J., Ebbets, D.C., and Lindler, D.J. 1992, PASP, 104, 367
- Wahlgren, G.M., Leckrone, D.S., Shore, S.N., Lindler, D.J., Gilliland, R.L., and Ebbets, D.C. 1991, ApJ, 377, L41

## **GHRM Photocathode Blemishes: Discoveries Lurking in the Spectrum**

Glenn M. Wahlgren<sup>1</sup>, Jennifer L. Sandoval<sup>1</sup> and Don J. Lindler<sup>2</sup>

### **Abstract**

Blemishes and irregularities in the photocathode and window materials of the GHRM digicon detectors produce spurious features that are a source of noise in the spectrum. An iterative computational technique is applied to GHRM data obtained with the FP-SPLIT option to create a granularity vector that represents the fixed pattern noise of the observation. At signal-to-noise levels less than 100 the granularity vector is used to detect and remove blemishes in a data set of first-order grating spectra of the bright star Sirius-A.

### **I. Nature of the Problem**

Congratulations! You were awarded *HST* observing time to obtain spectra with the Goddard High Resolution Spectrograph (GHRM). The data was acquired in a routine fashion and your data tapes have arrived. You can match the STScI supplied reduced data files with your theoretical spectrum, or, if you are ambitious you first re-reduce the data with software obtained from STScI or the GHRM IDT. Either way, the data is reduced in a rather straightforward, cookbook manner. Comparison of modelled data with the observation reveals a rather deep unidentified feature in the observation. You feel you may have discovered 'cathodium,' because although you have followed each reduction procedure as prescribed you have not inspected the intermediate-step data products.

The ultraviolet spectrum of most astronomical sources is difficult enough to understand without having to worry about features that in reality do not exist. However, that is precisely what one needs to do with any GHRM spectrum before one can feel confident about its interpretation. There are several ways in which undesirable discrete features and distortions can arise in the data: individual diode response (both high and low), sleaks, blemishes, or poor doppler compensation correction. In this paper we illustrate the effect of photocathode blemishes on the spectrum; their detection and removal.

### **II. GHRM Photocathodes and Blemishes**

The GHRM is comprised of two separate detector and electronics chains, or sides, that are essentially different only by the coatings of their photocathode (pc) windows. Each pc active area is 18 x 26 mm in size, and accommodates the 25 mm length of the

1. Computer Sciences Corporation, Code 681, GSFC, Greenbelt, MD 20771

2. Advanced Computer Concepts, Code 681, GSFC, Greenbelt, MD 20771

diode array at the opposite end of the detector assembly. The side 1 pc window is a 4 mm thick piece of lithium fluoride (LiF) with a cesium iodide (CsI) photocathode. The side 2 pc window is a 3 mm thick magnesium fluoride ( $\text{MgF}_2$ ) window with a cesium telluride (CsTe) photocathode. Side 1 sensitivity allows it to be most efficient between 1050 – 1700 Å and is associated with the use of the G140L and G140M gratings and echelle-A, while side 2 is sensitive over the entire 1100 – 3300 Å range and utilizes the G160M, G200M, and G270M gratings and echelle-B for science operations. Photons directed from one of the gratings on the carousel impinge upon the associated pc window and liberate electrons that are then directed to the diode array by the magnetic fields of the detector. The pc location sampled by a diode is a function of the specified grating and wavelength, as well as a variable thermal and geomagnetic spacecraft environment. Therefore, two similar observations with the same specified grating and wavelength may not sample the same location on the pc. GHRIS instrument descriptions at various levels of complexity can be found in TePoel (1985), Cushman, Ebbets, & Holmes (1986), Ebbets (1992), and Soderblom (1993).

Photocathode blemishes are, in part, a natural result of the physical and chemical properties of the materials employed and the technology that is used to construct optical components. The blemishes are localized physical deformities in the pc material, often referred to as scratches or digs, that are registered as a deficiency of counts by elements of the silicon diode array. They are a subset of the more generically termed fixed-pattern noise (fpn) pc window related response deficiencies which affect the spectrum over a larger area of the pc window. The fpn essentially limits the effective spectral signal-to-noise level at high counts. Cardelli (this volume) discusses fpn and its removal from GHRIS spectra for the case where high count totals are obtained. However, at S/N levels that are limited by photon statistics the low-level fpn will not be evident. The impression should not be formed that high count totals are required for the identification and removal of spurious spectral features. The strong discrete blemishes will still be evident at S/N levels under 100 and can be removed.

Several processes can affect the creation and evolution of blemishes and fpn. Among them:

- Humidity has been found to decrease the transmittance of LiF windows, particularly below 1600 Å (Patterson & Vaughn 1963). The transmittance loss is due to a surface film formed on the crystal by chemical reaction products of  $\text{H}_2\text{O}$  with LiF. Tests show that after an initial throughput loss has developed, exposure to vacuum conditions accelerates the loss. Woodruff (1978a) has cautioned that in-orbit (vacuum) exposure of the windows should be kept in mind during the GHRIS calibration phase. The limited use of the GHRIS side-1 prior to the *HST* servicing mission makes it imperative that its potential use in the post GHRIS-Redundancy Unit environment allow for proper re-calibration and continued sensitivity monitoring.  $\text{MgF}_2$  windows, such as that on side-2, have not been found to be affected by humidity.
- Crystal flaws can contribute to variations in transmittance over the surface of the window. Cleaved surfaces also result in a certain amount of scattered light. The GHRIS windows are a dual plane window design with polished surfaces. Sleaks can result from the polishing process.

- Surface scratches and digs, on both the window and pc sides, can result from handling during the manufacture and assembly phases. Pre-flight tests (Eck 1983) with detector 2 observed a few digs, of size 400-600  $\mu\text{m}$  x 600  $\mu\text{m}$ , after reassembly of the unit following design changes. Scratches that cover a full diode width can either degrade or make unusable the particular diode response that samples that portion of the pc (Woodruff 1978b). Large digs, such as mentioned above, can affect the response of up to eight diodes. The presence of particulate contamination will likewise obscure specific diodes.

Pre-flight testing of spare digicons from the GHRS tube flight build were conducted to test pc quantum efficiency variations (Beaver & Greenwell 1989). The long shelf-time of the detectors, forced by *HST* launch delays, had raised concerns of sensitivity loss. Two spare digicons, with pc characteristics of the two flight units, were tested and found not to show sensitivity loss that would be indicative of a generic problem with the flight build. An additional CsTe pc digicon, referred to as Engineering Model 1 (EM1) and not of the exact flight build design, did show a significant drop in sensitivity over the time period 1980 - 1987. While it is only speculated as to why the EM1 unit suffered a sensitivity loss, it does point out that digicon tubes can develop individual problems.

### III. Blemish Removal

Removal of pc blemishes can be incorporated as an additional step in the normal data reduction procedure. The assumption, however, is that the data have been obtained with the GHRS FP-SPLIT<sup>1</sup> option. The FP-SPLIT option forces the observation to be broken into either 2 or 4 subexposures, where the GHRS grating carousel has been moved a slight amount between subexposures in order that each diode of the array samples a slightly different position of the pc. The effects from low-level fpn can be reduced nominally by a factor of two by shifting and coadding when four individual FP-SPLIT subexposures are available. The larger blemishes can appear as either 2 or 4 spectral absorption features that are slightly displaced from each other, by the wavelength equivalent of one carousel step, when all subexposures are overplotted in wavelength space. For all work regarding removal of fpn and blemishes we recommend that the observations be obtained using FP-SPLIT= 4.

We have employed a technique (Lindler 1991) that iteratively computes the fpn pattern and corrects for fpn in the source flux as the solution of an over-determined non-linear system of equations. The input data are multiple spectra aligned by shifting in the dispersion direction, with the assumption of the same fpn pattern. The procedure involves:

- initially setting the fpn (granularity) vector elements to unity
- correct (divide) each raw observation by the granularity vector
- compute a new flux array by shifting and averaging the corrected raw observations

---

1. see Proposal Instructions.

- compute a new granularity vector for each raw observation using the new flux array
- compute a new granularity vector by averaging the individual granularity vectors.

This process, from the second step, is iterated until a convergence criterion is met. Final solutions may display 'ringing' if a nearly constant value for the spectrum offsets is used, or spectral features are not perfectly registered. However, the GHRM grating carousel tends to produce unequally offset spectra from the FP-SPLIT option. In reality, limitations to the technique are imposed by spatially variable fpn, near equally spaced offsets, and the occurrence of near equally spaced source absorption features. Any will increase the noise level in the iterated flux and granularity vectors. The technique is particularly successful at high S/N levels in removing fpn from the flux spectrum (Cardelli, this volume). At lower S/N, where counting statistics dominate the errors, this technique produces signal level dependent errors that are larger than those from the simple shift and coadd technique, and should therefore be used only to make use of the granularity vector to locate blemishes to be masked from the spectrum.

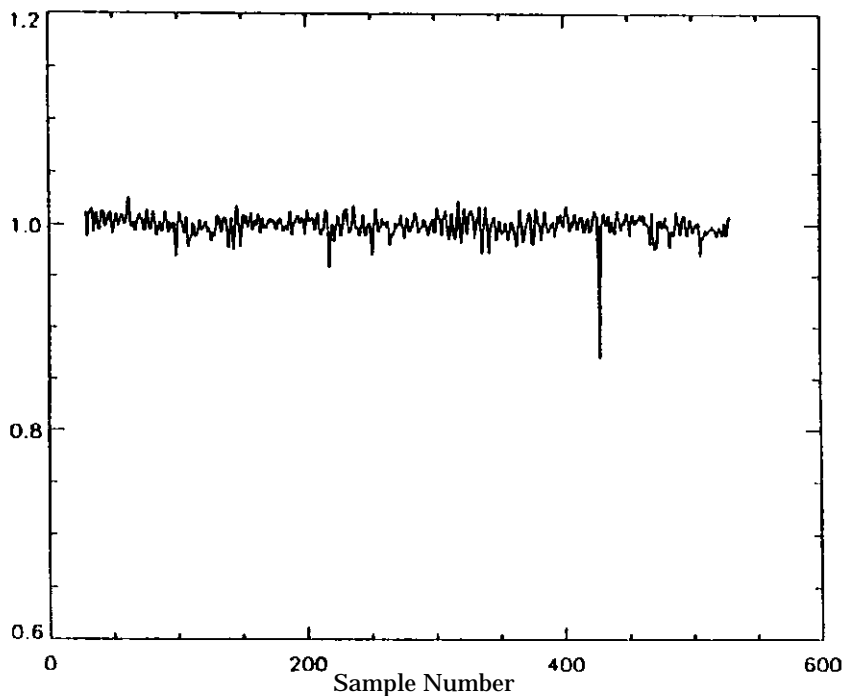


Figure 1: Granularity vector. Note obvious blemish near sample position 430.

Visual inspection of the iteration program granularity vector (Figure 1) allows the user to select the level of blemish that is required for data interpretation. For each pc a coordinate grid is constructed having grid spacings of 50  $\mu\text{m}$  in both the X (*sample*) and Y (*line*) dimensions. The origin of the grid is the upper-left corner of the pc. Simple linear relations have been calibrated that relate the commanded deflections in both X and Y coordinates to *sample*, *line* values. The *sample*, *line* values for an

observation can be computed using information extracted from the observation Science Header Packet. In Figure 1 it is evident that a blemish exists near *sample* position 430. Interactive techniques, such as our use of IDL, can be used to measure the *sample* range from such a plot. We have assumed that the blemish extends by  $\pm 1$  unit in *line* position. For each blemish the *line* and *sample* ranges are determined and a blemish table can be constructed for individual observation data sets. It is important that each blemish be assigned an epsilon (data quality flag) value that is appropriate for its severity. In GHRM IDT data reduction software, a value of 150 for the *badepts* parameter corresponds to a blemish that is at most 5 percent deep, and a value of 180 for depths greater than 5 percent.

To remove the effects from blemishes the GHRM spectrum is first reduced to produce the individual wavelength and flux calibrated FP-SPLIT spectra. Running the IDL routine HRSMERGE (available from the GHRM IDT), with optional parameter *badepts* set to the value of the epsilon level that needs to be removed, will align and coadd the FP-SPLIT segments, excluding the *sample/line* ranges designated in the specified blemish table. One drawback is that the S/N level for the affected data points will be reduced, by a factor of 1.154 in the case where three of four FP-SPLIT spectra are useful.

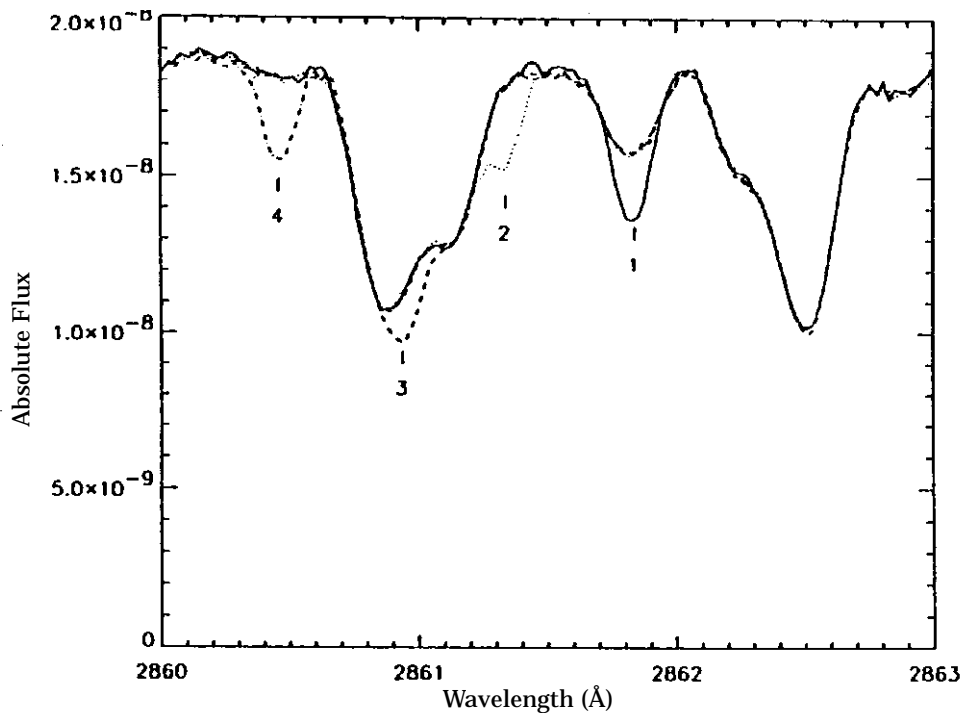


Figure 2: Overplots of individual FP-SPLIT spectra of Sirius with locations numbered of spectral features resulting from the blemish at *sample* 430.

The effect upon the spectrum of the blemish near *sample* position 430 is shown in Figure 2. The 3 Å of data presented represents approximately 7 percent of the observation wavelength range. Each of the four individual FP-SPLIT segments is plotted using different linestyles and the corresponding four spectral features resulting from the single blemish are numbered. For this blemish the additional

features are obvious in the FP-SPLIT segments but not necessarily in the final merged spectrum. Figure 3 presents the final merged (coadded) spectra both with (solid line) and without (dashed line) removal of the blemish. For FP-SPLIT segments 1, 2, and 3 an analysis of the uncorrected spectrum might produce increased abundances for the contributing elements or lead to concerns regarding their oscillator strengths. FP-SPLIT segment 4 might lead to the identification of an elemental species that does not exist in the star. Other blemishes will produce spectral features that are more or less obvious in the individual FP-SPLIT segments than those presented here and it should be remembered that searching the final merged spectrum will not necessarily uncover these features. *Observations taken without the FP-SPLIT option provide no information for identifying and removing blemishes.*

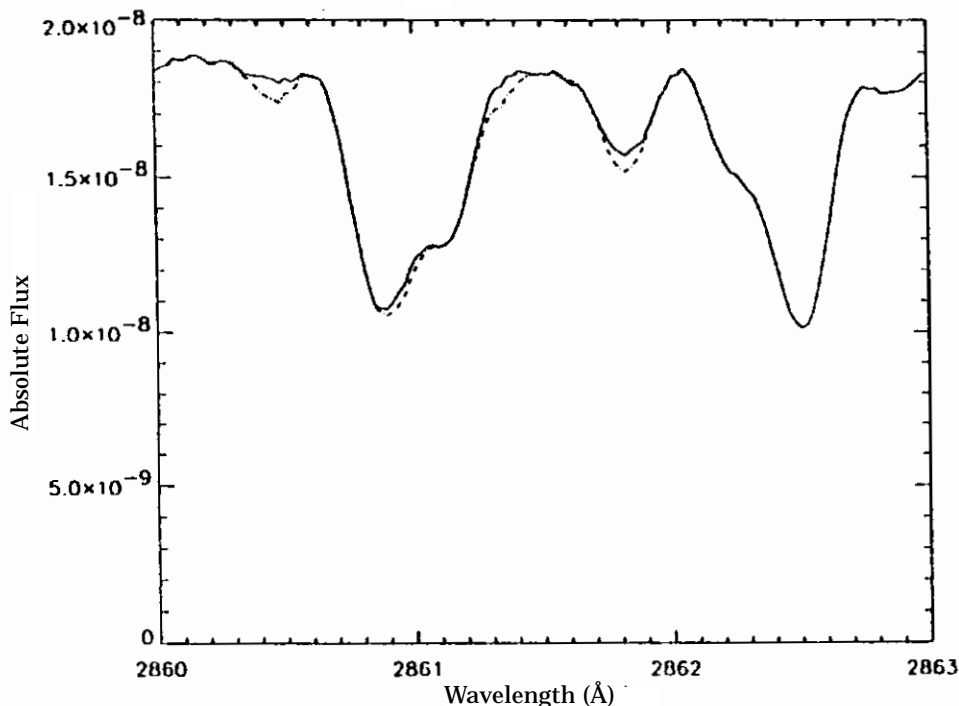


Figure 3: Coadded spectra for cases where blemish has (solid) and has not (dashed) been removed.

#### IV. Discussion

In the OV/SV planning phases for GHRM calibration, tests were constructed that would collect data to allow for a partial mapping of the two GHRM photocathodes. This proposal was never executed and after early observations were vigorously analyzed (Cardelli 1991) it was recommended that the use of FP-SPLIT will allow for the removal of detector effects (Ebbets 1992). A first post-launch mapping of the photocathodes was constructed by Robinson (1991) using Science Verification flux calibration spectra of the bright early-type star  $\mu$  Columbae (O9.5 V), obtained with the first-order gratings. Blemishes were detected by comparing the overlap regions of contiguous spectra. The  $\mu$  Col calibration data were not obtained using FP-SPLIT and so can not be analyzed by the iterative scheme outlined in section 3. The detection of blemishes in the  $\mu$  Col data set is not considered complete.

The recently acquired first-order grating spectral atlas of Sirius-A (Wahlgren et al. 1993) provides a large data set that can be used to supplement the earlier work of Robinson. The Sirius spectra were obtained with the FP-SPLIT = 4 option and have been searched for blemishes with the iterative technique discussed above.

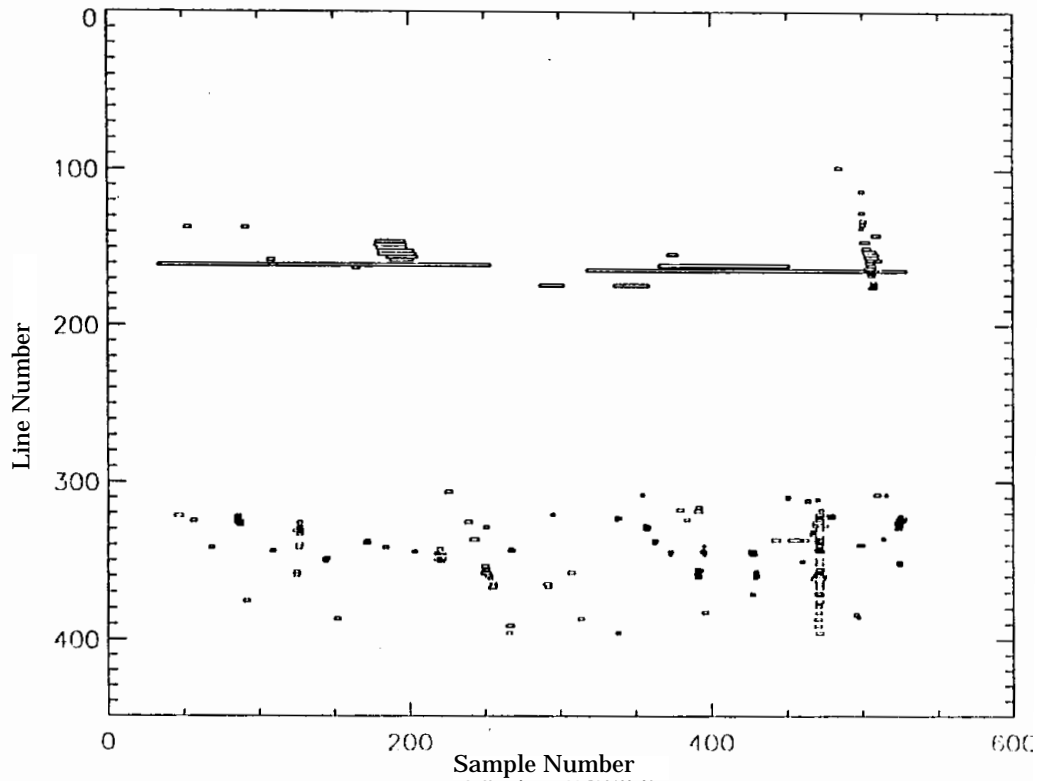


Figure 4: Areal coverage of GHRs photocathodes by catalogued blemishes.

Figure 4 presents all of the catalogued blemishes, from both data sets. The entire range of a pc is represented by the *line* and *sample* ranges plotted. The figure is actually a composite from both detectors. Data plotted in the *line* range of 100 - 200 are from the G140L and G140M gratings of side 1 while the data in the *line* range of 300 - 400 are from the side 2 gratings G160M, G200M, and G270M. Echelle formats for each detector cover the entire pc format but the first-order gratings are restricted. The limited amount of side 1 data originates only from the  $\mu$  Col calibration observations. The long horizontal features identified with detector 1 are difficult to refer to as blemishes, but do not appear to result from simple vignetting. Both detectors show a vertical feature, likely to be scratches, at high sample numbers. Smaller extended features are also noticeable.

Figure 5 expands the detector 2 data and distinguishes between  $\mu$  Col (boxes) and Sirius (stars). The symbol sizes are approximately the same as the area boxes in Figure 4 and are plotted for the center of the *line*, *sample* ranges. Many features were

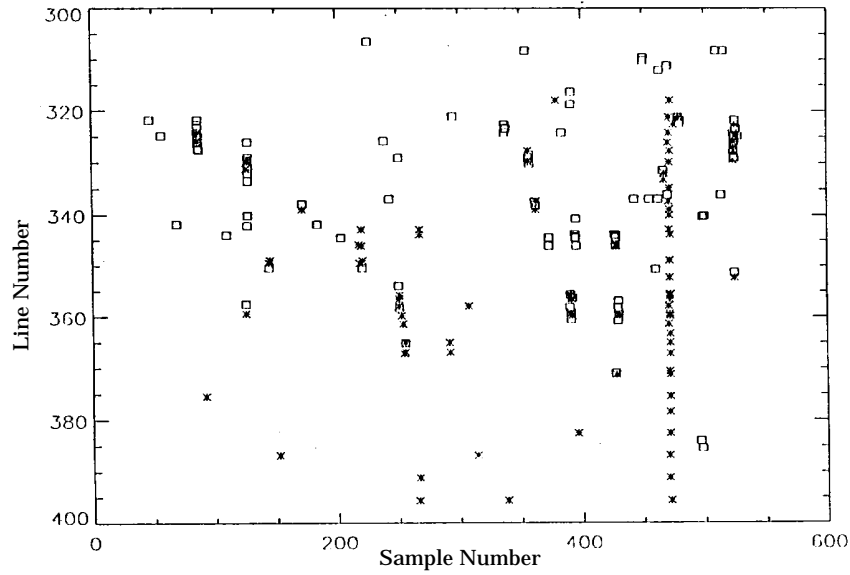


Figure 5: Detector 2 blemishes obtained from  $\mu$  Col (squares) and Sirius (stars) data sets.

observed by both data sets, and tend to produce most of the deepest features in the iterative-scheme output. It is also clear that the two data sets do not have full overlap. However, there are features that were observed in only one of the data sets and can not be explained by various selection effects. It is possible that pc blemishes evolve with time. For this possible reason alone the construction of photocathode maps for the removal of fpn features is not feasible.

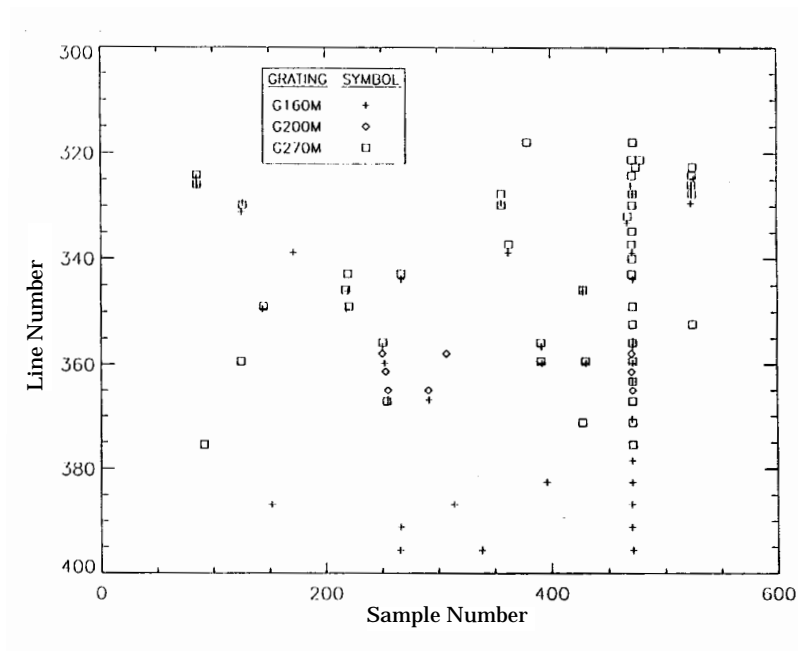


Figure 6: Sirius data set blemishes broken down by grating.

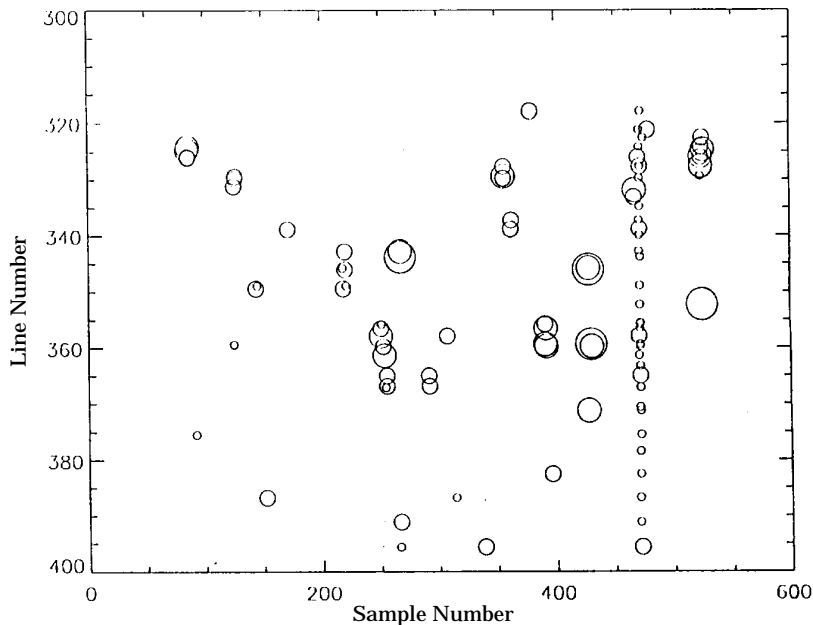


Figure 7: Sirius data set blemishes. Circle size depicts blemish depth (1-4, 5-10, 10-20, and 20-40 percent) in granularity vector, not necessarily photocathode blemish size.

Figures 6 and 7 present information regarding the Sirius data set alone. The extent of the separate gratings is presented in Figure 6, showing the overlap on the pc for the three gratings and the fact that, for the most part, where *line* positions for different observations/gratings are available they tend to identify the same blemish. For these same blemishes Figure 7 illustrates their approximate strengths, or feature depths in percent from the continuum level, in the iterative scheme output. The long vertical scratch-like feature located near *sample* number 470 is not strong and may explain why it was not identified in the  $\mu$  Col data set.

## References

- Beaver, E., & Greenwell, D., 1989, BALL System Engineering Report (SER) GHRS-DET-130, 'Recent GHRS Quantum Efficiency Data'
- Cardelli, J., 1991, BALL SER GHRS-SV-113, 'Detailed Analysis of Photocathode FPN Granularity, S/N Limits, and Weak Line Detectability Using the GHRS Detector Systems'
- Cushman, G., Ebbets, D., & Holmes, A., 1986, 'Pre-Launch Calibration Report for the High Resolution Spectrograph for the Hubble Space Telescope,' HRS-2176-051, BALL Aerospace Systems Group
- Ebbets, D., 1992, 'Final Report of the Science Verification Program for the Goddard High Resolution Spectrograph for the Hubble Space Telescope,' BALL Aerospace Systems Group
- Eck, H., 1983, BALL SER DET-103, 'D2-MkIII Performance Summary'
- Lindler, D.J., 1991, BALL SER GHRS-SV-102, 'Removal of FPN from FP-SPLIT Observations'
- Patterson, D.A., & Vaughn, W.H., 1963, JOSA, 53, 851

- Robinson, R.D., 1991, BALL SER GHRIS SV-080, 'Small Scale Imperfections in the GHRIS Detectors and Their Influence on Observations'
- TePoel, H.E., 1985, 'SI System Description and User's Handbook for the High Resolution Spectrograph for the Hubble Space Telescope,' HRS-2176-050C (SE-01), BALL Aerospace Systems Group
- Soderblom, D.R., 1993, 'Instrument Handbook for the GHRIS,' (STScI:Baltimore)
- Wahlgren, G.M., Johansson, Se., Kurucz, R.L., & Leckrone, D.S., 1993, BAAS, in press, 'A GHRIS/*HST* Spectral Atlas of Sirius-A'
- Woodruff, R., 1978a, BALL SER OPT-023, 'Data on Environmental Effects on LiF Crystals' Woodruff, R., 1978b, BALL SER OPT-013, 'Digicon Window Optical Constraints: Thickness, Polish, Scratch-Digs'

# **An Assessment of the Pipeline Wavelength Calibrations for the First-Order Gratings of the GHRS in Cycle 2<sup>1</sup>**

David R. Soderblom<sup>2</sup>, Lisa E. Sherbert<sup>2</sup> and Stephen J. Hulbert<sup>2</sup>

## **Abstract**

This *Report* is based on several executions of calibration proposal 4067 and shows that the default wavelength scale provided by the pipeline data reduction system has not changed significantly with time. WAVE exposures as part of user observations can, however, improve the zero point for each observation, as can use of Spectrum Y Balance (SPYBAL) exposures.

## **I. Introduction**

Users of the GHRS depend on the wavelength scale to draw astrophysical conclusions from their observations. Many users rely on the default wavelength scale that is provided by the pipeline data reduction system (PODPS). Other observers may obtain exposures of the wavelength calibration lamp just before they observe a celestial object, but that is often done only to check the zero point of the wavelength scale rather than to obtain a full wavelength solution from scratch.

The STScI GHRS team monitors the accuracy and repeatability of the wavelengths inferred from the instrument. The last report on this subject was prepared by J.R. Walsh in June 1992, and he concluded that the pipeline reductions provided a satisfactory calibration and that there was no need to change the constants in use at that time. In this report we extend that analysis further but reach essentially the same conclusion. However, at the same time the calibrations clearly point to several significant correlations between the wavelengths and other quantities. Procedures are being put in place to enable users to improve upon the default wavelength scales to extract wavelengths and velocities that are virtually as good as if calibration exposures had been obtained, see the companion report.

## **II. Calibration Methodology**

In Cycle 2 the GHRS wavelength calibrations for the first-order gratings of Side 2 were executed as proposal 4067. Several exposures at standard central wavelengths were obtained for each of the gratings (G160M, G200M, and G270M). Each proposal was run internally and so required no on-target *HST* time. Each was executed approximately every four months.

---

1. Originally published as GHRS Instrument Science Report #52

2. Space Telescope Science Institute, Baltimore, MD 21218

### **III. Observations and Data Analysis**

The data sets which were used in this analysis are listed in Table 1. Each file is an ACCUM accompanied by a SPYBAL, using aperture SC2. There are 6 settings observed for each of the three Side 2 first-order gratings: G160M, G200M, and G270M. We also examined some observations made in Cycle 1.

In a first analysis, the NOAO.ONEDSPEC task IDENTIFY was used to find the wavelengths of the lines and to fit a fourth order legendre polynomial to each data set. The rms residuals of the fits were low. However, in order to use IDENTIFY the data had to be RESAMPLED, which can introduce small errors in the centering of a line, since RESAMPLE changes the flux at some points in order to make the wavelength scale linear. Therefore the data were reduced with the HRS task WAVECAL.

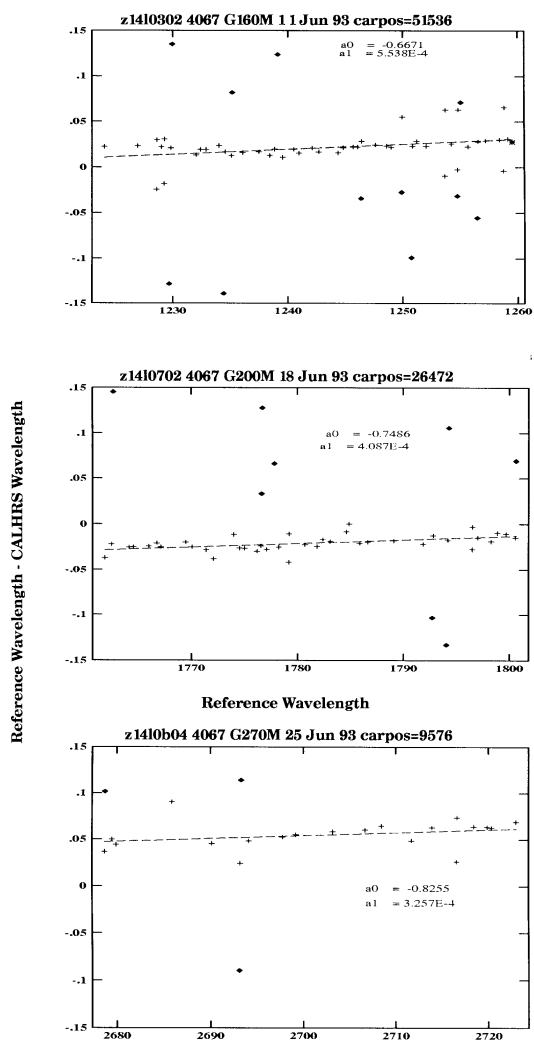
WAVECAL first does a cross-correlation to find the features from a set of reference (vacuum) wavelengths (Reader et al. 1990), and then performs a linear regression to determine the dispersion coefficients. In this analysis we calculate the difference between the reference wavelengths and the CALHRS wavelengths from the default dispersion solution. A line is then fitted to that difference as a function of the reference wavelengths.

We found that certain lines at each grating setting had consistently deviant positions relative to their reference wavelengths; these were ignored in our analysis. After doing so, we found rms scatter about a mean relation to be that listed in columns (3) and (4) of Table 1. Examples of these analyses are shown in Figures 1–3. The way in which the measured wavelengths deviate from laboratory wavelengths is characterized by three quantities. The first is the rms scatter just mentioned, which measures random error and which may also include a component of error in the lab wavelengths themselves. The second quantity is the mean deviation (column (5) of Table 1), which represents a zero-point error in the wavelengths. The final quantity is the slope of the fit, which measures the error in the wavelength scale (or dispersion).

### **IV. Discussion**

The rms values in Table 1 are typically less than 1 km/sec, and often below 0.5 km/sec, with the shortest wavelengths being exceptions. Such scatter is much less than any of the systematic components of wavelength differences and shows that random error and errors in the lab wavelengths do not contribute significantly to uncertainty in velocities derived with the GHRS.

The slopes of the fits are also small, although they deviate from zero in a statistically significant way. For the typical 40 Å wide bandpass of a GHRS medium-resolution spectrum, a slope of, say, 0.0004 translates to errors in the wavelength scale of 8 mÅ of the ends relative to the middle. This is about twice as large as the rms scatter but still well within the specifications for the default wavelength scale. We expect to work on improvements. As illustrated in the Figures 4–9, the changes in slope are uncorrelated with time but are related to temperature within the GHRS. Allowing for the temperature dependence of the slope (wavelength scale) should allow us to remove the dominant component that changes from exposure to exposure.

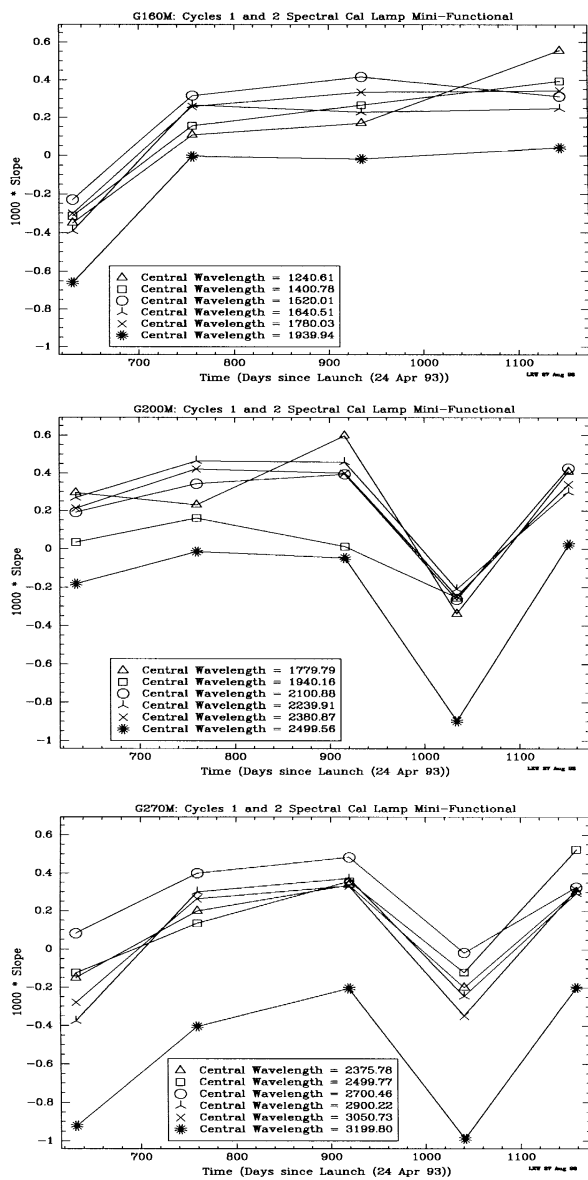


Figures 1-3<sup>1</sup>: Plots of the Difference between the Reference Wavelengths and the CALHRS Wavelengths versus Reference Wavelengths (i.e. the Pt-Ne Lamp line wavelengths). The line just above each plot gives the rootname, proposal id, grating, date and carousel position for the data used to do the fit shown. The data was fit with a 2nd order Legendre polynomial with points above and below 2 sigma from the mean being rejected. The rejected points are in the plot but are surrounded by a diamond shape. The slope (a1) and y-intercept (a0) are included on the plot. No errors are given for these values because the STSDAS.FITTING.GFIT task does not convert the errors when it converts the Legendre values into power-series values. The RMS values for the three plots can be found in Table 1.

The most significant problem lies with the mean deviations, which are shifts in the overall wavelength scale that can lead to significant mismeasurement of velocities. For example, the deviations listed in column (5) of Table 1 correspond to velocity errors as large as 10 km/sec. The Figures 10–15 show how these deviations are

1. The three figures on each of the following pages (except for the last) are for gratings G160M, G200M, and G270M from the top down.

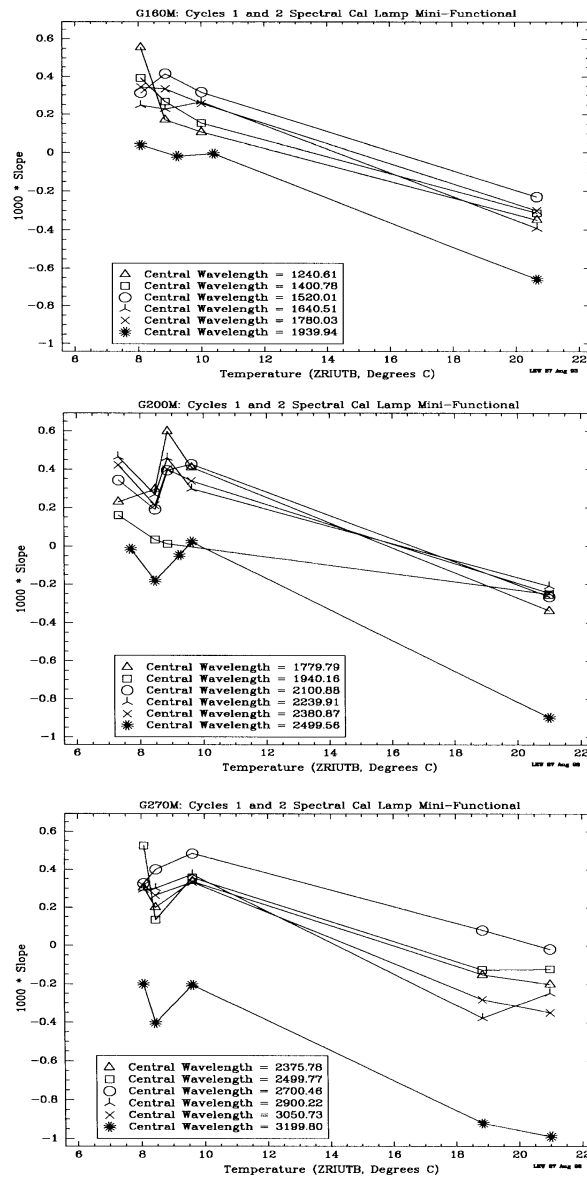
correlated with both time and temperature. In principle it should be possible to improve the calibration algorithm to allow for these quantities. In practice, however, there is a simpler way, and that is to use the information available in the SPYBAL exposure that precedes virtually all GHRS ACCUMs. SPYBALs are wavelength calibration exposures made at a constant carrousel position that is almost always different from the wavelength of the ACCUM. However, the SPYBAL can be used to compute a zero-point correction for its wavelength that can then be applied to the wavelength of observation. That procedure has been shown to yield a wavelength scale that is essentially as good as if a specific WAVE exposure had been obtained and it will be described in the next paper.



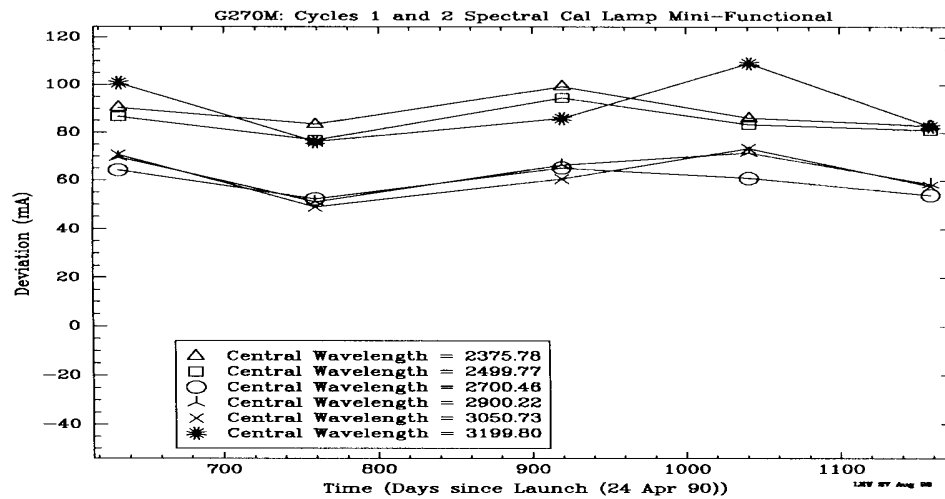
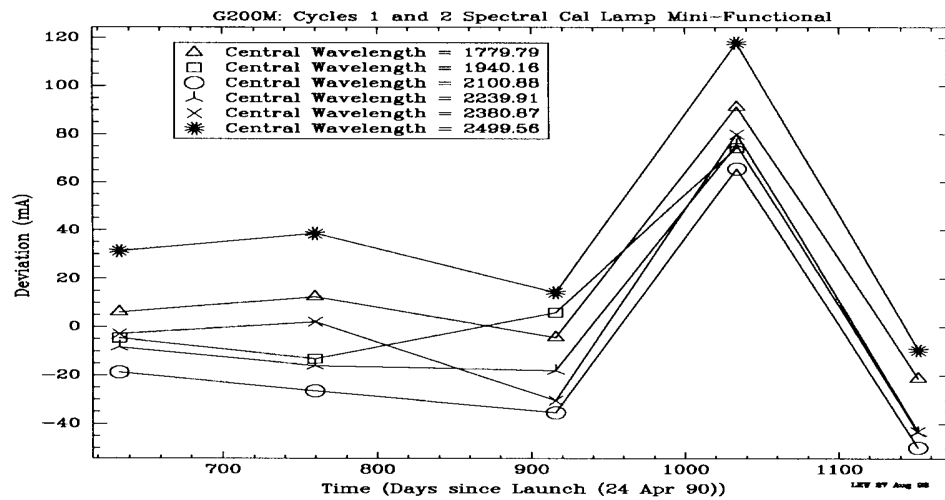
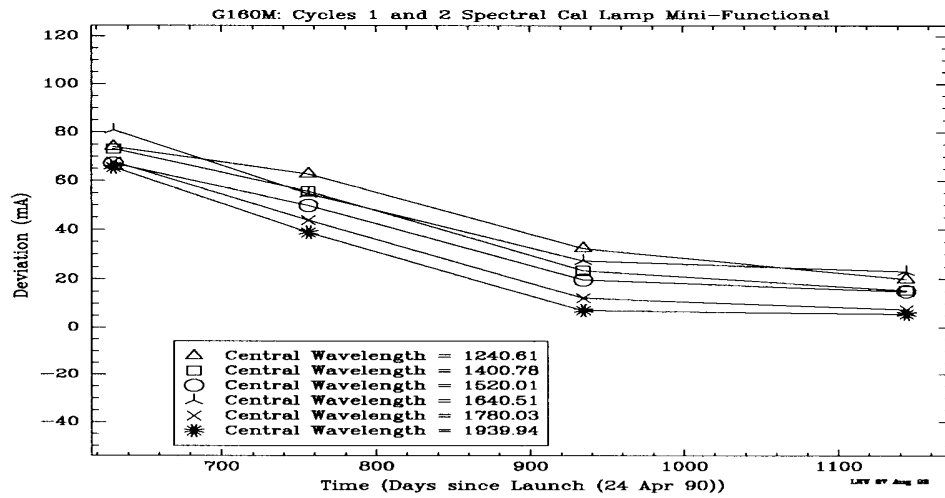
Figures 4-6: Plots of Slope versus Time. The slopes are listed in Table 1 and came from fitting the data as illustrated in Figures 1-3.

## V. Summary

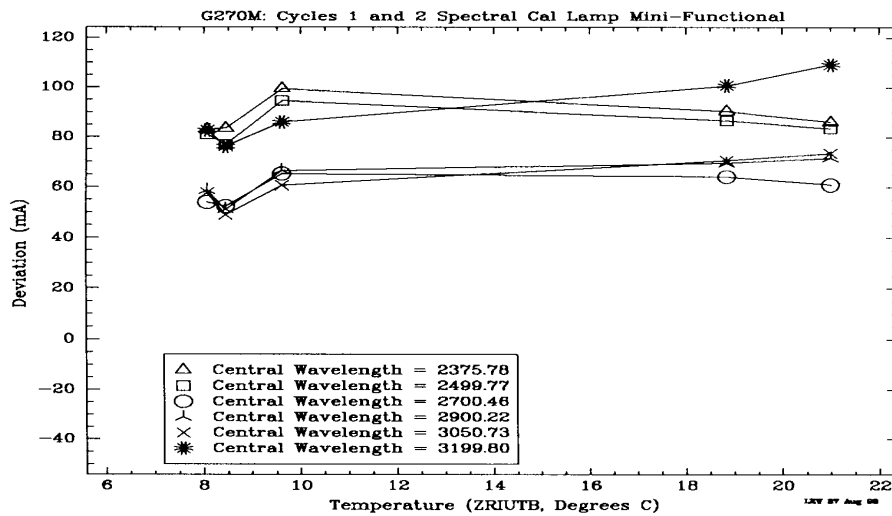
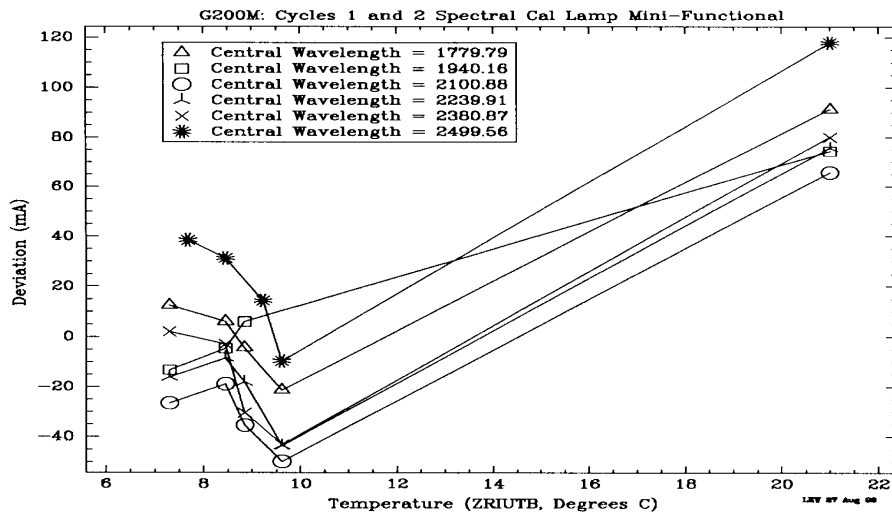
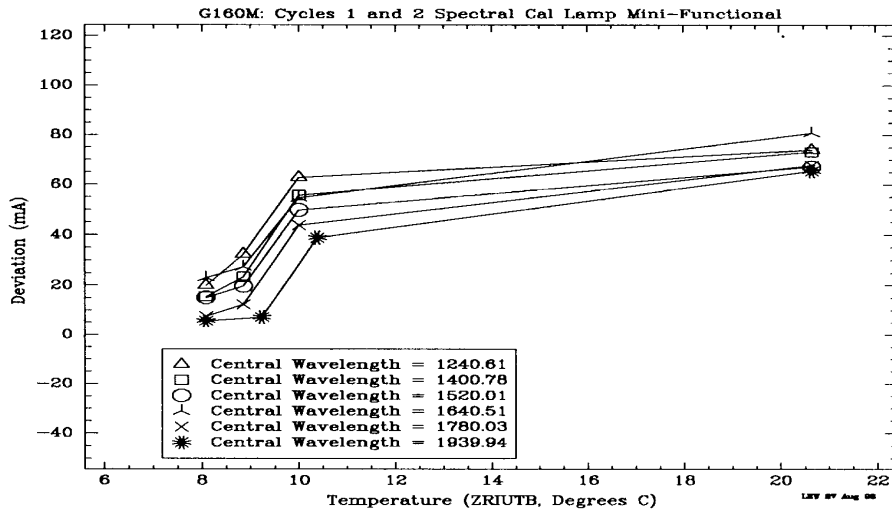
The wavelength calibrations provided to observers as part of the pipeline data reduction are adequate in some nominal sense of meeting specifications, but they are clearly deficient compared to what is possible when a WAVE exposure is obtained to go with the science observation. The most glaring deficiency is in the zero-point for each spectrum, and that is being remedied by providing users a means of utilizing the information contained in SPYBAL exposures. That routine will allow users of current and archival data to extract astrophysical wavelengths that will be on a scale that is essentially as good as it is possible to obtain with a WAVE exposure and so will ensure productive and appropriate use of GHRS data.



Figures 7-9: Plots of Slope versus Temperature. ZRIUTB is the temperature monitor currently used to correct for zeroth-order thermal drifts for grating G160M.



Figures 10-12: Plots of Deviation versus Time. The deviations are listed in Table 1. The deviation was calculated as follows:  $a1 \times l + a0$ , where  $a1$  is the slope,  $l$  is the central wavelength of the grating (see Table 1), and  $a0$  is the y-intercept.



Figures 13-15: Plots of Deviation versus Temperature.

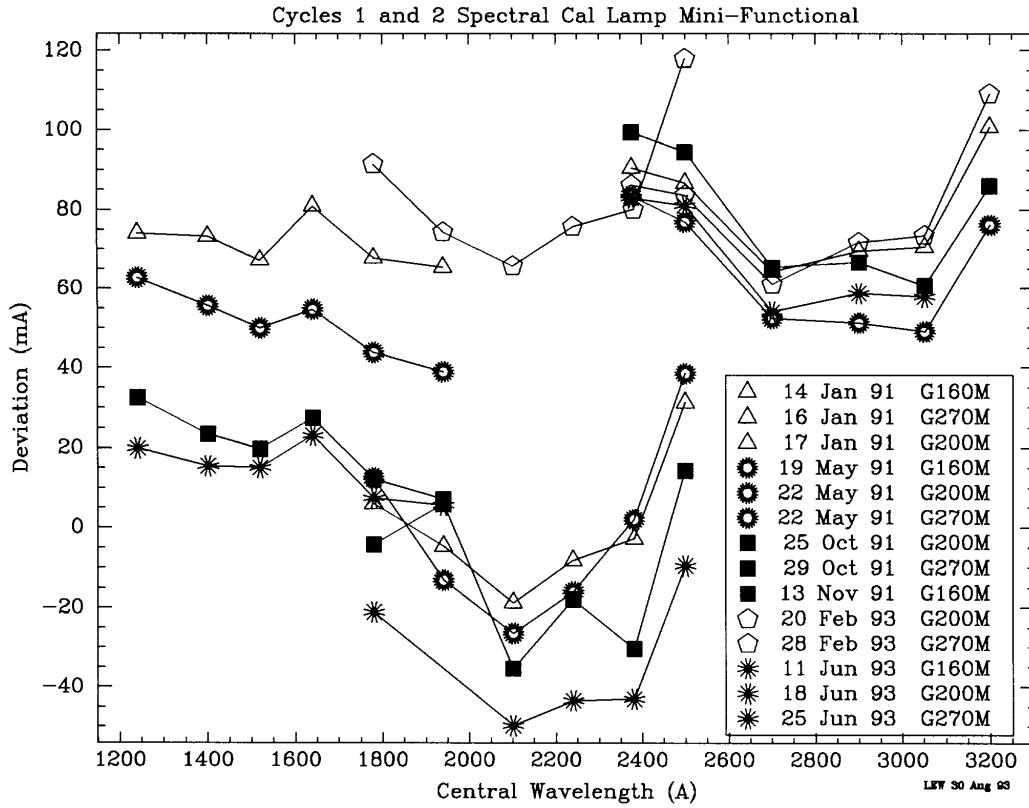


Figure 16: A plot of Deviation versus Central Wavelength for all 3 gratings.

**Reference**

Reader et al. 1990, ApJS, 72, 831

**Table 1**

Rootname	Date	RMS		deviation (mÅ)	slope
		(mÅ)	(km s <sup>-1</sup> )		
		G160M	1240.61 Å		
z0n60602m	14 Jan 92	16.50	3.99	74.0	-3.491e-04
z0n60802t	19 May 92	15.44	3.73	62.7	1.068e-04
z14l0102t	13 Nov 92	4.76	1.15	32.5	1.696e-04
z14l0302t	11 Jun 93	15.64	3.78	19.9	5.538e-04
		G160M	1400.78 Å		
z0n60603m	14 Jan 92	9.30	1.99	73.2	-3.134e-04
z0n60803t	19 May 92	4.55	0.97	55.6	1.543e-04
z14l0103t	13 Nov 92	3.86	0.83	23.4	2.658e-04
z14l0303t	11 Jun 93	4.01	0.86	15.4	3.922e-04
		G160M	1520.01 Å		
z0n60604m	14 Jan 92	12.89	2.54	67.1	-2.294e-04
z0n60804t	19 May 92	4.45	0.88	49.9	3.164e-04
z14l0104t	13 Nov 92	3.50	0.69	19.7	4.154e-04
z14l0304t	11 Jun 93	5.70	1.13	15.0	3.121e-04
		G160M	1640.51 Å		
z0n60605m	14 Jan 92	4.95	0.91	80.9	-3.921e-04
z0n60805t	19 May 92	7.30	1.34	54.6	2.651e-04
z14l0105t	13 Nov 92	4.34	0.79	27.4	2.270e-04
z14l0305t	11 Jun 93	6.29	1.15	23.1	2.470e-04
		G160M	1780.03 Å		
z0n60606m	14 Jan 92	3.11	0.52	67.7	-3.009e-04
z0n60806t	19 May 92	3.57	0.60	43.8	2.574e-04
z14l0106t	13 Nov 92	4.00	0.67	12.2	3.341e-04
z14l0306t	11 Jun 93	2.96	0.50	7.4	3.429e-04
		G160M	1939.94 Å		
z0n60607m	14 Jan 92	3.89	0.60	65.4	-6.586e-04
z0n60807t	19 May 92	4.76	0.74	38.9	-5.484e-06
z14l0107t	13 Nov 92	3.76	0.58	7.1	-1.875e-05
z14l0307t	11 Jun 93	6.46	1.00	5.6	3.937e-05
		G200M	1779.79 Å		
z0n60a02t	17 Jan 92	4.34	0.73	6.0	2.943e-04
z0n60c02t	22 May 92	4.68	0.79	12.4	2.295e-04
z14l0502t	25 Oct 92	5.43	0.91	-4.4	5.976e-04
z14l0602m	20 Feb 93	4.00	0.67	91.4	-3.385e-04
z14l0702t	18 Jun 93	7.41	1.25	-21.2	4.087e-04

**Table 1 (Continued)**

Rootname	Date	RMS		deviation (mÅ)	slope
		(mÅ)	(km s <sup>-1</sup> )		
		G200M	1940.16 Å		
z0n60a03t	17 Jan 92	4.67	0.72	-4.7	3.407e-05
z0n60c03t	22 May 92	5.23	0.81	-13.2	1.602e-04
z14l0503t	25 Oct 92	5.47	0.85	5.9	1.082e-05
z14l0603m	20 Feb 93	14.89	2.30	74.3	-2.522e-04
z14l0703t	18 Jun 93	Lost due to timeout caused by FGS testing.			
		G200M	2100.88 Å		
z0n60a04t	17 Jan 92	3.78	0.54	-18.8	1.912e-04
z0n60c04t	22 May 92	3.22	0.46	-26.5	3.418e-04
z14l0504t	25 Oct 92	2.62	0.37	-35.4	3.932e-04
z14l0604m	20 Feb 93	2.72	0.39	65.7	-2.657e-04
z14l0704t	18 Jun 93	4.41	0.63	-49.8	4.255e-04
		G200M	2239.91 Å		
z0n60a05t	17 Jan 92	2.92	0.39	-8.3	2.668e-04
z0n60c05t	22 May 92	2.38	0.32	-16.1	4.647e-04
z14l0505t	25 Oct 92	3.70	0.50	-18.0	4.585e-04
z14l0605m	20 Feb 93	2.89	0.39	75.7	-2.104e-04
z14l0705t	18 Jun 93	4.72	0.63	-43.5	2.973e-04
		G200M	2380.87 Å		
z0n60a06t	17 Jan 92	2.44	0.31	-2.9	2.118e-04
z0n60c06t	22 May 92	2.89	0.36	2.0	4.217e-04
z14l0506t	25 Oct 92	4.21	0.53	-30.4	3.995e-04
z14l0606m	20 Feb 93	5.25	0.66	80.1	-2.461e-04
z14l0706t	18 Jun 93	4.51	0.57	-43.1	3.389e-04
		G200M	2499.56 Å		
z0n60a07t	17 Jan 92	3.96	0.48	31.3	-1.827e-04
z0n60c07t	22 May 92	5.64	0.68	38.5	-1.458e-05
z14l0507t	25 Oct 92	4.06	0.49	14.3	-4.766e-05
z14l0607m	20 Feb 93	10.87	1.30	117.9	-8.970e-04
z14l0707t	18 Jun 93	6.59	0.79	-9.6	2.235e-05
		G270M	2375.78 Å		
z0n60e02t	16 Jan 92	11.27	1.42	90.5	-1.506e-04
z0n60g02t	22 May 92	17.59	2.22	83.5	2.003e-04
z14l0902t	29 Oct 92	9.95	1.26	99.4	3.364e-04
z14l0a02t	28 Feb 93	17.06	2.15	86.2	-2.004e-04
z14l0b02t	25 Jun 93	11.43	1.44	83.0	3.036e-04

**Table 1 (Continued)**

Rootname	Date	RMS		deviation (mÅ)	slope
		(mÅ)	(km s <sup>-1</sup> )		
		G270M	2499.77 Å		
z0n60e03t	16 Jan 92	7.34	0.88	86.7	-1.249e-04
z0n60g03t	22 May 92	10.81	1.30	76.9	1.347e-04
z14l0903t	29 Oct 92	10.85	1.30	94.5	3.561e-04
z14l0a03t	28 Feb 93	8.62	1.03	83.6	-1.209e-04
z14l0b03t	25 Jun 93	6.19	0.74	81.1	5.249e-04
		G270M	2700.46 Å		
z0n60e04t	16 Jan 92	6.46	0.72	64.2	8.120e-05
z0n60g04t	22 May 92	4.57	0.51	52.4	3.997e-04
z14l0904t	29 Oct 92	4.40	0.49	65.3	4.830e-04
z14l0a04t	28 Feb 93	12.11	1.35	61.0	-1.787e-05
z14l0b04t	25 Jun 93	14.41	1.60	54.0	3.257e-04
		G270M	2900.22 Å		
z0n60e05t	16 Jan 92	2.25	0.23	69.5	-3.767e-04
z0n60g05t	22 May 92	1.65	0.17	51.2	3.003e-04
z14l0905t	29 Oct 92	1.84	0.19	66.6	3.719e-04
z14l0a05t	28 Feb 93	1.87	0.19	71.7	-2.458e-04
z14l0b05t	25 Jun 93	3.86	0.40	58.7	2.928e-04
		G270M	3050.73 Å		
z0n60e06t	16 Jan 92	2.23	0.22	70.6	-2.788e-04
z0n60g06t	22 May 92	2.98	0.29	49.0	2.633e-04
z14l0906t	29 Oct 92	3.65	0.36	60.6	3.325e-04
z14l0a06t	28 Feb 93	2.87	0.28	73.5	-3.486e-04
z14l0b06t	25 Jun 93	2.68	0.26	57.8	3.152e-04
		G270M	3199.80 Å		
z0n60e07t	16 Jan 92	1.62	0.15	100.7	-9.211e-04
z0n60g07t	22 May 92	2.49	0.23	76.2	-4.037e-04
z14l0907t	29 Oct 92	1.36	0.13	86.0	-2.050e-04
z14l0a07t	28 Feb 93	1.89	0.18	109.1	-9.891e-04
z14l0b07t	25 Jun 93	1.36	0.13	82.7	-2.000e-04

# Using SPYBALs to Improve Pipeline Wavelength Calibrations for the First-Order Gratings of the GHR<sup>1</sup>

David R. Soderblom<sup>2</sup>, Lisa E. Sherbert<sup>2</sup> and Stephen J. Hulbert<sup>2</sup>

## Abstract

The previous paper showed that wavelengths produced by PODPS can be significantly in error compared to the solution that would result from obtaining a WAVECAL in conjunction with a science exposure. This *Report* illustrates how the information contained in a Spectrum Y Balance (SPYBAL) exposure, which is routinely obtained before many GHR exposures, can be used to correct the default wavelengths so that they are nearly as good as if a WAVECAL had been specified. This procedure can also be used with archival data.

## I. Introduction

Users of the GHR depend on the wavelength scale to draw astrophysical conclusions from their observations. Many users rely on the default wavelength scale that is provided by the pipeline data reduction system (PODPS). Other observers may obtain exposures of the wavelength calibration lamp just before they observe a celestial object, especially if their science goals demand reliable and precise wavelengths or velocities.

But in other cases an observer may only wish wavelengths that are better than the routine reductions provide and which are largely free of systematic error. Also, an Archival Researcher may find that the default wavelength scale for an existing observation is not fully adequate for his or her needs.

GHR *Instrument Science Report 52* demonstrates that the routine wavelengths provided by PODPS are mostly within the nominal specifications (see the GHR *Instrument Handbook*), but that there are clear and significant departures from true wavelengths that are systematic in nature. These departures arise from, for example, effects of the geomagnetic field, thermal effects within the instrument, possible long-term changes, and so on. Many of these effects can be parameterized in principle by correlating them with quantities recorded in the engineering data stream.

However, many GHR science exposures are preceded by a SPYBAL. A SPYBAL is an exposure made with the spectrum calibration lamp, but instead of being made at the same wavelength as the science exposure (as would be the case for a WAVECAL) a SPYBAL is performed at a wavelength that is fixed for each grating. That means

---

1. Originally published as GHR Instrument Science Report #53

2. Space Telescope Science Institute, Baltimore, MD 21218

that a carousel rotation occurs between the SPYBAL and the science exposure, of course, which means that a SPYBAL cannot provide the precision provided by a WAVECAL. But a comparison of the actual wavelength zero-point seen in the SPYBAL, compared to the nominal expected, offers an opportunity for improving the default wavelengths.

## II. A Comparison of SPYBAL Wavelengths to the Default Scale

We wish to see if corrections to wavelengths measured from SPYBAL exposures can significantly improve the default wavelengths from PODPS. To do that, we searched the data archive and identified 55 instances of GHRS usage when a SPYBAL and WAVECAL were both obtained in conjunction with a science observation. The WAVECAL exposure enabled us to determine how much the default wavelengths were in error for the science exposure. We concentrate here on correcting the zero-point of the wavelengths because we showed in ISR 52 that is the predominant error, with uncertainty in the wavelength scale (dispersion) being nearly insignificant. We can also compare the wavelengths measured from the SPYBAL to the nominal wavelengths expected for it.

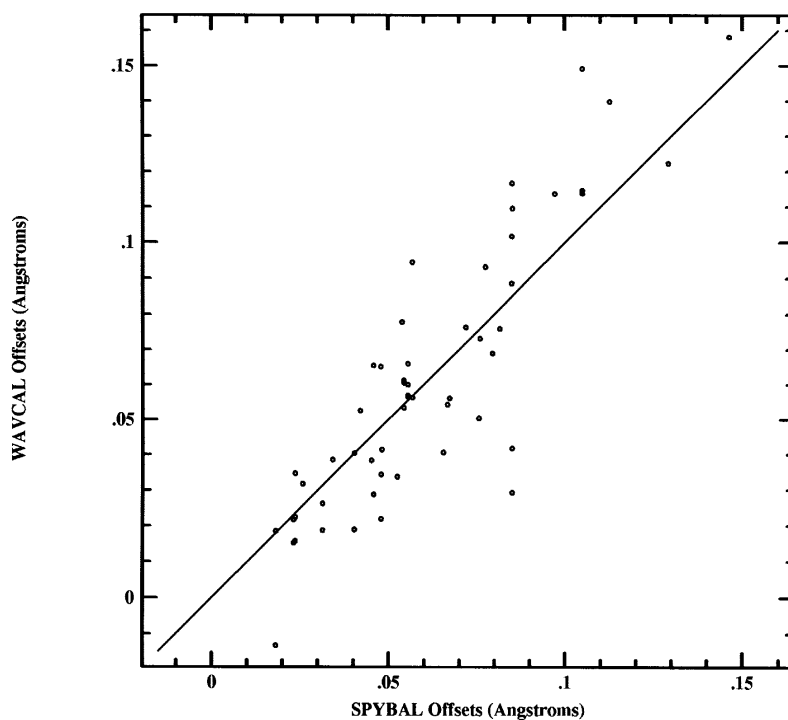


Figure 1: Comparison of wavelength offsets.

The relationship between these two wavelength offsets is illustrated in Figure 1. Note that the points scatter about the line of equality; a formal fit confirms that  $y = x$  is consistent with these data. Thus, on average, a zero-point correction computed from a SPYBAL is equivalent to one determined from a WAVECAL. The scatter about the line then indicates the uncertainty associated with using a SPYBAL in place of a WAVECAL. The rms scatter in Figure 1 is 19 mÅ, which corresponds to 3 km/sec at

1900 Å. This is a substantial improvement over the default wavelengths. Note that Figure 1 shows the deviations measured for all Side 2 gratings.

### III. Using SPYBALs to Improve the Default Wavelengths.

The procedure for applying this technique to currently-obtained or archival data is straightforward:

- Determine if a SPYBAL was obtained in connection with the science exposure or exposures whose wavelengths are to be corrected. If no SPYBAL exists then no improvement can be made, of course. The existence of a SPYBAL can be determined most easily from the OBSMODE keyword. OBSMODE will have the value of SPYBAL in this instance. (Note: currently, PODPS is filling OBSMODE with SPYBAL for *any* observation that makes use of the spectral cal lamps. Thus, both WAVECALs and SPYBALs are labeled as SPYBALs. This problem is currently being worked.) Additionally, one should check the carousel position (found in the CARPOS keyword) of the SPYBAL since the SPYBALs are always obtained at the same carousel position (for a given grating), see Table 1.
- Extract the SPYBAL and process it in the same manner as a science exposure.
- Use the STSDAS task, WAVECAL, to determine the zero-point shift between the calibrated wavelengths and the laboratory wavelengths.
- Apply this difference in wavelength to the science exposures using either of the STSDAS tasks, IMARITH or IMCALC. We see no systematic trend in this shift with increasing wavelength and so it appears inappropriate to apply the correction as a velocity shift, for example.

**Table 1: Default Carousel Positions for SPYBALs**

GRATING	CARPOS
G160M	50764
G200M	25672
G270M	9140
ECH-B	39156

# Wavelength Calibration of the Goddard High Resolution Spectrograph

Don J. Lindler<sup>1</sup>

## Abstract

The Goddard High Resolution Spectrograph (GHRS) is capable of obtaining data with a wavelength accuracy of 1 km/sec in the echelle modes. Both proper observing and data reduction techniques are required to achieve this accuracy.

Shifts of the spectral format at the GHRS diode array can be as large as 300 microns (six diode widths) with time and environmental factors. We have modeled this motion as a function of temperature, time, and the component of the Earth's magnetic field in the direction of dispersion. In the absence of calibration observations of the onboard spectral calibration lamp, this model can be used to reduce the errors from spectral motion in routine processing to approximately one diode width or 3 km/sec in the echelle modes.

## I. Method

The following steps are used to compute the calibration coefficients used for routine reduction of GHRS science data. The calibration includes a model for thermal, time, and geomagnetically induced image motion.

1. Compute the dispersion coefficients for each spectral calibration lamp observation. The dispersion relation gives the photocathode sample position as a function of spectral order and wavelength (section i.i).
2. Compute a new cubic dispersion coefficient by fitting residuals in step 1 simultaneously for all observations made with the same grating mode (section i.ii). Repeat step 1 with the new cubic coefficient.
3. Fit of the central wavelength of each observation as a function of carrousel position. The carrousel controls which grating is selected and the grating scan angle (section i.iii).
4. Shift the dispersion relation to a coordinate system where the photocathode sample position is a function of the differences of the spectral order and wavelength from the central spectral order and wavelength (section i.iv).
5. Compute a global dispersion relation for each grating where the dispersion coefficients in step 4 are modeled by least square polynomials of the carrousel position (section i.v).

---

1. Advanced Computer Concepts, Inc., Potomac, MD 20854

6. Compute a thermal/temporal motion model (section i.vi).
7. Determine the motion caused by the Earth's magnetic Field (section i.vii).
8. Model changes in linear dispersion as a linear function of temperature (section i.viii).

*i.i Compute Dispersion Coefficients for each spectral calibration lamp observation*

The GHRS dispersion relation is given by:

$$s = a_0 + a_1 m \lambda + a_2 m^2 \lambda^2 + a_3 m + a_4 \lambda + a_5 m^2 \lambda + a_6 m \lambda^2 + a_7 m^3 \lambda^3$$

where,

$s$  is the photocathode sample position in 50 micron (one diode) units.

$m$  is the spectral order

$\lambda$  is the wavelength

$a_0, a_1, \dots, a_7$  are the dispersion coefficients.

A single set of dispersion coefficients are computed for multiple spectral orders in the echelle mode when the data are taken without moving the carousel between observations. In all other cases the dispersion coefficients,  $a_0, a_1, \dots, a_7$  are fit for each individual spectral calibration lamp observation. A typical GHRS spectral calibration lamp observation is shown in Figure 1.

**a)** Determine the photocathode sample positions of the spectral lines in the lamp observation with known wavelengths.

**b)** Compute  $a_0, a_1, a_2,$  and  $a_4$  by least-squares fit. There are typically too few lines in a single observation to accurately fit the cubic term,  $a_7$ . The  $a_7$  coefficient is user supplied (its computation is described in a later section).  $a_3, a_5,$  and  $a_6$  are fixed at 0.  $a_5,$  and  $a_6$  are not used for the GHRS but have been included in the relation for compatibility with the International Ultraviolet Explorer dispersion definition.  $a_3$  is used only for the incidence angle correction from the spectral calibration lamp aperture to the science apertures.  $a_4$  is set to 0 for the first order gratings and single order echelle observations.

**c)** Apply an incidence angle correction from the spectral calibration lamp aperture to the small science aperture (SSA). This correction is given by:

$$a_i = a_i(1.0 - p_0) \quad \text{for } i = 1, 7$$

$$a_0 = a_0 - p_1$$

$$a_3 = a_3 - p_2$$

where  $p_0, p_1, p_2$  vary with carousel position,  $R$ , by the following relations:

$$p_0 = c_2 + c_3 R$$

$$p_1 = c_0 + c_1 R + c_4 R^2$$

$$p_2 = c_5$$

## GHRS spectral calibration lamp observation

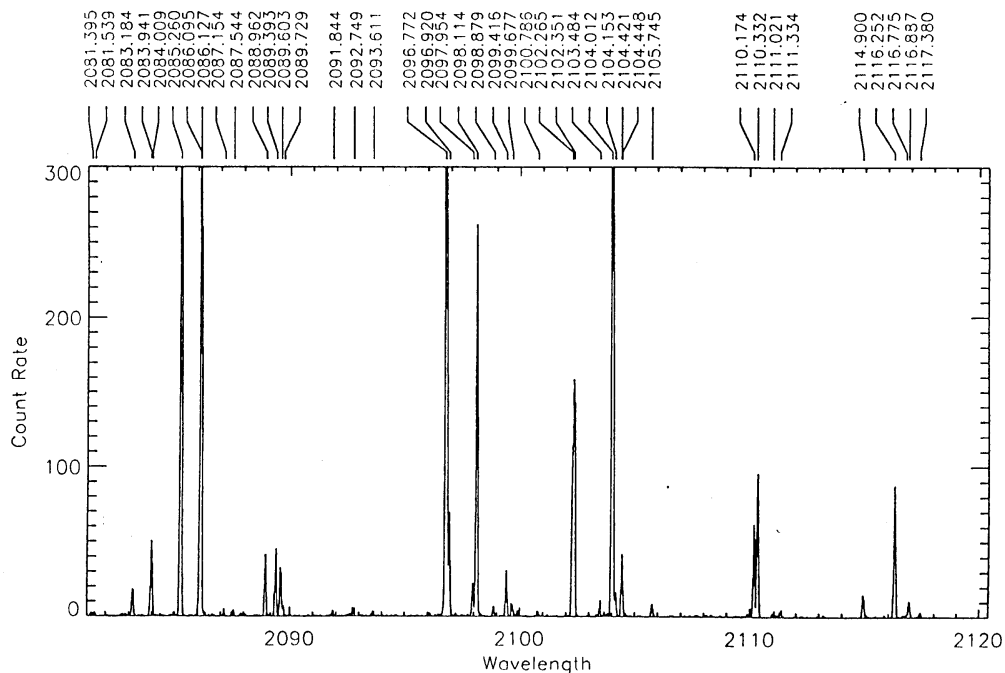


Figure 1: Typical GHRS spectral calibration lamp observation with laboratory wavelengths annotated.

$c_0$ ,  $c_1$ ,  $c_2$ ,  $c_3$ ,  $c_4$ , and  $c_5$  are coefficients that were computed by least squares fit to pre-launch offset measurements between the SSA and the spectral calibration lamp apertures.

*i.ii Computation of the Cubic Term in the dispersion relation.*

The cubic term,  $a_7$ , of the dispersion relation can not be reliably fit from a single observation. To obtain the value of the cubic coefficient it is necessary to combine the results from multiple observations for the grating mode taken at multiple carousel positions. This is done by computing the dispersion relations for all of the observations with the cubic term,  $a_7$ , set to 0.0. The residuals (observed spectral line positions minus the spectral line positions computed from the fitted dispersion relation) are combined from all observations. The combined residuals are fit as a least-squares polynomial of the difference  $m(\lambda - \lambda_c)$ .  $\lambda_c$  is the wavelength at the center of the diode array. Figure 2 shows the results for grating mode G160M. The cubic term of the polynomial can now be used as the  $a_7$  dispersion coefficient. The other coefficients are then recomputed for each observation with the new  $a_7$  coefficient.

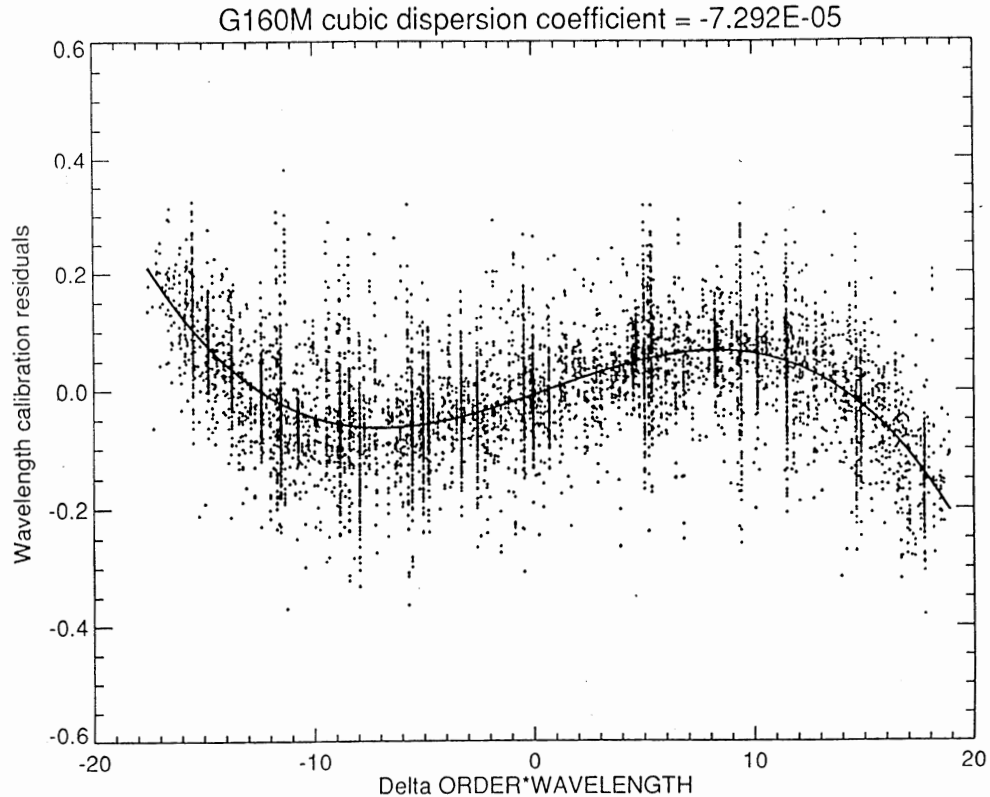


Figure 2: Least-squares polynomial fit to the G160L spectral line position residuals from a quadratic dispersion model. The residuals (in diodes) are plotted versus the distance (in wavelength) of the line from the center of the diode array.

*i.iii Fit the central wavelength as a function of carrousel position:*

The central wavelength of an observation can be modeled as a function of carrousel position by the following relation which can be derived from the grating equation:

$$\lambda_c = (A \cdot \sin(C - R) / 10430.378) / m_c$$

where:

- $\lambda_c$  is the central wavelength for spectral order  $m_c$ ,
- $m_c$  is the central order (1 for first order gratings, 42 for echelle A, and 25 for echelle B),
- $A$  and  $C$  are coefficients fit for each grating mode,
- 10430.378 is used to convert from carrousel positions to radians.

$A$  and  $C$  (tabulated in Table 1) are computed from the dispersion coefficients by:

- a)** adjust  $a_0$  term by subtracting previous thermal/time/geomagnetic model (if available).
- b)** for each dispersion relation compute the wavelength,  $\lambda_c$ , at the x-center of photocathode (sample position = 280.0) for central spectral order,  $m_c$  (1 for first order gratings, 42 for echelle A, 25 for echelle B).

c) Combining all observations for each grating mode, compute the coefficients  $A$  and  $C$  by using a non-linear least squares fit. Do not use observations in the echelle mode when only a single order was used to generate the dispersion coefficients.

*i.iv Shift each dispersion relation to new coordinate system:*

The dispersion coefficients, as defined in section i.i, are not useful for analysis of image motion. Small changes in the computed values of higher order coefficients cause large variations of the lower order coefficients. These large variations also make interpolation between calibrated carousel positions invalid except for linear interpolation. Linear interpolation between carousel positions has been shown to be inadequate. These problems can be avoided by changing the coordinate system of the dispersion coefficients so that the sample position is a function of the difference of the wavelength from a predicted central wavelength (the wavelength at the center of the photocathode). This new relation can be specified by:

$$s = f_0 + f_1U + f_2U^2 + f_3U^3 + f_4V + f_5X$$

where:

$$U = m\lambda - m_c * \lambda_c$$

$$V = \lambda - \lambda_c$$

$$X = m - m_c$$

$$\lambda_c = (A * \sin(C - R) / 10430.378) / m_c$$

$A$  and  $C$  are coefficients fit in section i.iii.

$m_c = 1$  for first order gratings, 24 for Ech-A,

25 for Ech-B

$R$  is the carousel position.

The new sets of dispersion coefficients  $f_0, f_1, f_2, f_3, f_4,$  and  $f_5$  can be computed from the previous coefficients by:

$$f_0 = a_0 + a_1K + a_2K^2 + a_3K^3 + a_4\lambda_c + a_5m_c$$

$$f_1 = a_1 + 2a_2K + 3a_3K^2$$

$$f_2 = a_2 + 3a_3K$$

$$f_3 = a_3$$

$$f_4 = a_4$$

$$f_5 = a_5$$

where:

$$K = m_c * \lambda_c$$

We now have a set of  $f_i$  coefficients for each observation which vary smoothly with carousel position.

**Table 1: GHRs Wavelength Calibration Coefficients**

	G160M	G200M	G270M	ECH-B
$A$	4020.518	4615.5419	5539.2643	63192.867
$C$	54807.949	30600.929	14887.347	50575.473
$m_c$	1	1	1	25
$F_{00}$	-415.91319	76.751444	226.64578	688.63565
$F_{01}$	2.75097431e-02	1.59030662e-02	1.12093029e-02	-2.08831168e-02
$F_{02}$	-2.71933142e-07	-3.10844897e-07	-5.86011762e-07	2.66752644e-07
$F_{10}$	231.28828	75.862971	21.996576	95.848668
$F_{11}$	-8.08765830e-03	-4.38208344e-03	-1.82872974e-03	-4.52938433e-03
$F_{12}$	7.50778582e-08	7.49774546e-08	6.92031147e-08	5.42651856e-08
$F_{20}$	-0.42947955	-8.78849405e-02	6.51991907e-03	9.25916323e-03
$F_{21}$	1.73033639e-05	6.94837105e-06	-9.28531869e-07	-4.01144167e-07
$F_{22}$	-1.73384021e-10	-1.34734267e-10	4.12024736e-11	4.27596025e-12
$F_{30}$	-7.29502865e-05	-4.72720577e-05	-3.00016807e-05	-6.05639617e-08
$F_{31}$	0.0	0.0	0.0	0.0
$F_{32}$	0.0	0.0	0.0	0.0
$F_{40}$	0.0	0.0	0.0	0.39485885
$F_{41}$	0.0	0.0	0.0	-2.02594694e-05
$F_{42}$	0.0	0.0	0.0	2.59948183e-10
$F_{50}$	0.0	0.0	0.0	-1.80474559e-02
$F_{51}$	0.0	0.0	0.0	0.0
$F_{52}$	0.0	0.0	0.0	0.0
$T_{1\text{REF}}$	11.190587 (zdett1 <sup>a</sup> )	-1.8843722 (zfict <sup>b</sup> )	19.027338 (zcst <sup>c</sup> )	17.604019 (zcst)
$D_1$	0.17227277	-0.37546803	-0.70566530	-0.40634180
$T_{2\text{REF}}$	19.289868 (zcst)			
$D_2$	-0.48700304	0.0	0.0	0.0
$JD_0$	48111.5	48109.7	48109.8	48111.0
$D_3$	-1.42976053e-03	-1.09159957e-03	-1.51320847e-03	-5.44631437e-04
$T_{\text{REF}}$	33.370072 (zpabt2 <sup>d</sup> )	31.751161 (zpabt2)	32.713316 (zpabt2)	29.752718 (zpabt2)
$E_1$	4.61042115e-04	4.41550158e-04	3.36457557e-04	6.09907132e-05

a. zdett1 - detector 1 temperature

b. zfict - Fixture interface C temperature

c. zcst - Carrousel stator temperature

d. zpabt2 - Detector 2 preamp assembly box temperature

*i.v Compute a Global dispersion relation for each grating mode.*

The dispersion coefficients  $f_0, f_1, \dots, f_5$  defined in section i.iv can be used to construct a dispersion model for arbitrary carrousel positions. A least squares polynomial can be fit to each coefficient  $f_i$  as a function of carrousel position,  $R$ .

$$f_i = F_{i0} + F_{i1}R + F_{i2}R^2$$

$F_{i0}, F_{i1},$  and  $F_{i2}$  give the least squares polynomial coefficients for dispersion coefficient  $f_i$ . Because of an ambiguity between the  $f_0$  and  $f_4$  terms in echelle modes when only an observation of a single order was used to compute the dispersion relation, only multiple order echelle dispersion relations should be used in the preceding polynomial fit.

The order of the polynomial varies for each  $f_i$ . We presently use a second order (quadratic) polynomial for  $f_0, f_1, f_2,$  and  $f_4$  and a zeroth order (average value) for  $f_3$  and  $f_5$ . Table 1 shows the computed values for  $F_{i0}, F_{i1},$  and  $F_{i2}$ .

*i.vi Computation of new spectral motion model*

At this point any adjustment for a previous motion model subtracted from  $a_0$  in section i.iii should be added to the  $f_0$  values. We are ready to compute an improved motion model. Compute the fitted dispersion coefficients for each observation by using the polynomial from section i.v:

$$f_{i\_fit} = F_{i0} + F_{i1}R + F_{i2}R^2.$$

For echelle mode observations of a single order where  $a_4$  and  $f_4$  could not be computed, set  $f_4$  equal to  $f_{4\_fit}$  and adjust the  $f_0$  term accordingly:

$$\begin{aligned} f_4 &= f_{4\_fit}, \\ \lambda &= A \sin((C-R)/10430.378)/m, \text{ and} \\ f_0 &= f_0 - f_{4\_fit}(\lambda - \lambda_c), \end{aligned}$$

where  $m$  is the spectral order observed and  $\lambda_c$  is the central wavelength for order  $m_c$  computed in section i.iii. The differences of the  $f_i$  values with the fitted values can be used to generate a motion model by:

**a)** For each observation compute the residual,  $\Delta f_0$ , of  $f_0$  from the value computed using the fit in section i.v.

$$\Delta f_0 = f_0 - f_{0\_fit}.$$

**b)** If already calibrated, subtract the contribution to  $\Delta f_0$  due to geomagnetically induced motion. The geomagnetically induced motion will be computed in section i.vii by combining the results of all grating modes for the same detector:

$$\Delta f_0 = \Delta f_0 - G * B_x$$

where:  $B_x$  is the x-component of the Earth's magnetic field for the midpoint of the observation  
 $G$  is the geomagnetic image motion coefficient (diodes/Gauss)

c) Perform a least squares fit to the equation to determine  $D_0$ ,  $D_1$ ,  $D_2$ , and  $D_3$

$$\Delta f_0 = D_0 + D_1(T_1 - T_{1REF}) + D_2(T_2 - T_{2REF}) + D_3(JD - JD_0)$$

where:  $T_1$  is the temperature reading from the selected thermistor,  
 $T_2$  is an optional second temperature from a second thermistor,  
 $T_{1REF}$  is the average  $T_1$  for all observations,  
 $T_{2REF}$  is the average  $T_2$  for all observations,  
 $JD$  is the Julian Date - 2400000,  
 $JD_0$  is the minimum JD for all observations.

Repeat for each thermistor or pair of thermistors. Select thermistors which give the best fit.

d) Adjust  $F_{00}$  computed in step V to correspond to temperature  $T_{1REF}$ ,  $T_{2REF}$  and day  $JD_0$ .

$$F_{00} = F_{00} + D_0$$

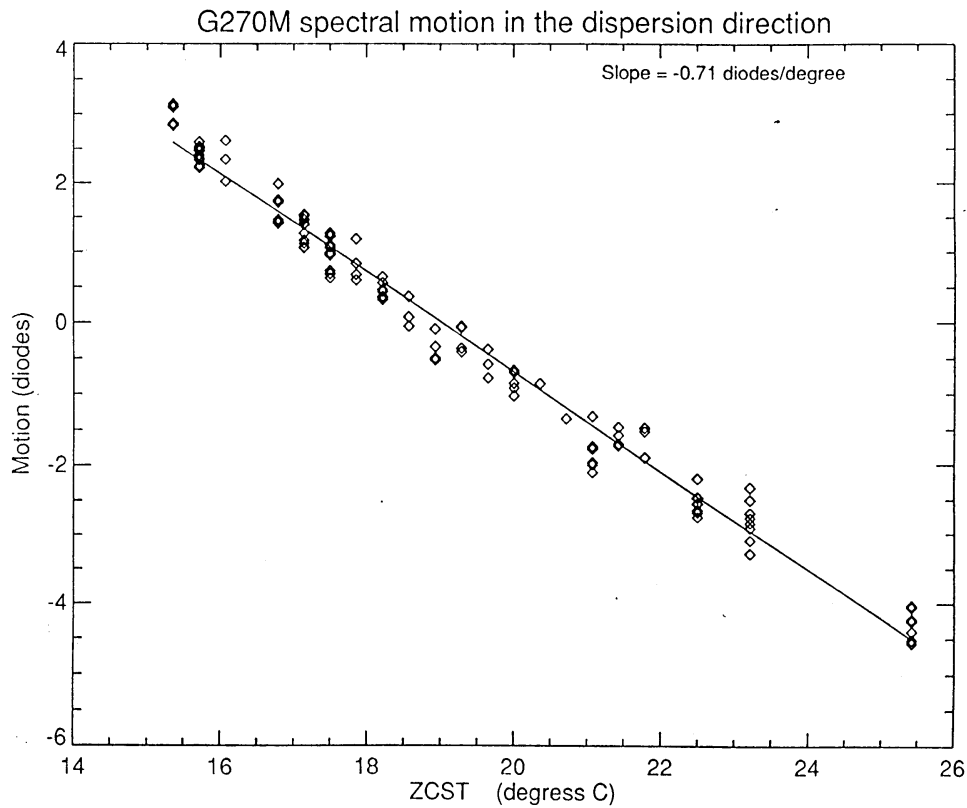


Figure 3: G270M spectral motion versus carousel stator temperature. The diamonds are the motion for each individual observation and the solid line is the model.

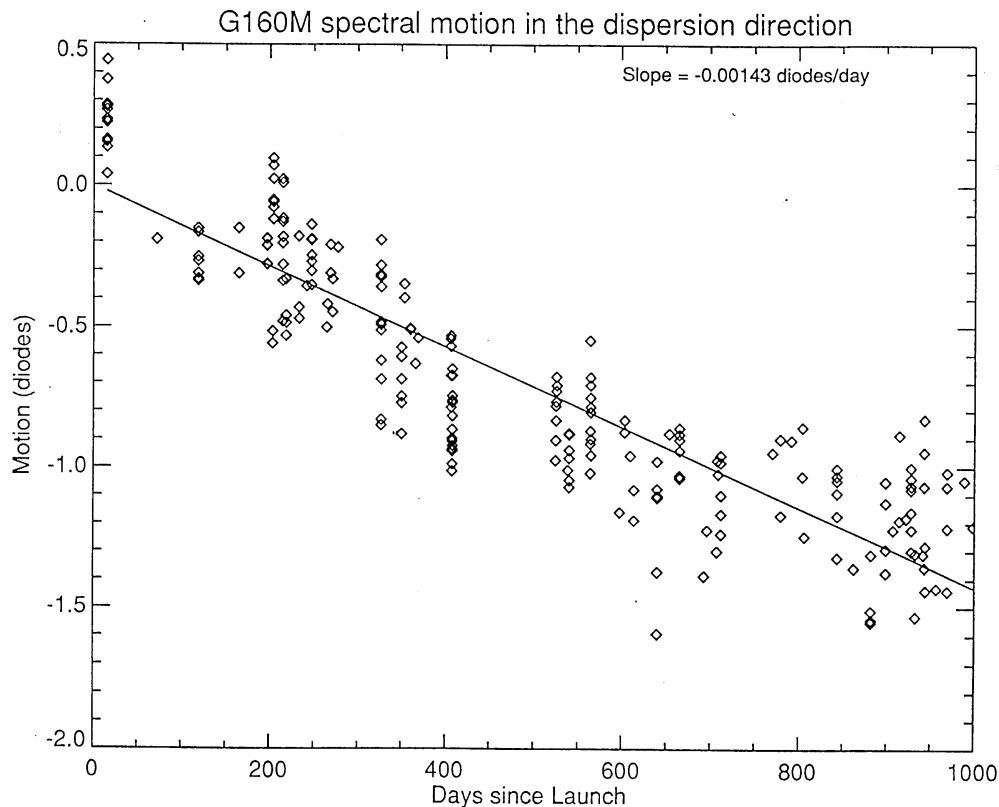


Figure 4: G270M spectral motion versus time. The diamonds are the motion for each individual observation and the solid line is the model.

Figure 3 shows a sample plot of spectral motion versus temperature for grating G270M. G270M was the only grating mode which showed a significant improvement in the fit when a two temperature thermal model was used. We set  $D_2$  to 0.0 for all other grating modes. Figure 4 shows the spectral motion for G270M as a function of time. It appears that a linear model of motion with respect to time will not be sufficient in the future. The rate of change with time appears to be decreasing. The thermal and time motion coefficients computed by this model are tabulated in Table 1.

#### *i.vii Computation of sensitivity to the Earth's Magnetic Field.*

To determine the spectral motion resulting from changes in the Earth's magnetic field vector as the *HST* orbits the Earth, subtract contributions to  $\Delta f_0$  caused by thermal and time motion as modeled in the previous section. This gives any remaining residual from the global dispersion coefficient model that is not predicted by our thermal and time motion model. Since the magnetically induced motion is a detector problem, we can combine the results for all grating modes for the same detector. We then compute the least-squares linear fit to the residuals as a function of the component of the Earth's magnetic field in the dispersion ( $x$ ) direction of the detector. The slope of the least-squares line gives the spectral motion in diodes/Gauss. Figure 5 shows the results for detector 2. Each + mark is the average of the residuals for 25 individual observations.

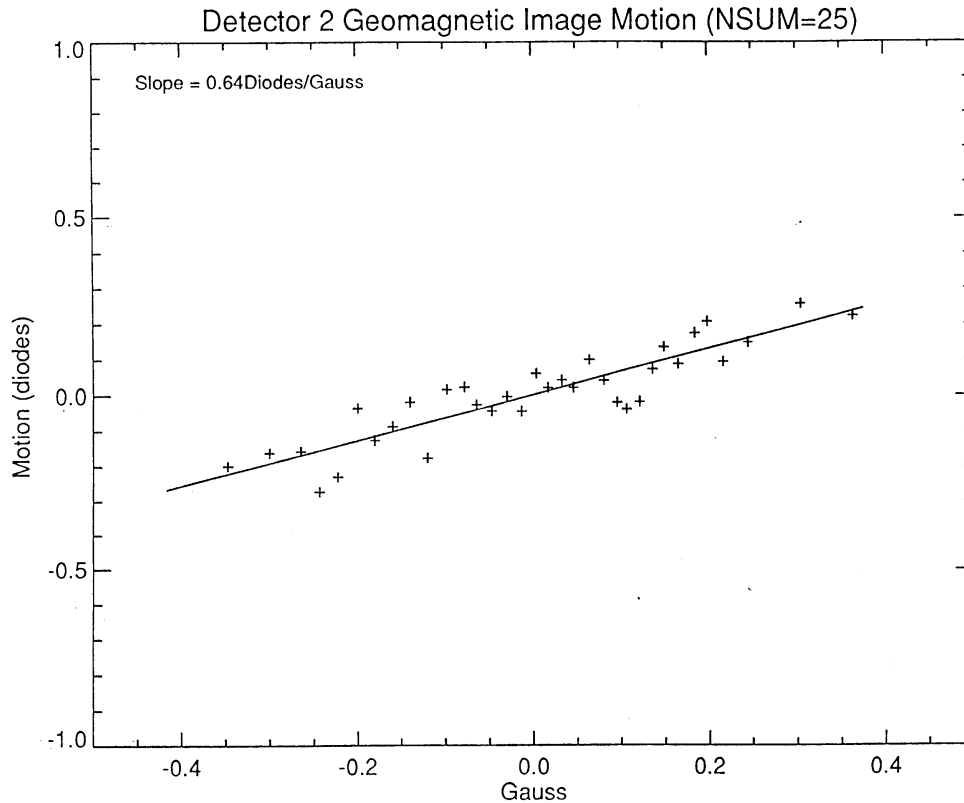


Figure 5: Detector 2 image motion versus the component of the Earth's magnetic field in the detector's x (dispersion) direction. Each + mark represents the average of 25 spectral calibration lamp observations. The solid line is the linear model.

*i.viii Changes in the linear dispersion with temperature.*

In addition to motion of the spectrum with temperature, results show that the linear dispersion, term,  $f_1$ , also changes with temperature. To model these changes:

- a)** For each dispersion relation compute the residual,  $\Delta f_1$ , of  $f_1$  from the value fit by the coefficients derived in section i.v.

$$\Delta f_1 = f_1 - f_{1\_fit}$$

- b)** Perform a least squares fit to the following equation to determine  $E_0$  and  $E_1$  (tabulated in Table 1).

$$\Delta f_1 = E_0 + E_1(T - T_{REF})$$

where:

T is the temperature reading from the selected thermistor, and  
 $T_{REF}$  is the average T for all observations.

Repeat for each thermistor and select the results for the thermistor which gives the best fit.

c) Adjust  $F_{10}$  computed in section i.v to correspond to temperature  $T_{REF}$ :

$$F_{10} = F_{10} + E_0$$

Figure 6 shows the changes in the linear dispersion for grating G160M as a function of the thermistor with the best correlation.

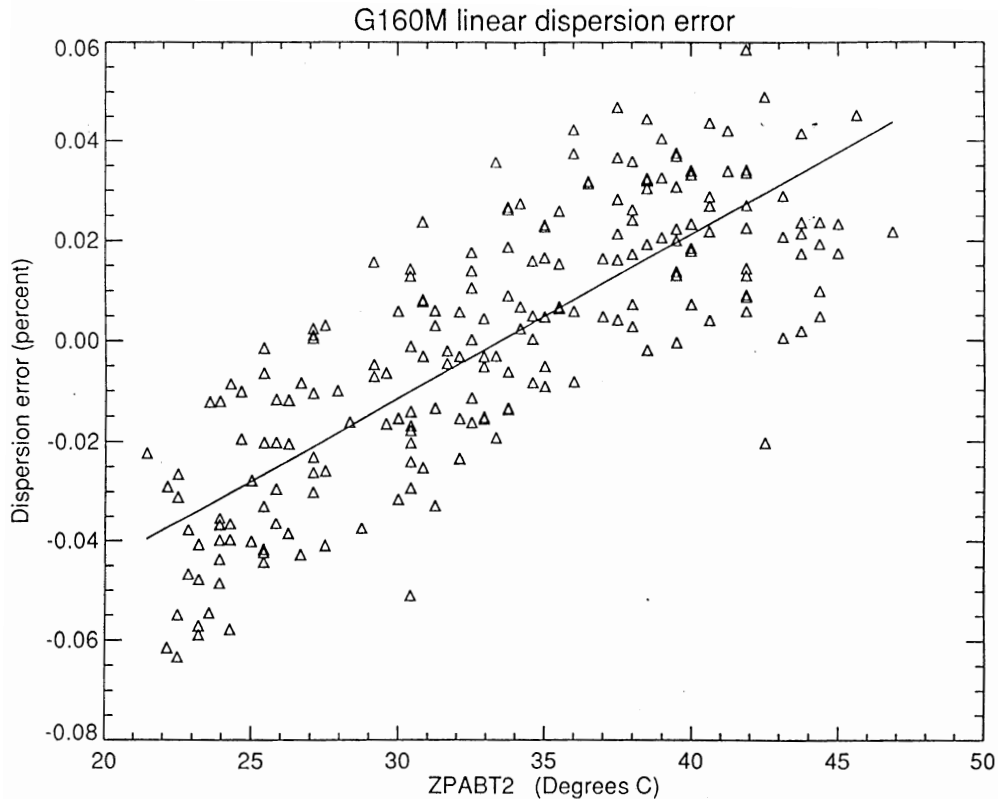


Figure 6: Changes in the linear dispersion of G160M versus temperature. The triangles represent the change from the average for each individual observation. The solid line is the linear model.

## II. Sources of GHRS Wavelength Calibration Errors.

The major sources of errors in the assignment of wavelengths to GHRS science observations are shown in Table 2. When the object is observed in the Large Science Aperture (LSA) the major source of errors are inaccuracies in the centering of the target in the aperture by the onboard flight software and the lack of an accurate incidence angle correction for the LSA. These errors are estimated to be as large as 1.5 diodes.

Wavelengths accurate to 1.0 diodes can be obtained for observations with the target in the SSA using the spectral motion model described in this report. A WAVECAL/SPYBAL observation taken near the time of a science observation can be used to correct the data for inadequacies in the thermal/time motion model. Errors in carousel repeatability and the short term thermal motion between the WAVECAL/

SPYBAL and the science apertures will then be the dominant errors. The most precise wavelengths can be obtained by taking a WAVECAL observation at the same carousel position as the science observation.

**Table 2: Sources of GHRS Wavelength Errors**

Source of Error	Max Error (diodes)	Correction
1) Computation of dispersion coefficients	0.1	None
2) Incidence angle offset between spectral lamp aperture and SSA	0.1	None
3) Errors in thermal/time model	1.0	Use WAVECAL or WAVECAL/SPYBAL
4) Short term thermal motion	0.4 diodes/hour	take multiple WAVECALs
5) Carousel repeatability	0.5 (0.17 typical)	Take WAVECAL at same wavelength as science obs.
6) Onboard Doppler compensation	increases with time since Doppler zero typical=0.15	Use short obs. times (e.g. 5 minutes). Correct errors with ground software.
a) round off in orbital period causing phase shift		
b) round off in Doppler magnitude to nearest 1/8 diode	0.06	
c) round off of correction to nearest 1/8 diode	0.06	
7) Geomagnetic image motion	0.25	short obs. time. Correct with ground software
8) Errors in centering target in SSA	0.21	Use the new SSA return to brightest point
9) Observing in LSA. (centering errors, lack of accurate incidence angle offset calibration)	1.5	Use the SSA

### III. Obtaining the Ultimate Wavelength Precision with the GHRS

Observing in the SSA is the only special observing consideration required to obtain wavelengths accurate to within one diode. If better wavelengths are desired, the following observing guidelines can be followed.

- 1) Observe in the small science aperture.
- 2) Use an SSA return to brightest point target acquisition. This decreases the errors caused by mis-centering of the target in the aperture.
- 3) Limit individual exposures to 5 minutes. This limits the loss of resolution and allows corrections for geomagnetically induced image motion and errors in the onboard Doppler compensation processor.

4) Take a WAVECAL at each wavelength observed. If total time at a single wavelength exceeds 15 minutes, take a WAVECAL both before and after the science observation. This limits the errors resulting from short term thermal motion.

5) For long exposures, take a wavecal every 30 to 60 minutes. Do not allow a WAVECAL/SPYBAL to be performed without a WAVECAL before and after it. The WAVECAL/SPYBAL moves the carousel.

The following accuracy is achievable by following these guidelines:

<u>Source of Error</u>	<u>Error(diodes)</u>
Accuracy of the dispersion relation	0.1
Spectral cal lamp to SSA offset error	0.1
Centering error in the SSA	<u>0.125</u>
TOTAL	0.325 diodes = 1 km/sec
Errors added in quadrature	0.19 diodes = 0.6 km/sec

# Determining the Vignetting and Echelle Blaze Function for the GHRS

R. D. Robinson<sup>1</sup>

## Abstract

I describe the techniques used in deriving the vignetting in the GHRS when used with the first order gratings G140M, G160M, G200M, G270M and G140L. I also present an analysis of the blaze function and vignetting present in the echelle B data.

## I. Introduction

The sensitivity function of the spectrograph is simply a conversion factor between count rate and absolute flux at any given wavelength. Inspection of the data immediately reveals, however, that the value of the sensitivity can be highly dependent on the position of that wavelength sample on the photocathode of the detector. For the first order gratings the sensitivity is a three dimensional function of the variables X, Y and  $\lambda$ . For the echelle gratings we have the additional complication of the blaze or ripple function, where for any given order the response peaks at a given wavelength and decreases at both higher and lower wavelengths.

To simplify the problem we have separated the total spectrograph sensitivity into a variety of components. The simplest and most easily calculated is the standard sensitivity, defined for first order gratings as the conversion between count rate and absolute flux at the center of the detector. For the echelle the sensitivity is the conversion factor measured at the peak of the blaze function for each order. Large scale variations in this sensitivity along both the X and Y directions are then identified as vignetting, which includes the influence of obstructions within the light path as well as such effects as losing light from the wing of the PSF off the end of a diode, non-uniformities in the photocathode faceplate (sleeks) and large scale variations in the gain of the diodes or the response of the photocathode. Small scale imperfections on the photocathode are referred to as blemishes and are discussed by Wahlgren, et al (this volume), while small scale, small amplitude (1-2 percent) gain variations from the photocathode or diodes are referred to as granularity and discussed by Cardelli (this volume).

In this paper we describe the procedures used to determine the vignetting and blaze functions for the GHRS gratings as well as the results themselves. The reduction procedures are described so that the general user can understand the limitations of the final calibrations.

---

1. CSC, Goddard Space Flight Center, Code 681/CSC, Greenbelt, MD 20771

## II. Vignetting in the First Order Gratings

The data used in deriving the vignetting were taken during the science verification (SV) phase of the mission. Observations of  $\mu$  Columbae were used to calibrate all of the medium resolution gratings (G140M, G160M, G200M and G270M). Observations of this star were supplemented by observations of the fainter BD+25D325 in calibrating the low resolution (G140L) grating. The data consisted of sequences of exposures taken over the entire useful wavelength range of each first order grating and with an approximately 50 percent overlap in wavelength coverage between adjacent exposures. Thus, nearly all wavelengths were sampled at two positions on the detector. In figure 1 we show an overlapping plot of some of the G270M data illustrating the effects of vignetting on the data.

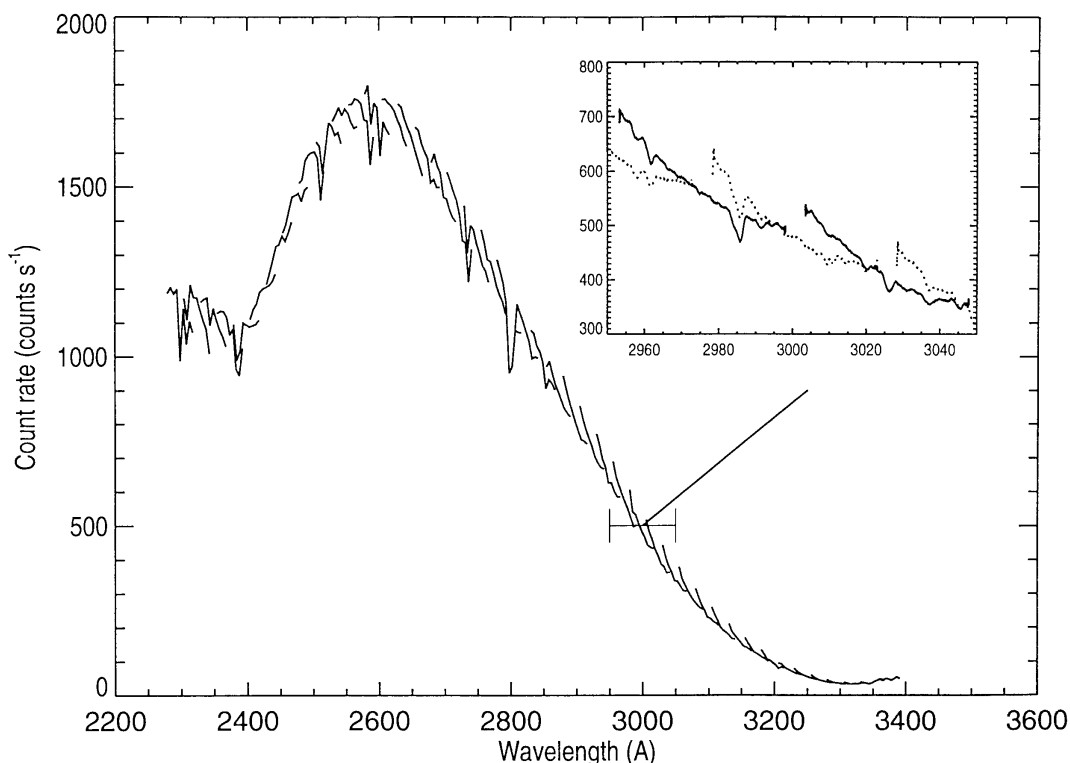


Figure 1: Overplot of the G270M calibration data showing the effects of vignetting. The large scale trends are caused by sensitivity variations.

The basic technique for measuring the vignetting was to use a simple sensitivity calibration to calculate the absolute flux for the data and then compare the calculated flux with that from a reference spectrum. The large scale differences between the two were then attributed to vignetting. The diode array spans nearly the full width (x-dimension) of the photocathode. Since the spectrum is slightly tilted with respect to the x-axis, changing the wavelengths of the observation moved the observations along the y dimension. Thus, by analyzing spectra taken at different wavelengths you can build up a complete two dimensional picture of the vignetting function.

In practice the analysis is somewhat more complicated. Firstly, the original reference spectrum for  $\mu$  Columbae was taken with the IUE in low resolution mode and had

very low spectral resolution, typically about  $5\text{\AA}$  compared with resolutions of  $0.57\text{\AA}$  for the G140L and  $0.05\text{-}0.1\text{\AA}$  for the medium resolution gratings. This IUE spectrum worked reasonably well for the G140L data and for the medium resolution gratings at wavelengths greater than  $1900\text{\AA}$ . It was totally inadequate, however, for analyzing the medium resolution observations at shorter wavelengths, where substantially more fine structure is present. For these wavelengths we first determined a vignetting function for the G140L grating using the IUE spectrum, applied these vignetting corrections to the G140L data and then merged the individual spectra into a low resolution GHRS reference spectrum covering the wavelength range between  $1100\text{\AA}$  and  $1900\text{\AA}$ . This spectrum was then used as a reference in analyzing the medium resolution observations.

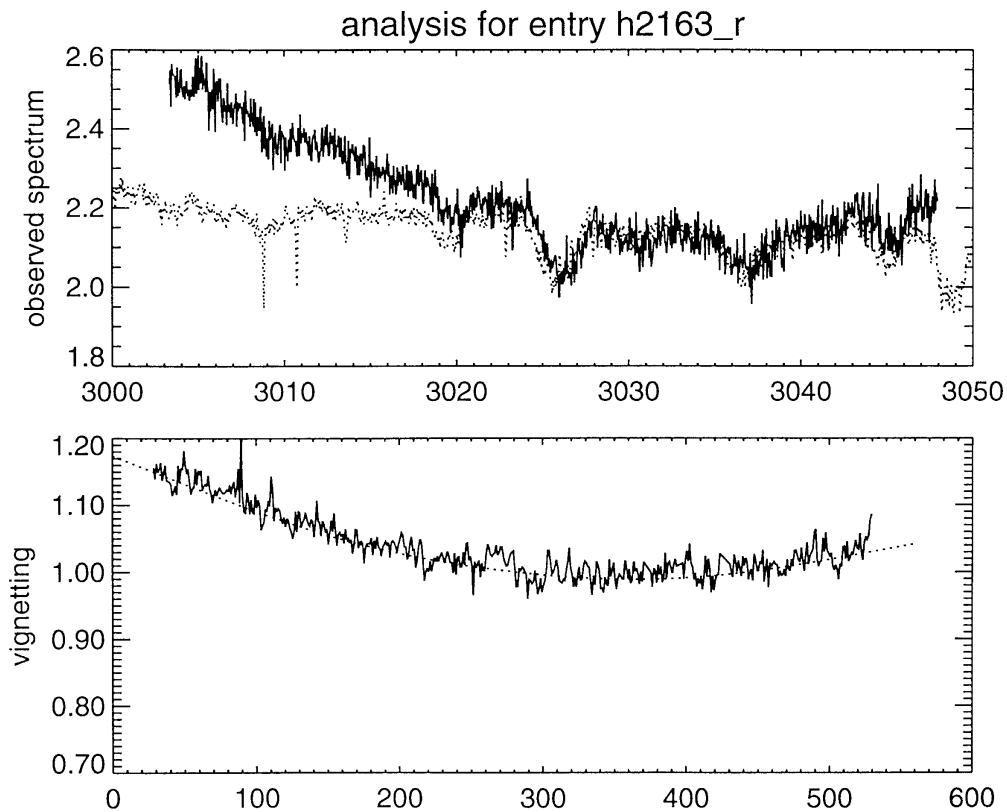


Figure 2: Analysis of the vignetting in a single exposure taken with the G270M grating. The low resolution *IUE* reference spectrum is shown as a dotted line in the top plot.

Figure 2 shows an example of the vignetting calculation for an individual spectrum. In many cases it was necessary to reduce the resolution of the observations to that of the comparison spectrum by convolving with an appropriate instrumental profile. A cross correlation was also performed and the calibration spectrum was shifted to align as closely as possible with the data. The raw vignetting curve normally had a substantial fine structure which is caused by noise, calibration errors in the comparison spectrum, inaccuracies in degrading the resolution of the observation, as well as blemishes on the photocathode. While some of this structure may be real we found that it was better to deal with it as blemishes rather than vignetting and eliminated it from the final vignetting curve by fitting a smooth, low-order spline to the data. Typically, 5 nodes were found to give an acceptable fit.

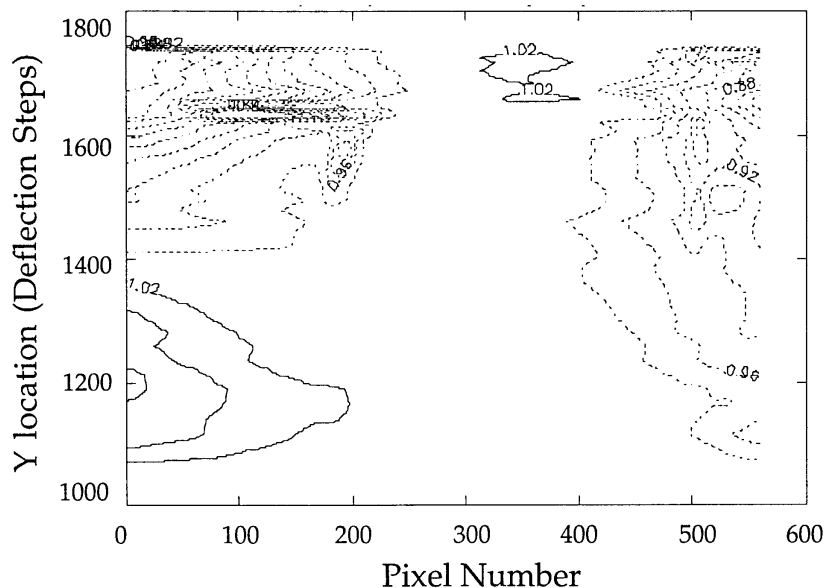


Figure 3: A total vignetting function for the G140M grating, done before smoothing in the Y direction. Note the large “scratch” near Y location 1625. Details of the plot are given in Figure 5.

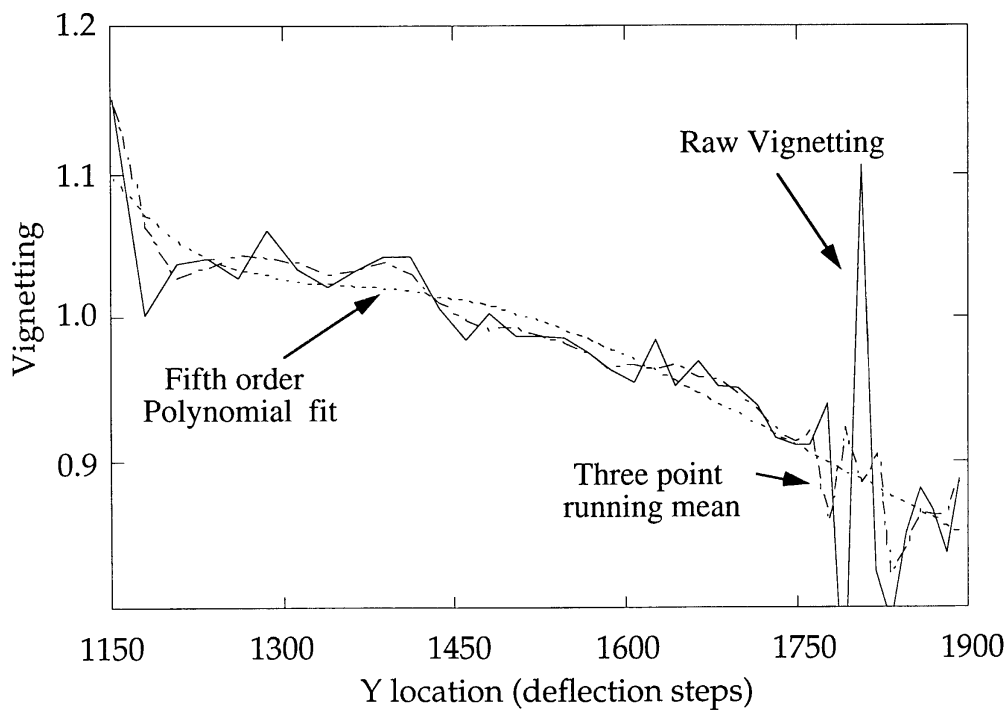


Figure 4: Smoothing the vignetting function in the Y direction. A 3 point running mean was found to give the best results.

The vignetting curves for the individual wavelength settings were eventually merged into an image, which represented the full vignetting function for that particular grating. Figure 3 shows a sample, raw vignetting function for grating G1. The noise is caused by errors in the spline fits to the individual vignetting curves as well as the fact that the vignetting may change dramatically over the 400  $\mu\text{m}$  height of an individual diode. Note, for example, the very sharp feature at the Y location of 1650 deflection units, which is caused by a sizable scratch in the photocathode.

Figure 4 shows a slice of the image along the Y direction (e.g. at constant sample position) and illustrates the large scale trends which we want to retain. Several schemes were tried for smoothing the data along the Y direction, including polynomial and spline fits. In the end it was decided that a simple three point running mean was sufficient to smooth the data without overly distorting the large scale trends. The final, smoothed vignetting functions are presented in figure 5.

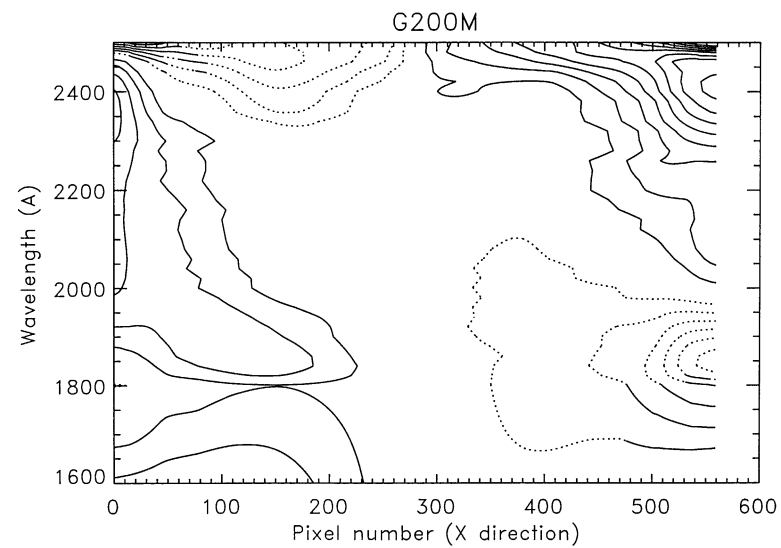
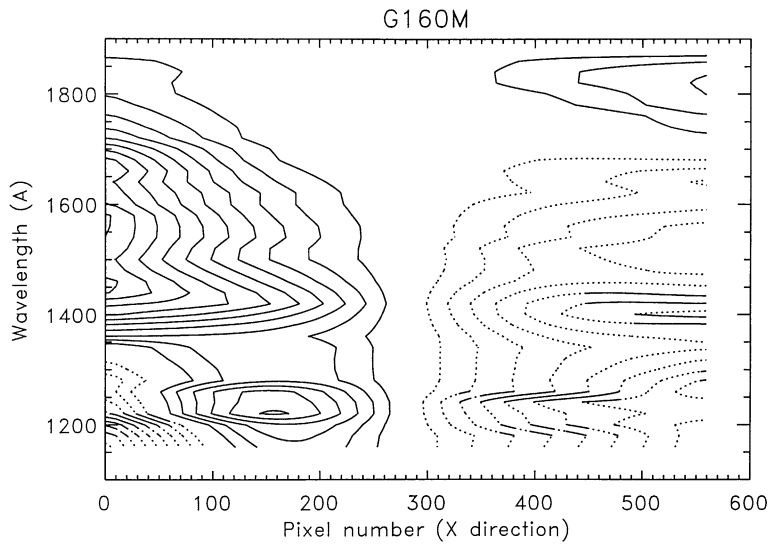
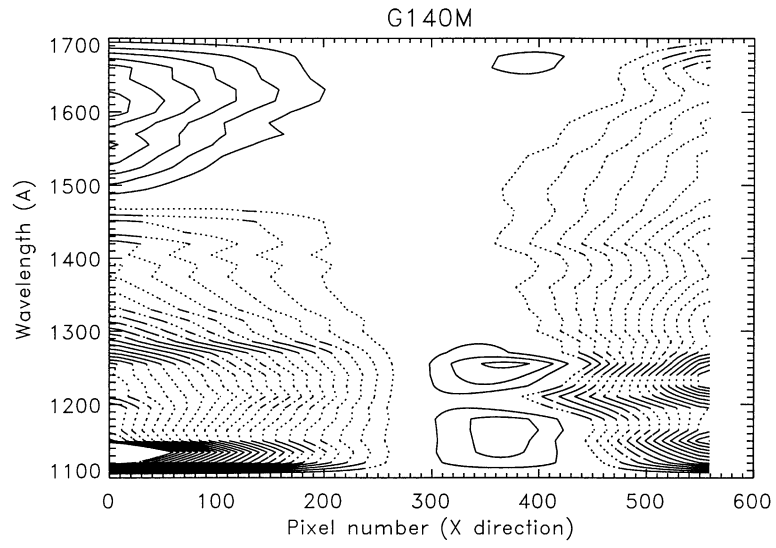
### **III. Calibrating the Echelle Data**

#### *The Echelle B Blaze Function*

A well known characteristic of echelle spectrographs is that the sensitivity for a specific order peaks at a given wavelength and decreases at both higher and lower wavelengths. This is the so-called blaze function and has approximately a constant shape when plotted against the variable  $m\lambda$ , where  $m$  is the order number and  $\lambda$  is the wavelength. There were extensive pre-launch tests of the echelle characteristics, and it was thought that in-orbit calibrations only needed to sample the full calibration. These data would then allow us to adjust the groundbased calibrations and thereby obtain the full on-orbit characteristics. As shown below, this strategy turned out to be only marginally successful.

The star  $\mu$  Columbae was again chosen as the spectrophotometric standard. The pattern of exposures taken during SV tests designed to study sensitivity, vignetting and ripple for the echelle B grating are shown schematically in figure 6. SV tests designed to measure the echelle A grating characteristics failed during execution and the side 1 electronics failed before these tests could be rerun. The blaze function tests consisted of sequences of exposures at different wavelengths along an individual order (termed a WSCAN) covering the entire useful wavelength range for 6 of the 16 orders. Sensitivity and vignetting were to be calculated using scans of all of the orders (termed an OSCAN) at 3 specific values of  $m\lambda$ , one near the peak of the response function and one at each end of the free spectral range.

The analysis began by determining the basic sensitivity function, which was defined as the conversion between count rate and absolute flux as measured at the peak of the blaze function for each order. These calculations were carried out using the central OSCAN. This sensitivity function was then used to determine a rough absolute flux calibration for each spectrum in the WSCAN taken over individual orders. The results of such a calculation are shown in figure 7, which clearly shows the effects of both the vignetting and the blaze function. The roughly calibrated data go to higher fluxes than the reference because the sensitivity was not measured exactly at the blaze maximum.



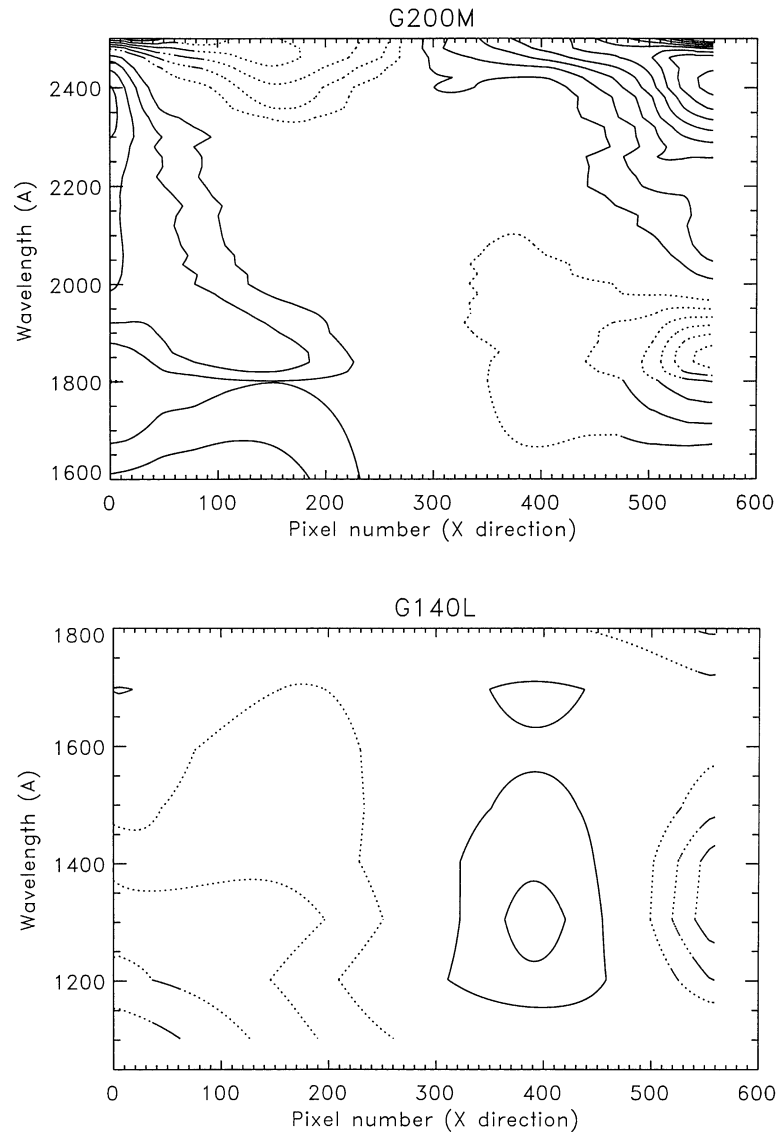


Figure 5: Final vignetting for the first order gratings. These are correction factors for the data, defined to be 1 at the center of the diode array. The spacing is in intervals of 1 percent, with the solid lines being greater than unity (e.g. 1.01, 1.02, etc.), while the dotted lines are less than unity (e.g. 0.99, 0.98, etc). The corrections are made by dividing the observed counts by the vignetting.

To calculate the blaze function ( $R$ ), the absolute flux from the *center* of each of the spectra in the WSCAN was compared with the flux in a reference spectrum, derived by combining the calibrated, vignetting corrected spectra obtained during the first order gratings tests. A non-linear least squares fit was then determined between the measured corrections and a theoretical curve based on equation 18 in Bottema (1980, SPIE Proc, 240, 171);

$$R = C \times N \times \text{sinc}^2(X) ,$$

where,

$$\begin{aligned}
 N &= \cos (\theta + \beta + \delta) / \cos (\theta + \beta - \delta) , \\
 X &= \pi \times m \times \cos (\theta + \beta + \delta) \times \sin (\theta) / \sin (\theta + \beta) , \text{ and} \\
 \theta &= (R0 - CP) / 182.0444 - \beta
 \end{aligned}$$

Here  $\beta$  is the echelle blaze angle,  $\delta$  is the half angle between the collimator and the cross disperser,  $\theta$  is the grating angle,  $R0$  is the reference carousel position specifying the point of maximum sensitivity,  $C$  is a normalization constant,  $CP$  is the carousel position and  $m$  is the order number. In the fitting process values of  $\beta$ ,  $\delta$ ,  $R0$  and  $C$  were determined for each order. Ideally, these should be identical for all orders, since they refer to physical properties of the spectrograph. In practice their values varied between orders, giving the curves shown in figure 8. This behavior was expected, since it occurred in the ground-based tests (see the pre-launch calibration report for the GHRS).

Rather than use separate values of  $\beta$ ,  $\delta$  and  $R0$  for each order, it was decided to adopt representative values and introduce 'fudge factors' into the expression to account for deviations from the norm. To do this we replace the variable  $X$  with  $X'$ , such that;

$$X' = A \times X + B$$

where  $A$  and  $B$  are the fudge factors, with  $A$  controlling the width of the function and  $B$  determining the position of the sensitivity maximum. Unfortunately, the representative values for  $\beta$ ,  $\delta$ , and  $R0$  determined from the on-orbit calibrations differed significantly from the values obtained from the ground, so that none of the results of the ground-based calibrations could be used in the on-orbit calibration.

In figure 9 we show the best fit of the theoretical blaze function to the observations in order 20, using single values for  $A$  and  $B$ . The results give extremely good agreement with the observations. Unfortunately, this fitting could only be done for those orders for which a full WSCAN was available. To determine the fudge factors in the other orders we did a linear least-squares fit to the best single values of  $A$  and  $B$  for the WSCAN orders, as shown in figure 10. Note that while the values of  $B$  give a reasonably well defined, linear trend with order number, the values of  $A$  have considerably more scatter.

### *Vignetting in Echelle B*

Figure 11 shows an overlap of the spectra taken in the order 20 WSCAN after conversion to absolute flux and correction for the echelle blaze function. A significant vignetting is obviously present. The vignetting also changes significantly with wavelength, even though the range of  $Y$  positions of the photocathode which is sampled by this data is small. To determine a representative vignetting function for the echelle we used the same OSCAN data which was used to derive the absolute sensitivity curve. This sampled all of the orders near the center of the free spectral

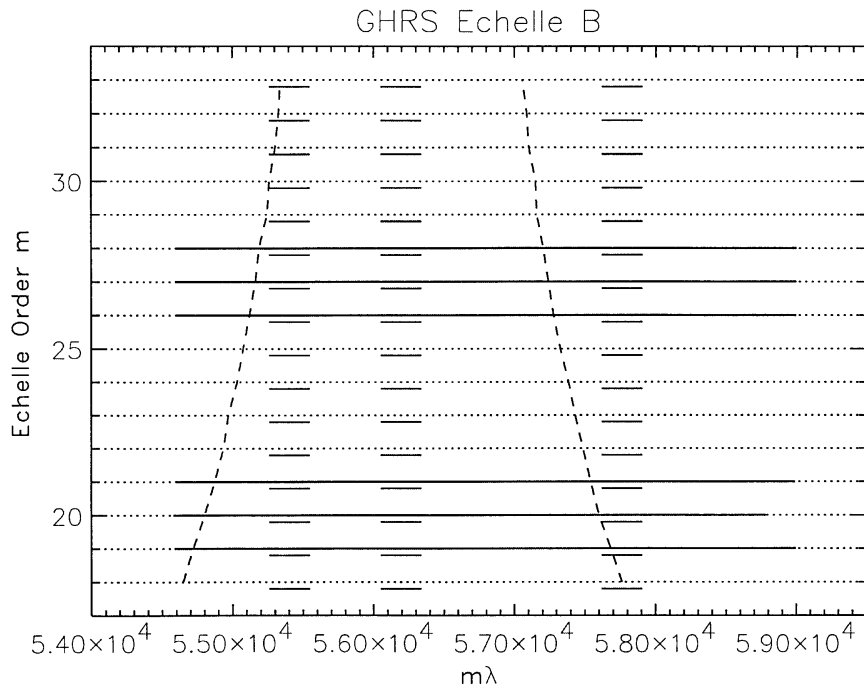


Figure 6: Wavelength and orders observed during the SV tests designed to measure echelle sensitivity, vignetting and blaze function.

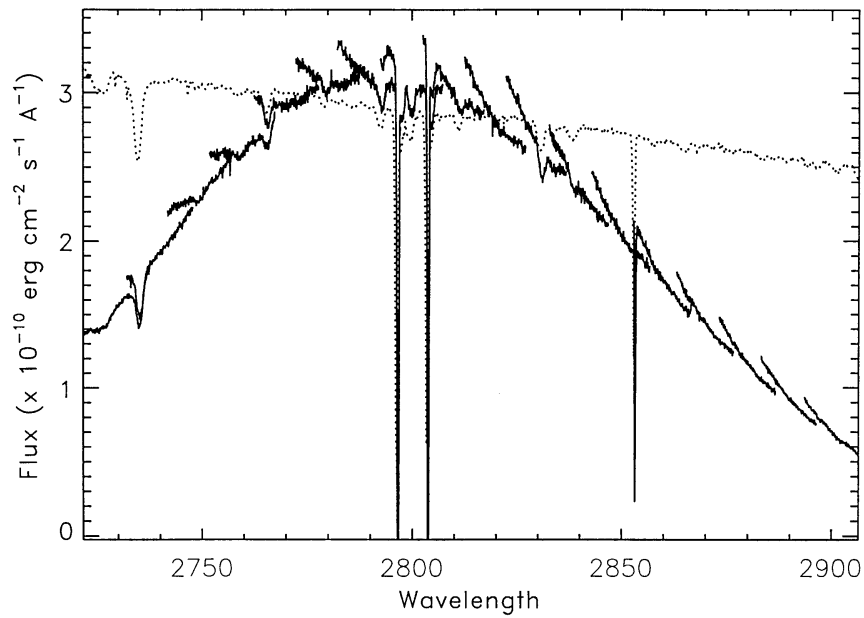


Figure 7: Overplot of the WSA data for order 20 (solid). The reference spectrum, which shows the correct flux levels, is given by the dotted line.

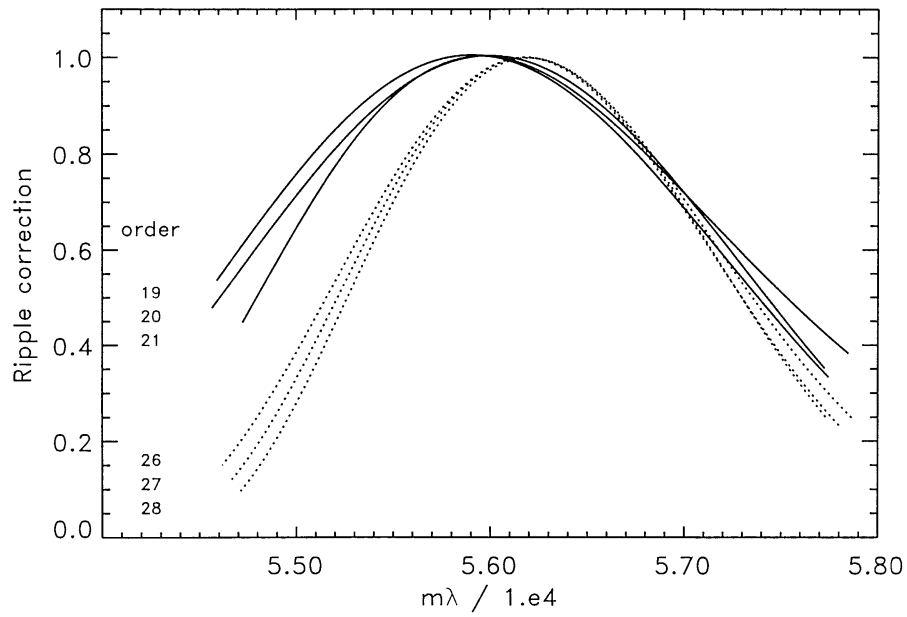


Figure 8: Measured blaze function for the 6 orders with good wavelength coverage.

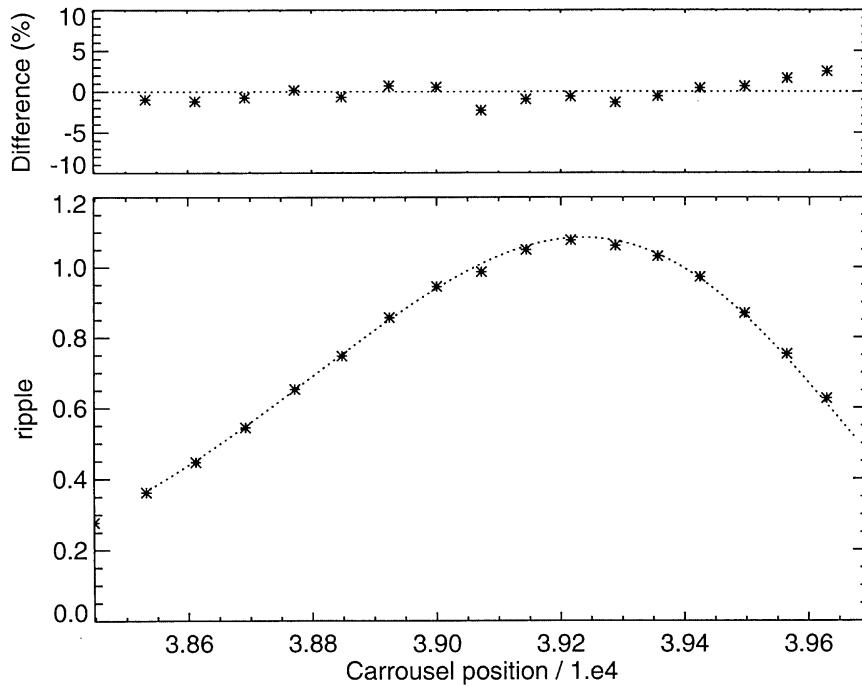


Figure 9: Results of the fitting of the observations to the theoretical formalism described in the text.

range and covered nearly the entire surface of the photocathode. The method of analysis was nearly identical to that used in determining vignetting for the first order gratings, except that the reference spectrum was the medium resolution GHR atlas of  $\mu$  Col which was generated from data obtained for the first order grating calibrations.

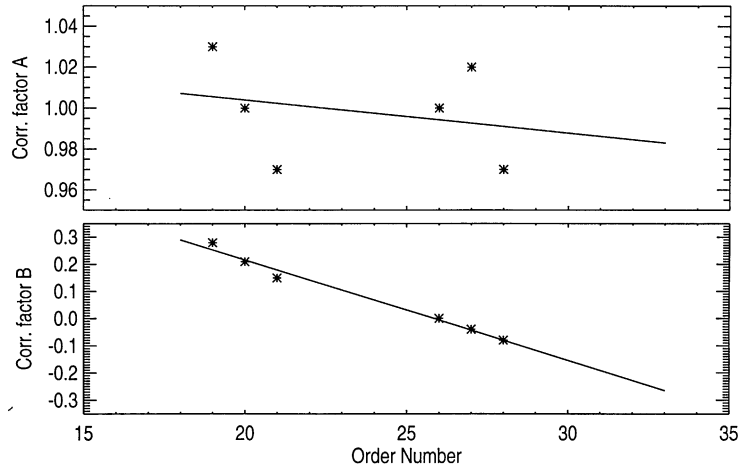


Figure 10: Fudge factors A and B for the 6 orders with good wavelength coverage. The lines show the least squares fit to the data and were used to determine the blaze functions for other orders.

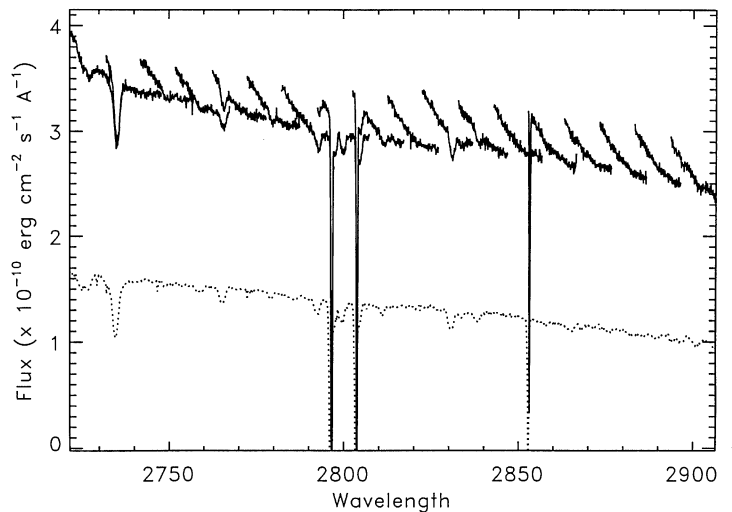


Figure 11: Overplot of the WSCAN data from order 20 after correcting for the blaze function. The reference spectrum, shown as a dotted line, has been displaced downward.

The results of the analysis are shown in figure 12. Repeating the analysis for the OSCANS taken at the high and low wavelength limits of each order produced vignetting functions which differed from the function presented in figure 12 by factors of up to 20 percent.

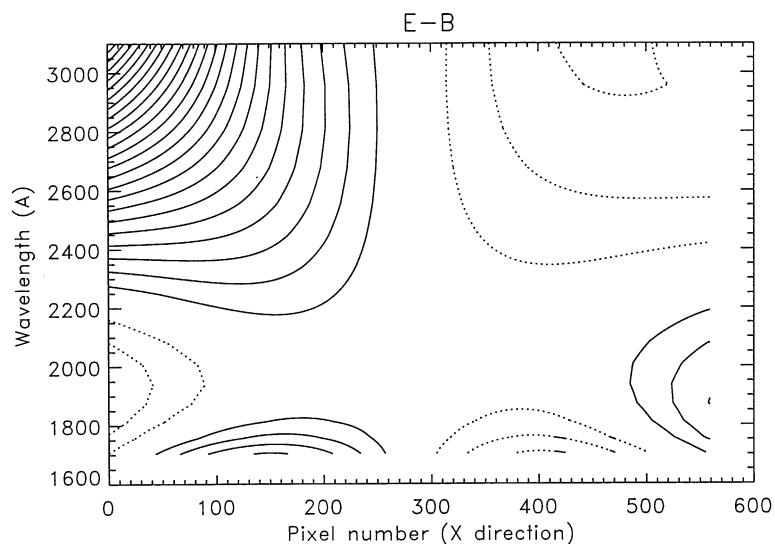


Figure 12: The vignetting function for echelle B as derived from data obtained from the central OSCAN. Details of the curves are as presented in Figure 5.

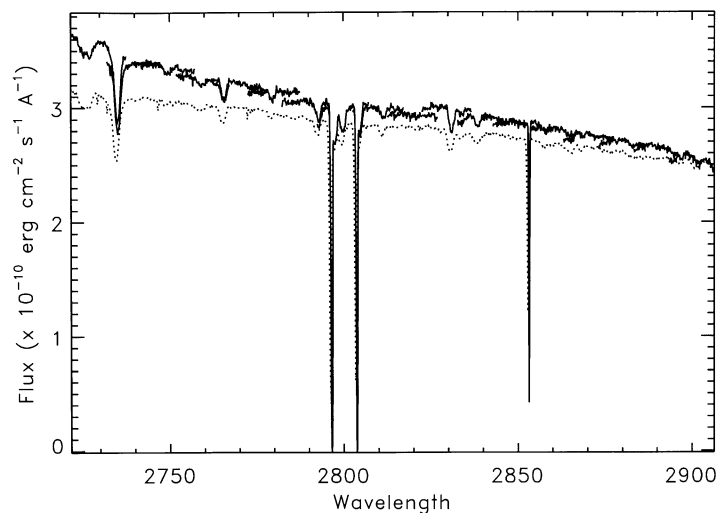


Figure 13: Overplot of the WSCAN data for order 20 after correcting for both the blaze function and vignetting. The reference spectrum (dotted) has been displaced downward slightly.

## Conclusions

Overall, the total, multi-dimensional sensitivity characteristics of the GHRS gratings are reasonably well understood and relative fluxes which are good to about 5 percent should be attainable on a regular basis. One of the primary existing problems with first order vignetting involves corrections near the ends of the array (i.e. near the edge of the photocathode), where the existing functions sometimes overcorrect or

undercorrect by as much as 10 percent. This is not always seen at a given wavelength and may result if the light from the star is not accurately centered on the diode array when observing with the LSA. A second difficulty involves vignetting for SSA data, since the majority of the calibration data was taken with the LSA and the two apertures do not view exactly the same portion of the photocathode at a given wavelength.

The echelle gratings still have difficulties due to the lack of calibration data. Echelle A has a rough sensitivity calibration, but no vignetting or on-orbit blaze function determination. Echelle B is better determined, but still has errors resulting from inadequate sampling. In figure 13 we show the effects of applying the full, multi-dimensional calibration to one of the echelle WSCANS. The dashed line shows the reference spectrum, which has been displaced from the echelle observation for clarity. While there is general overall agreement there are slight discrepancies, many of which probably result from errors in the vignetting function. It is hoped that calibration tests taken after the servicing mission will resolve these difficulties.

## Calibration of GHRS Burst Noise Rejection Techniques

E. A. Beaver<sup>1</sup>, R. D. Cohen<sup>1</sup>, A. Diplas<sup>1</sup>, H. Garner<sup>2</sup>, S. R. Heap<sup>3</sup>  
M. Loveland<sup>1</sup> and R. D. Robinson<sup>4</sup>

### Abstract

For observing very faint objects with the GHRS, the limiting magnitude is not only set by the instrumental sensitivity but by detector dark-noise. The measured average dark level for the D2 detector is 0.01 counts/sec/diode, the GHRS dark specification; almost all of the dark appears to be due to space radiation particle noise. We report here our calibration of the D2 burst noise rejection algorithm with the Proposal 4012 data set. For a FLYLIM setting of 1, where a frame sum of 2 counts or more is rejected, we find the average dark level reduced some 80 percent to 0.002 counts/sec/diode for 0.2 second frame times. In addition we have developed a signal-to-noise code that determines the optimum FLYLIM setting for a specific object signal level.

### I. Introduction

Radiometric tests of the GHRS instrument during Science Verification have shown that the GHRS is a very sensitive instrument. For observing faint objects, e.g. high-*z* quasars, the limiting factor is not so much sensitivity but detector dark-noise. The measured dark-noise on the GHRS detectors is due to space particle radiation. If we are to make use of this sensitive instrument on very faint objects, we must take all possible steps to lower the dark-noise level. In order to calibrate the GHRS burst noise rejection algorithms, Proposal 4012 was developed, entitled DARK-COUNT STATISTICS FOR GHRS DETECTOR D2. Proposal 4012 is designed to find out about how many times the diode array registers a 1 count, how many times 2 counts, etc. in the GHRS frametime. We report here our analysis of the data from Proposal 4012.

During extensive ground test activity, the GHRS detectors registered about  $2 \times 10^{-4}$  counts/sec/diode dark-count level at high voltage. However in the near-Earth orbit of the *HST*, the radiation environment elevates the Digicon detector dark-count level. The GHRS team has carried out extensive measurements of the particle radiation via Proposals 1407 and 1408 during science verification. These tests have served to describe the dark-counts as a function of *HST* position (latitude, longitude) and to give a dark-count rate for the D2 detector outside the SAA, varying from 0.007 counts/sec/diode at 0 degrees geomagnetic latitude to about 0.014 counts/sec/diode at

- 
1. CASS, University of California, San Diego, La Jolla, CA 92093-0111
  2. Ball Aerospace Systems Group, PO Box 1062, AR-1, Boulder, CO 80306
  3. Goddard Space Flight Center, Code 681, Greenbelt, MD 20771
  4. CSC, Goddard Space Flight Center, Code 681/CSC, Greenbelt, MD 20771

40 degrees geomagnetic latitude. For a long, multi-orbit observation, the GHRS dark-count averages out to about 0.01 counts/sec/diode, which is the original GHRS specification established at contract award in 1978; we are attempting to improve the GHRS limiting magnitude performance beyond specification.

Monte Carlo modeling of the GHRS detector dark-noise indicates that the predominant source of orbital noise comes from Cerenkov light flashes generated by cosmic rays transiting the Digicon faceplate (Beaver et al. 1991). The character of this noise is seen to be the essentially instantaneous formation of single counts on many diodes from individual cosmic ray induced light flashes in the faceplate (Rosenblatt et al. 1991). The Monte Carlo Cerenkov Model calculations further predict that the distribution of particle background events is very different from that of the Poisson distributed starlight and suggest a significant reduction in detector background will occur by the use of a rejection algorithm that is designed to take advantage of this difference. The GHRS rejection algorithm simply sums the number of counts in a frame of data and rejects the frame from the exposure sum if the sum is greater than a preset limit parameter. For faint objects and short frame times, most of the Poisson distributed signal frame sums are zeros or ones whereas a large percentage of the exponential-like distributed dark frame sums are greater than one.

Science Verification tests have also been done to see to what extent the dark-count rate could be lowered through use of the GHRS high speed (burst rejection in 10 microseconds) burst noise rejection circuit with the result that it reduces the dark-count rates by only 20 or so. The problem is that the counter can only detect bursts of particle radiation on the order of 8 or more photo-electrons, whereas the particle hit patterns generally come in smaller packets.

This possibility was not unexpected, and the flight software accordingly has means of rejecting data obtained in the ACCUM mode by comparing the sum of the counts on the diode array with the user-set threshold, FLYLIM, and discarding frames with sums greater than FLYLIM from the accumulation. This noise rejection technique was standard fare on the ground-based Digicons (Beaver et al. 1976), and so it was transferred to the GHRS flight software. In fact, the reason why we have a 200-ms frametime instead of 50-ms, as we initially wished, is to allow time for the NSSC-1 to do this frame-rejection.

The first astronomical use of the GHRS burst noise rejection technique occurred with observations of the star AU Mic (Woodgate et al. 1992 and Maran et al. 1993) where the authors searched the spectra for indications of flaring activity. These observers of AU Mic used the GHRS in the rapid readout mode at 0.4 seconds per frame with each frame sent to the on-board tape recorder. They applied burst noise rejection techniques on the data post-facto.

## **II. Proposal #4012 Data**

The dark-noise statistics proposal, #4012, was run in two parts. The first part was run on Side 2 in Oct 1992 and is composed of 6 *HST* orbits of rapid readout data with 0.35 second per readout frame. Only the first four orbits are analyzed here, since the last two orbits penetrated the SAA. Ideally we would have liked to monitor the

background by sending down frames every 200-ms and analyzing them. This data rate would require the 1-Mhz link, which is not available for long periods of time. Instead the dark was monitored every 350 ms, sending each frame of data to the tape recorder.

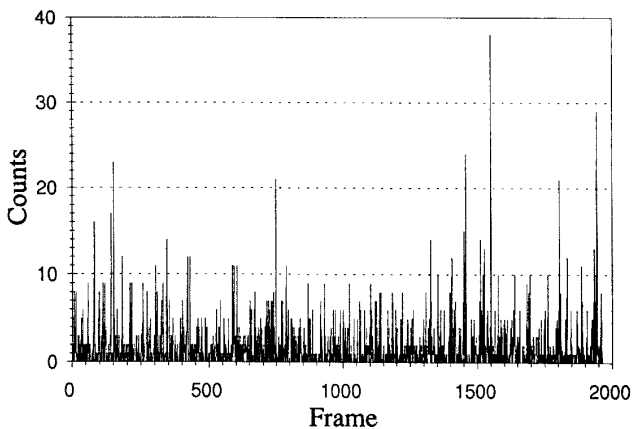


Figure 1: H5611 Frame Sums

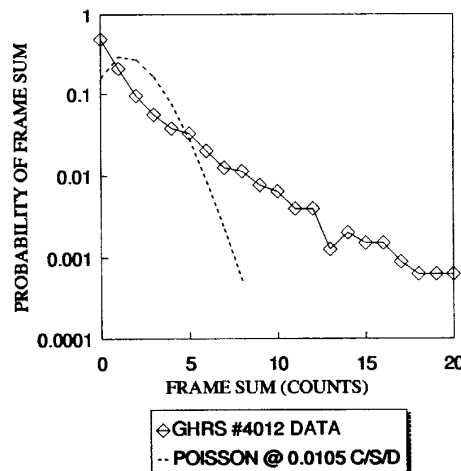


Figure 2: #4012 Dark Event and Poisson Distribution

Analysis of the 7864 frames of dark data gives the frequency distribution of the frame sums and allows prediction of SIGNAL/NOISE ratios for faint objects. The four orbits of data are located at entry numbers 5611 to 5616 in the GHRLOG. This observation is strictly internal dark-count. The carousel is at the safe position and the shutter is closed. No external light should reach the detector.

During this observation five diodes were turned off; they are diodes 110, 150, 279, 348, and 448, numbered starting from 1. Thus 495 science diodes are active. The frame sums for the first orbit (H5611) are displayed in figure 1. The distribution of frame sums for the entire data set is shown in figure 2, along with a distribution that would be expected from a Poisson distribution of frame sums at the 0.35 second framing rate and average dark rate. If the dark-count were due to photocathode thermionic emission, for example, it would be Poisson distributed. Clearly the distribution of frame sums for GHR# orbital dark-noise is non-Poisson in character. The largest frame sum in the data set is 138 counts!

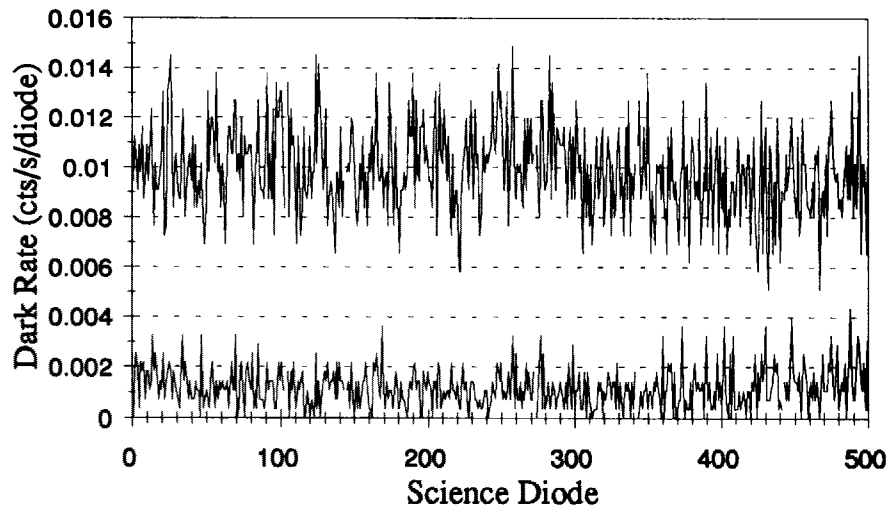
The average size of a non-zero frame sum is 3.5 counts. The average dark-count integrated over the four orbits is  $0.01057(\pm 0.00008)$  counts/sec/diode. Note that this small formal error is due to good counting statistics; another dark observation exposed over a different orbital track than 4012 could have a somewhat higher or lower average dark than the quoted 4012 dark level. Although a long exposure tends to average down the factor of 2 geomagnetic latitude variation in the dark rates, some smaller differences remain in the dark level for different orbit tracks.

**Table 1: #4012 Frame Distribution**

Frame Sum (Counts)	Fraction of Frames with Frame Sum	Fraction of Frames < Frame Sum	Fraction of Dark Counts < Frame Sum
0	0.49	0	0
1	0.21	0.49	0
2	0.096	0.70	0.12
3	0.056	0.79	0.23
4	0.038	0.85	0.33
5	0.032	0.89	0.42
8	0.011	0.95	0.64
10	0.00065	0.97	0.73

Statistical information from the experiment is listed in Table 1. Figure 3 shows the dark-count sum from this observation along with the dark-count sum with a frame sum rejection set at two or greater. As seen from Table 1, 49 percent of the 7864, 0.35 second frames have no dark-counts. For a setting of FLYLIM=1, the lowest meaningful setting, 70 percent of the frames are accepted; however the dark-count is

**FIGURE 3: #4012 DARK-COUNT FOR FRAME SUM >1 REJECTION AND WITHOUT REJECTION**



reduced to 12 percent of the full non-rejection value. As will be demonstrated in section 3, for FLYLIM=1, the fraction of time available for signal collection is the fraction of frames with no dark-counts. Thus for a faint object signal where 2 or more counts per frame is unlikely, we would expect the collected signal to be 49 percent of the full, non-rejection level for the 0.35 second frame time. Note, however, that the apparent count rate from the object will be lower than the rate without rejection

because additional time is spent counting single dark photons. Clearly a shorter frame time would be advantageous for better signal collection since the percentage of frames with no counts will increase with decreasing frame time. The second part of #4012, discussed next, addresses the need for faster framing by testing real time burst noise rejection at 0.2 seconds per frame.

The second section of GHR Side 2 #4012 was run in February 1993. It is a dark observation of 7 bins with 215 patterns per sub-exposure; this observation has six sub-exposures and the frame time is 0.2 seconds. FLYLIM was set to 1, which means frames with 0 or 1 counts in the ON-THE-FLY-ADDER (OTFA) are accepted; those frames with 2 or more counts in the OTFA are rejected. This observation is entry number 6037 in the GHR SLOG database. Figure 4 shows the exposure sum for all frames. The specified exposure time for this observation is 1806 seconds. However, a study of the observation logs shows that frame rejection increased the exposure time by 24.3 percent to 2245.4 sec. In other words, out of a total of 11227 frames, 2197 frames were rejected. To be consistent, we use this larger exposure time to calculate an average dark rate of  $0.00207(\pm 0.00004)$  counts/sec/diode for this FLYLIM=1 dark observation at 0.2 second frame time. The reduction in dark rate with FLYLIM=1 is certainly dramatic and on the order of 80. Successful operation of this observation shows that the flight software for a typical science observation with FLYLIM enabled works fine.

**FIGURE 4: #4012, PART 2 DARK WITH FLYLIM=1 AT 0.2 SEC. FRAME**

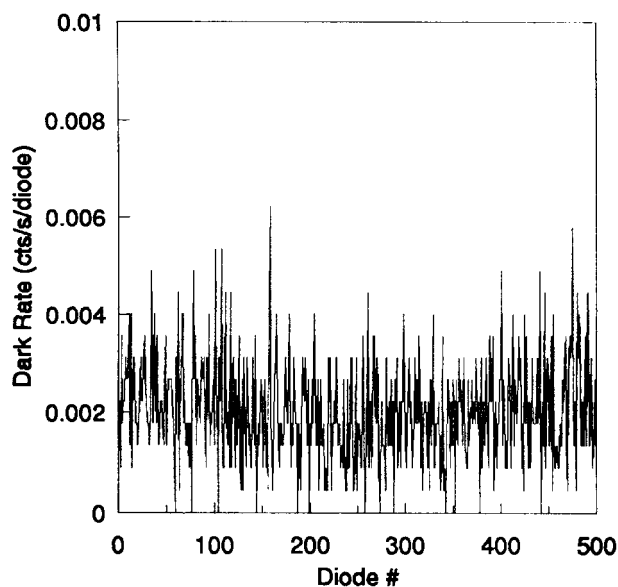


**Table 2: Science-to-Dark Ratios**

FLYLIM (counts)	Frame Time (sec)	Bkgd/Science (B/d)	Statistical Error ( $\pm$ )
1	0.20	12.2461	0.850
1	0.35	16.259	1.177
2	0.35	11.418	0.700
3	0.35	9.572	0.533
4	0.35	8.468	0.444
9	0.35	6.4848	0.293
19	0.35	5.6161	0.245
$\infty$	all	5.384	0.121

Additional information concerning the dark level comes from the large background diodes; proposal #4012 calibrates the response of the background diode dark sensitivity relative to the science diode dark sensitivity. At each end of the 500 diode science array are located two background diodes, situated above and below the axis of the science diodes. Each of the background diodes has geometrically 5 times the collection area of an individual science diode. In Table 2 we list the Background-to-Science Diode ratios (B/d) determined from our analysis, where

$$\frac{B}{d} = \left( \frac{\text{sum of 4 bkgd diodes}}{4} \right) / \left( \frac{\text{sum science diodes}}{495} \right) \quad (1)$$

Note that this ratio is a strong function of the FLYLIM setting and frame time. Of course our only calibration of B/d at 0.2 second frame time is at the FLYLIM setting of one.

Also as part of this effort we have analyzed all previous (up to 9/93) Proposal 1408 dark observations in order to find the best possible value for the normal B/d. This “no burst noise rejection” result is  $B/d = 5.384 \pm 0.121$  and represents some 140 minutes of dark observation time. The statistical uncertainty of 0.121 in B/d is larger than we would prefer since it alone can lead to an uncertainty in the science observation dark level equivalent to the faint signal level under investigation. Hopefully considerably more dark observations can be taken to improve the accuracy of B/d.

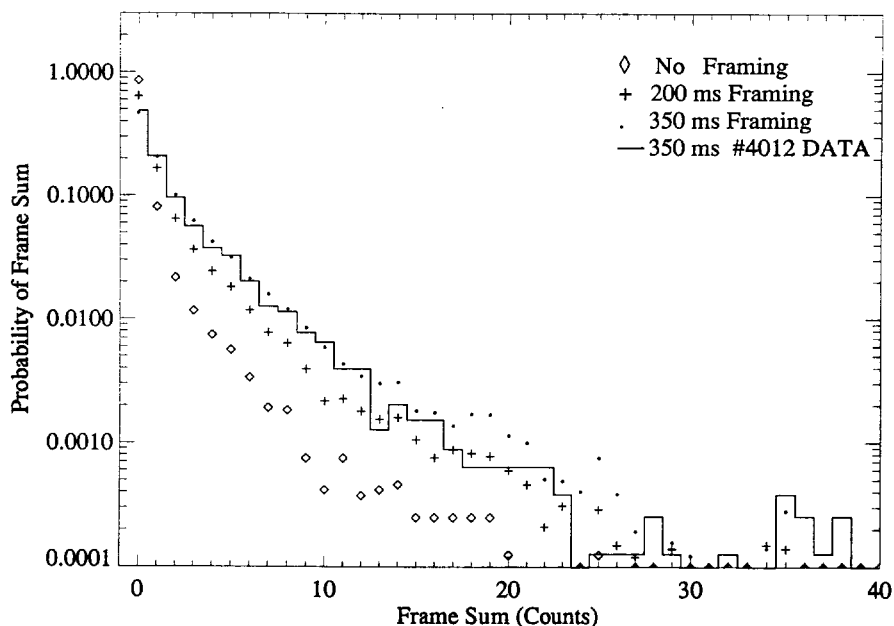
### III. GHRB Frame Rejection Signal to Noise Calculations

In the simplest case the signal to noise relationship for photon counting statistics is given by the equation in the GHRB Handbook:

$$(S/N)^2 = \left[ \left( \frac{s}{d} \right) / \left( \frac{s}{d+1} \right) \right] st \quad (2)$$

where  $s$  = object signal count rate,  $d$  = detector dark-count rate, and  $t$  = accumulation time for the observation. The dark event distribution statistics of Table 1 show that the dark-count rate can be significantly reduced and consequently S/N improved by rejecting frame sums above a preset limit; however, somewhat negating this S/N improvement is the loss of observation time and object signal caused by the rejection process. To accurately take these losses and gains into account and estimate the S/N improvement with frame rejection, we have developed a software S/N model based on the Table 1 results.

**FIGURE 5: S/N CODE DISTRIBUTIONS FOR NO, 0.2, & 0.35 SEC. FRAMING**



This S/N software model builds up two separate random number arrays, one for the dark frame count sums and the other for signal frame count sums. The object signal frame vector is easily filled by calls to the standard Poisson random number generator (Press et al. 1992). However, filling the dark-count array with random numbers distributed according to the Table 1, required programing a special random function, developed according to the “rejection method” (Press et al. 1992).

Since we also want to determine S/N improvement for other frame times than the 0.35 second framing, we have added a cosmic ray flux section to this S/N code. That is, the Table 1 distribution will change shape with frame time due to the different average number of cosmic ray induced Cerenkov events for a different frame time interval. We assume that the cosmic ray flux incident on the Digicon faceplate is Poisson distributed.

The S/N program flow is as follows: 1. The observation time, frame time, object signal level and detector dark level are entered into the program. 2. A frame loop is started to fill the dark and signal arrays. 3. For the frame number under consideration, a call is made to the cosmic ray Poisson random number generator to find the number of cosmic rays that transited the faceplate during the frame time. A call is then made

to the dark random number generator for each of these cosmic rays and the dark-count results are summed into the dark frame under consideration. 4. For the frame number under consideration, a call is made to the signal Poisson random number generator and the random signal result is placed in the signal frame under consideration. 5. The frame loop continues until the end of the observation time. 6. For each frame sum rejection level (FLYLIM), the Dark and Signal arrays are used to determine S/N from equation 2. 7. The optimum frame sum rejection level which maximizes S/N is determined.

Figure 5 shows the dark distributions determined from this S/N program for various frame times at the dark rate of 0.01 counts/sec/diode and an observation time of 20000 sec. Note in figure 5 the close approximation of the 0.35 second dark random number distribution to the actual distribution. However our S/N results for other frame times will be model dependent. The "no framing" distribution of Figure 5 is the distribution used in the dark random number generator and is constructed such that when used in the S/N Program with 0.35 second frame time, the observation 4012 frame distribution of Table 1 results.

As determined from our S/N code, Table 3 gives the optimum settings for FLYLIM for various object signal levels and frame times at a dark rate of 0.01counts/sec/diode. The fourth column, labeled "improvement," is given by  $(s/n)^2/(S/N)^2$  where s/n and S/N are the signal to noise with and without burst noise rejection, at the indicated FLYLIM setting. This improvement number indicates the factor by which observation time is reduced to get the same S/N as that case with no burst noise rejection. For a frame time of 0.2 seconds and object signal of 0.001 counts/sec/diode, the exposure time is one half that to obtain the same S/N without burst noise rejection. As the signal level increases to the dark rate the advantage of using burst noise rejection decreases. Note that decreasing the frame time also improves the S/N performance for burst noise rejection.

Maran et al. 1993 point out that the fraction of time available for signal measurement is the fraction of dark frames with no counts. Our S/N code gives the same result. For the very faint object signal of 0.0004 counts/sec/diode at 0.2 second framing, 64 percent of the signal is accepted, and is to be compared with 64 percent of the dark frames having no counts (see figure 5).

**Table 3: Optimum FLYLIM Setting for Various Object Signal Levels at a Dark Rate of 0.01 counts/sec/diode**

Object Signal "S" (c/s/d)	Frame Time (sec)	Optimum FLYLIM (Count)	Improvement	Signal Accepted (s/S)	Dark Accepted (d/D)	Time Lost $(1-t)/T$
			$\frac{(s/n)^2}{(S/N)^2}$			
0.0004	0.20	1	2.40	0.64	0.15	0.19
	0.35	2	1.88	0.67	0.22	0.22
0.001	0.20	2	2.00	0.80	0.27	0.12
	0.35	2	1.65	0.65	0.20	0.24
0.002	0.20	2	1.75	0.78	0.25	0.13
	0.35	3	1.50	0.75	0.29	0.18
0.003	0.20	2	1.56	0.76	0.24	0.14
	0.35	4	1.35	0.81	0.37	0.14
0.005	0.20	3	1.38	0.83	0.33	0.11
	0.35	5	1.24	0.84	0.42	0.12
0.0075	0.20	4	1.26	0.88	0.40	0.084
	0.35	6	1.15	0.86	0.47	0.10
0.01	0.20	5	1.18	0.90	0.47	0.067
	0.35	8	1.11	0.91	0.58	0.068
0.02	0.20	8	1.07	0.95	0.62	0.037
	0.35	12	1.04	0.95	0.68	0.043

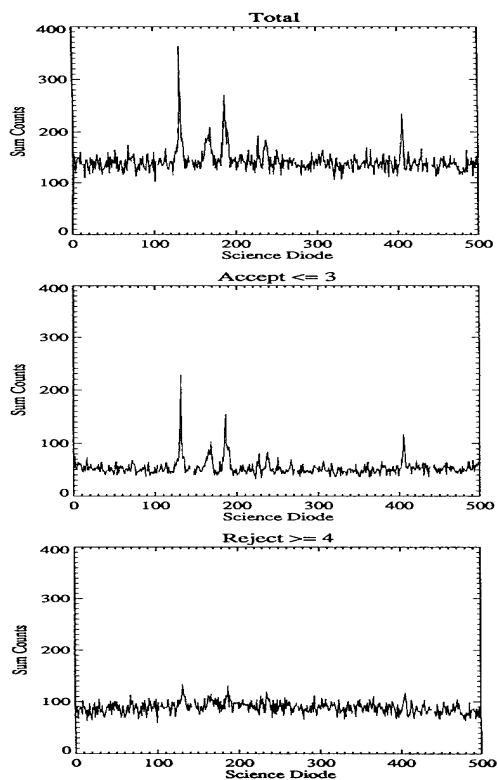


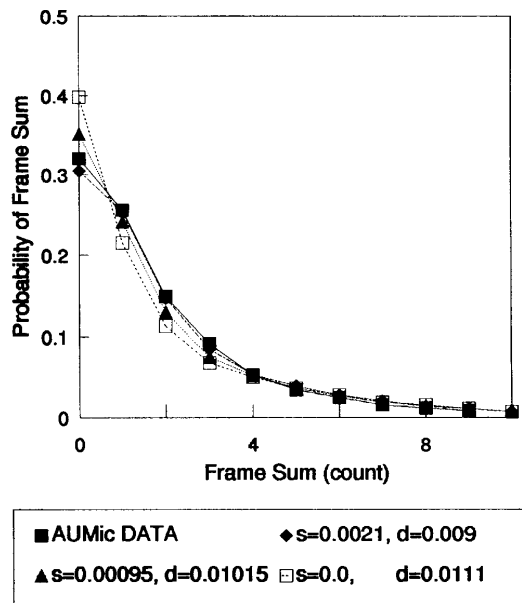
Figure 6: AU Mic star spectrum with optimal rejection.

#### IV. Rapid Readout Flare Star

As an example of the use of our results, we apply them to an existing (Maran et al. 1993) rapid readout data set for the star AU Mic, a star known for flare activity. This specific application is only meant to be used for illustration. The top plot in Figure 6 displays the GHRs G160M spectrum of AU Mic (without burst noise rejection) centered at about 1360Å. This rapid readout data set is composed of 31962 frames at 0.4 second per frame.

**FIGURE 7: Comparison of AU Mic data with models at various signal levels:**

$s=0$  cts/s/d,  $d=0.0111$  cts/s/d  
 $s=0.00095$  cts/s/d,  $d=0.01015$  cts/s/d  
 $s=0.0021$  cts/s/d,  $d=0.009$  cts/s/d



We use the Background-to-Science diode ratio (5.38 from Table 2) along with the AU Mic Background diode count from the observation to calculate a dark level of  $0.01016 \pm 0.0012$  counts/sec/diode as seen by the science diodes. Since the average total count as measured by the science diodes works out to be 0.01110 counts/sec/diode, the signal level works out to be  $0.0009455 \pm 0.0012$  counts/sec/diode. The large uncertainty in the Background-to-Science diode ratio has caused an uncertainty in the signal level greater than the actual signal level.

Another possible approach for determining the signal level in the data total is to compare the data distribution with model distributions generated by our S/N code for various percentages of signal and dark levels. The results of this approach are shown in figure 7. For the lower frame sum counts, the shape of the distribution is very sensitive to the signal and dark percentages. Note that before we would take this technique very seriously, we want to further investigate the stability of dark distribution data for different orbits and the degree of predictive accuracy of our S/N code.

However, for this illustrative work, we take the signal level to be  $\sim 0.002$  counts/sec/diode, the best curve fit in figure 7; the dark level works out to be 0.0091 counts/sec/diode. Our S/N code gives the optimum FLYLIM=3 for these signal and dark level settings, where 73 percent of the signal is accepted and the dark is reduced to 28 percent of the normal level. The middle plot in figure 6 is the AU Mic spectrum for FLYLIM=3. We see a significant reduction in diode-to-diode variation and the possible presence of additional weak features in the AU Mic spectrum when frame sum rejection is used. The bottom curve of figure 6 is the difference between the top and middle curves of figure 6.

**FIGURE 8: AU Mic spectrum with dark subtracted, corrected for signal loss, and divided by observation time.**

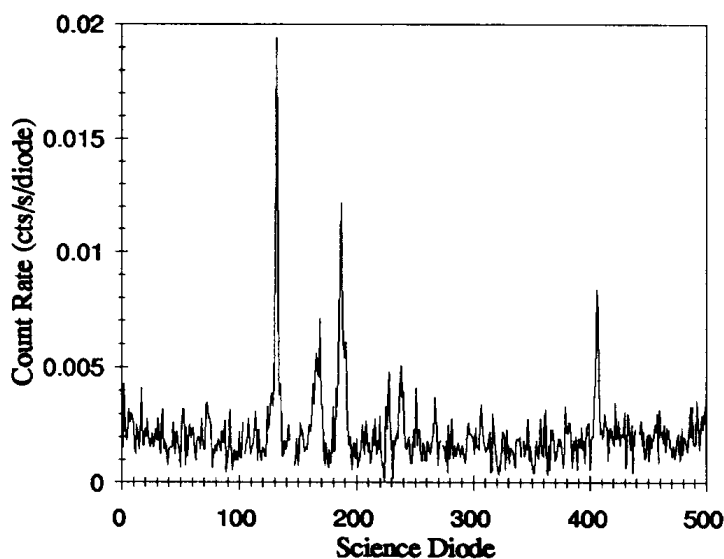


Figure 8 shows the “calibrated” AU Mic data, for FLYLIM=3, with a dark constant subtracted, a correction for signal loss, and division by the observation time. The dark level constant is determined by our S/N code to be 28 percent of the original dark level of 0.0091 counts/sec/diode. The spectrum is then corrected for signal loss, caused by burst noise rejection, by dividing the data by the factor of 0.73, also determined by the S/N code. Note that without this signal correction, object flux is not conserved, when using burst noise rejection.

### **Acknowledgment**

This work is supported by NASA - NAG5-1858.

## **References**

- Beaver, E. A., Harms, R. J., and Schmidt, G. W. 1976, Sixth Symposium on Photoelectron Image Devices, in *Advances in Electronics and Electron Physics*, ed. B. L. Morgan, 40B, 751.
- Beaver, E. A., Baity, W. A., Brandt, J. C., Ebbets, D. C., Garner, H., Heap, S. R., Lindler, D. J., Linsky, J. B., Lyons, R. W. and Rosenblatt, E. I. 1991, 10th Symposium on Photoelectronic Image Devices, in *Photoelectronic Image Devices*, ed. B. L. Morgan, 121, 65.
- Maran, S. P., Robinson, R. D., Shore, S. N., Brosius, J. W., Carpenter, K. G., Woodgate, B. E., Linsky, J. L., Brown, A., Byrne, P. B., Kundu, M. R., White, S., Brandt, J. C., Shine, R. A., & Walter, F. M. 1993, *Ap. J.* [in press].
- Press, W. H., Teukolsky, S. A., Vetterling, W. T., Flannery, B. P. 1992, *Numerical Recipes in Fortran*, Cambridge University Press, 281.
- Rosenblatt, E. I., Beaver, E. A., Cohen, R. D., Linsky, J. B., Lyons, R. W. 1991 *SPIE Proceedings on Electron Image Tubes and Image Intensifiers II*, ed. I. P. Csorba (Bellingham, WA: SPIE) 1449, 72.
- Woodgate, B. E., Robinson, R. D., Carpenter, K. G., Maran, S. P., and Shore, S. N. 1992, *Ap. J.*, 397, L95.

## **Dark Count Statistics for GHRS Detectors: A Test of Noise Rejection with FLYLIM**

Lisa E. Sherbert<sup>1</sup>, Stephen J. Hulbert<sup>1</sup>, Ronald L. Gilliland<sup>1</sup> and Joseph P. Skapik

### **Abstract**

GHRS calibration proposal 4012 was designed to obtain the statistical data needed to plan an operational strategy for observing faint targets with the GHRS. The FLYLIM noise rejection strategy is potentially of most use when one is observing an object so faint that source counts are well below the level of the detector dark count. In that case it is possible to reject multiple-count integrations as instances of higher-than-average noise without the risk of discarding exposures containing genuine signal. The data obtained in proposal 4012 show that when FLYLIM count rejection is used on the GHRS Detector 2 the dark noise is reduced by a factor of four (4) over what is seen well outside the South Atlantic Anomaly (SAA). The rejection of some lines of data resulted in an increase in execution time by about 25 percent over the nominal exposure time.

### **I. Introduction**

Observations obtained in GHRS calibration proposal 4012 were designed to obtain the statistical data needed to plan an operational strategy for observing faint targets with the GHRS. The proposed test involved only the use of Side 2, since only this side of the GHRS can benefit from the results of this test at the present time. Due to the loss of the GHRS low-resolution mode (with G140L on Side 1), most observing programs that had originally specified G140L have been changed to use G160M instead. These programs then see an overall higher dark count rate since the SV-measured GHRS background at 0° geolatitude for the Detector 1 was 0.005 cts/s/diode, but for Detector 2 it was 0.008 cts/s/diode (Ebbets 1991). Hence, the problem of reducing the GHRS dark-count has become even more acute. The FLYLIM<sup>2</sup> noise rejection strategy is potentially of most use when one is observing an extremely faint object—one that is so faint that source counts are well below the level of the detector dark count. In that case it is possible to reject multiple-count integrations as instances of higher-than-average noise without the risk of discarding exposures containing genuine signal.

For GHRS calibration proposal 4012, dark count observations in RAPID<sup>2</sup> and PHOTOSCAN<sup>2</sup> modes were taken at various times. The RAPID observations provide lines of raw, unprocessed data every 0.35 seconds for the period of the exposure, providing statistical data on the distribution of bursts of counts produced by particle

---

1. Space Telescope Science Institute, Baltimore, MD 21218

2. see Proposal Instructions

radiation. With these statistics, methods of noise removal can be evaluated. The PHOTOSCAN dark observation had the onboard data quality check FLYLIM enabled to discard every line of data that had more than one count total in the 0.2 second STEP-TIME<sup>1</sup> integration period. The observations relayed to the ground were the summation of all lines of data that had one or zero counts. This observation achieves the lowest dark count available with onboard data processing with very faint targets. The primary purpose of this proposal was to evaluate achievable dark count rates for Detector 2, although originally it was intended for Detector 1.

Both observations were scheduled relative to the South Atlantic Anomaly. Evaluation of the data depends upon knowing the radiation environment. The RAPID observation started well before the entry into the SAA, to provide statistics during the quiet part of the orbit. This observation ended in the SAA to allow evaluation of dark count statistics as the radiation increased, see Figure 1 which is explained in the next section.

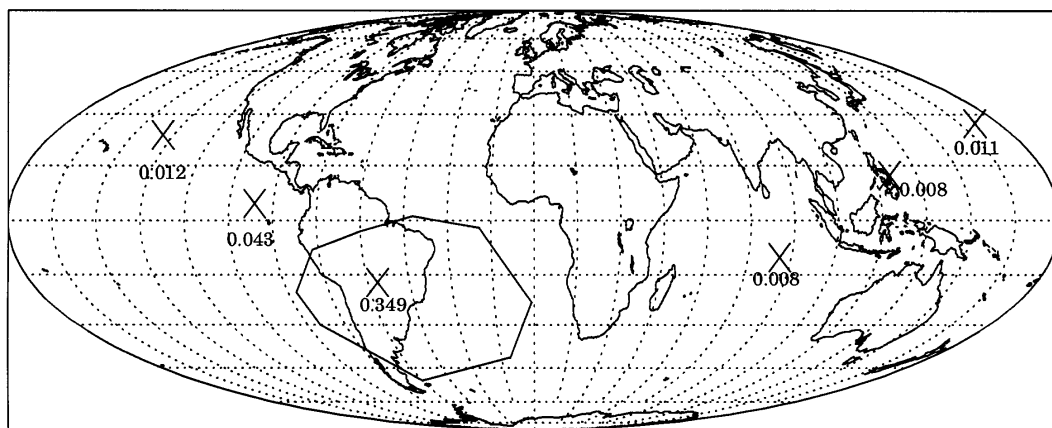


Figure 1: Rapid mode observation locations and mean dark count rate in cts/sec/diode.

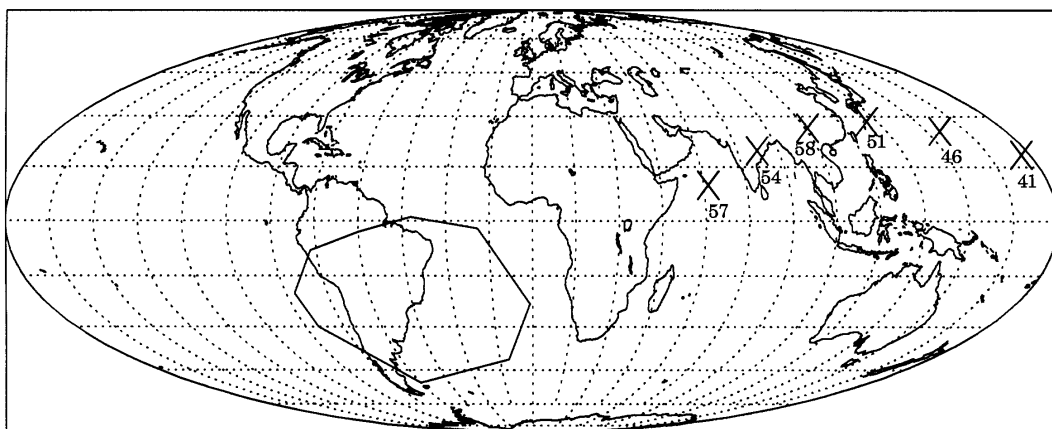


Figure 2: Photoscan mode observation locations and number of extra pattern repeats.

The PHOTOSCAN observation was designed to measure the ultimate achievable dark count using onboard data processing and was run in a quiet portion of the orbit. The PHOTOSCAN observation required special handling to set the value of the

1. see Proposal Instructions.

OTFA (on-the-fly-adder) acceptance limit, FLYLIM. The default setting for FLYLIM is the maximum possible value of 33554431 to disable this feature. For this test the value of FLYLIM was set to one to force rejection of all multiple count lines of data, see Figure 2.

The following special scheduling requirements were imposed:

1. All observations used orbits which include SAA passages.
2. For the RAPID mode exposures, the observation began 50 minutes before crossing the western boundary of the SAA.
3. For the PHOTOSCAN mode exposures, the observation began 45 minutes after crossing the western boundary of the SAA.
4. Rejection of multiple count data in PHOTOSCAN observations can increase execution time by 50 percent of exposure time for Detector 2. No schedule adjustments are required since the only the last sub-exposures will be lost.

## II. Data

Table 1 contains the list of the rootnames for this observation. The first six data sets are the Rapid mode data; the last is the Photoscan data.

Figure 1 is a Mollweide projection of the world with the SAA drawn in. The location of the first group of each of the Rapid mode data sets is indicated with an X. The Rapid observations began over the Indian Ocean and proceeded to the East, ending in the SAA. Underneath each X is the average dark count rate (in cts/s/diode) for all 1,963 groups in the calibrated data set.

**Table 1: 4012 Data Sets**

Rootname	Date
z14n0101t	19 Oct 92
z14n0102t	19 Oct 92
z14n0103t	19 Oct 92
z14n0104t	19 Oct 92
z14n0105t	19 Oct 92
z14n0106t	19 Oct 92
z14n0201t	6 Feb 93

Likewise, Figure 2 is the same projection with the start of the PHOTOSCAN exposures indicated with an X. The exposures begin in the East and proceed westward. Under each X you will find the amount of extra time required to collect the data (due to the setting of FLYLIM) expressed as a percent difference. The proposal request for 6 exposures of 300 sec each translates into a data set consisting of 42 bins,

every 7 bins being the nominal 300 sec exposure. Since turning on FLYLIM leads to the discarding of some data, the actual time required to collect the 7 bins is greater than 300 sec because the pattern has to be repeated until the 300 sec exposure time is reached, see Table 2.

**Table 2: Comparison of Observation Times to Nominal Exposure Times**

UDL Packet Times (MJD)		Difference in Packet Times (seconds)	Percent Difference over Nominal Duration of 301.8s	Calculated Number of Patterns Executed	Number of Patterns over Nominal of 215	Percentage of Extra Patterns
First	Second					
49024.025	49024.029	382.119	26.6	272	57	26.7
49024.029	49024.033	377.379	25.0	269	54	25.1
49024.033	49024.038	383.999	27.2	273	58	27.3
49024.038	49024.042	373.999	23.9	266	51	24.0
49024.042	49024.047	367.249	21.7	261	46	21.7
49024.047	49024.051	360.379	19.4	256	41	19.5
Average Percent Differences			24.0			24.0

### III. Analysis

Diodes 342 and 442 were misbehaving during the RAPID mode observations since RAPID observations skip the normal diode quality processing. In order that their out-of-range values not dominate the statistics, both values were changed to zero before the data were processed. The STSDAS software could have filtered out these diodes itself, but it calculates the mean dark count before determining which diodes are out of range.

Table 3 lists the mean dark count statistics as calculated by the STSDAS task, darkstat for each of the rootnames in Table 1.

**Table 3: Dark Count Statistics**

FLYLIM Rejection Used?	Rootname	Mean	Sigma
No	z14n0101t	0.008	0.149
	z14n0102t	0.008	0.152
	z14n0103t	0.011	0.180
	z14n0104t	0.012	0.185
	z14n0105t	0.043	0.351
	z14n0106t	0.349	0.938
Yes	z14n0201t	0.002	0.007

If the numbers in Table 3 and in Figure 1 are compared to the locations of the observations with respect to the SAA, you can see that the dark count steadily increases as the telescope approaches the SAA. You can also see from above that the mean dark count for the FLYLIM observation is one-quarter that for the normal dark observations well away from the SAA.

One can calculate the nominal exposure time for the PHOTOSCAN observation without the FLYLIM rejection (or if none of the bins of data contained greater than 1 count). The nominal duration is:

$$0.8 \text{ sec} + (7 \text{ bins/patt}) \times (0.2 \text{ sec/bin}) \times (215 \text{ patt}) = 301.8 \text{ sec},$$

where 0.8 sec is the overhead required for the PASS deflections which clear the buffer and the end of an exposure, 0.2 sec/bin is the STEP-TIME, 7 bins/patt is the number of groups per exposure, and 215 patterns are needed to get the requested exposure time.

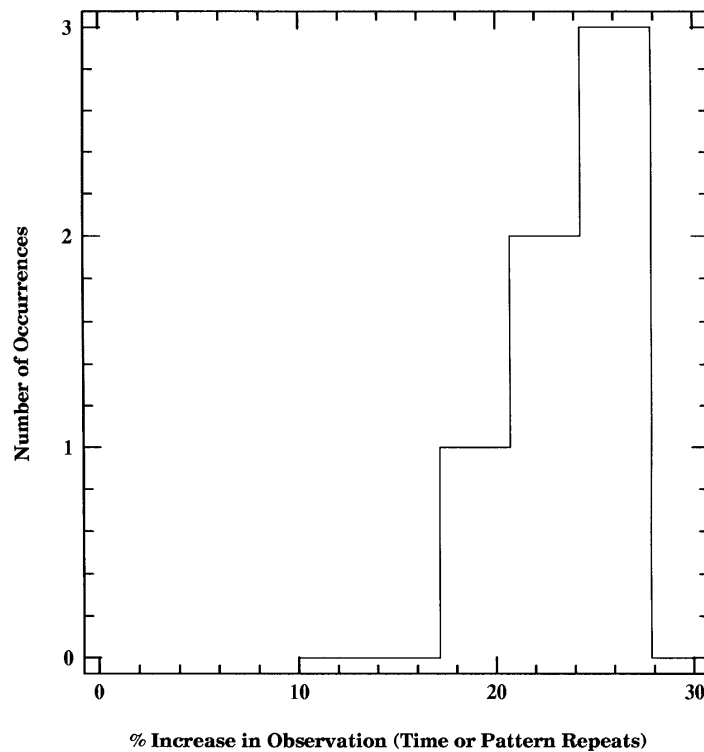


Figure 3: Histogram of percent differences.

There are two ways to view the effects of the setting of FLYLIM. In the first, we calculate the observation duration from the difference in the Unique Data Log (UDL) Packet times. (UDL dumps occur right before and right after the taking of the science data; the dumps are time-tagged.) We then compare that duration to the nominal duration to see how much extra time was used. Alternately, we can substitute the observation duration for the nominal duration in the above equation, and calculate the number of patterns which were actually executed. Table 2 shows the results of both calculations, which agree quite well.

Figure 3 shows a histogram of these percentages. While the average increase to the exposure in time or repeats of patterns is 24 percent, the distribution for the six observations ranges up to 27 percent.

### **Conclusions**

Using FLYLIM noise rejection well outside of the SAA can reduce the dark noise in GHRS Detector 2 by a factor of 4 while increasing the observation time by only about 24 percent on average. For routine operational use, the exposure times should be padded by an amount on the order of 30 percent of the nominal exposure time to ensure that the observations complete.

### **References**

Ebbets, D. GHRS Science Verification Report. May 1991.

# **Attaining High Signal-to-Noise Data with the Goddard High Resolution Spectrograph**

Jason A. Cardelli<sup>1</sup> and Dennis C. Ebbets<sup>2</sup>

## **Abstract**

We present an analysis of the characteristics of fixed pattern noise and photocathode granularity in the detector system of the Goddard High Resolution Spectrograph and the impact this noise can have on science data. We show that through the application of some basic and straightforward observing and data reduction techniques, this instrumental noise can be effectively suppressed, allowing high signal-to-noise (S/N) data to be achieved. Using these techniques, numerous examples of spectra with  $S/N \approx 300 - 1000$  have thus far been obtained. Analysis of the noise characteristics of these high S/N spectra also show the data to be essentially at the photon-limit.

## **I. Introduction**

The high resolution (3.5 km/sec) and linear photon-counting detector capabilities of the Goddard High Resolution Spectrograph (GHRS) offer a fantastic opportunity to obtain superb spectroscopic data, unprecedented in the history of satellite UV spectroscopy. However, as is the case with many detector systems, especially those employing photocathodes, the detector system of the GHRS is plagued by fixed pattern noise. The presence of such noise effectively limits the signal-to-noise (S/N) that can be obtained in a single exposure at a fixed grating position. While the GHRS detector system noise does not inhibit work on moderate-to-strong absorption lines (i.e., > 10 percent deep), its effects can be devastating for weak lines (< 5 percent deep). Weak line work is important because it provides a unique opportunity to study weak transitions from important abundant species (Cardelli et al. 1991; Cardelli et al. 1993b; Cardelli and Ebbets 1994) as well as the strongest transitions from species with very low cosmic abundance (Cardelli, Ebbets, & Savage 1991; Cardelli et al. 1993a; Hobbs et al. 1993; Federman et al. 1993).

In this paper we present an analysis of fixed pattern noise and its potential impact on science data. We show examples of its variability with wavelength and how the analysis of the noise characteristics can be affected by such things as Doppler compensation. We also provide a generalized discussion of some simple and straightforward observing and data reduction techniques that can be used to suppress fixed pattern noise and granularity to below that of the photon noise.

---

1. Department of Astronomy, University of Wisconsin, Madison, WI 53706

2. Ball Aerospace Research Group, Boulder, CO 80306

## II. Fixed Pattern Noise/Photocathode Granularity

### General Characteristics: Side 1 and 2

The noise in the GHRS detector system arises from two major sources: 1) fixed pattern noise features resulting from scratches and manufacturing marks present in the photocathode window and 2) granularity and non-uniformities in the photocathode. Additional contributions arise from particulate contamination. Examples of the detector system noise are shown in Figure 1 for side 1 (CsI photocathode deposited on a LiF window) and side 2 (CsTe photocathode deposited on a MgF<sub>2</sub> window) detector systems. The data were obtained with G140M and G160M using STEP-PATT=4 which produces 2 samples (pixels) per science diode. As seen in the figure, with the exception of a few notable broad and deep features, the fixed pattern noise features are generally narrow and have a typical depth of a few percent. The photocathode granularity is much less pronounced, being characterized by weak oscillations typically  $\leq 1$  percent in depth. The S/N values correspond to expected values from photon statistics. The data are of such high quality that essentially every feature seen in the spectra can be attributed to detector system noise.

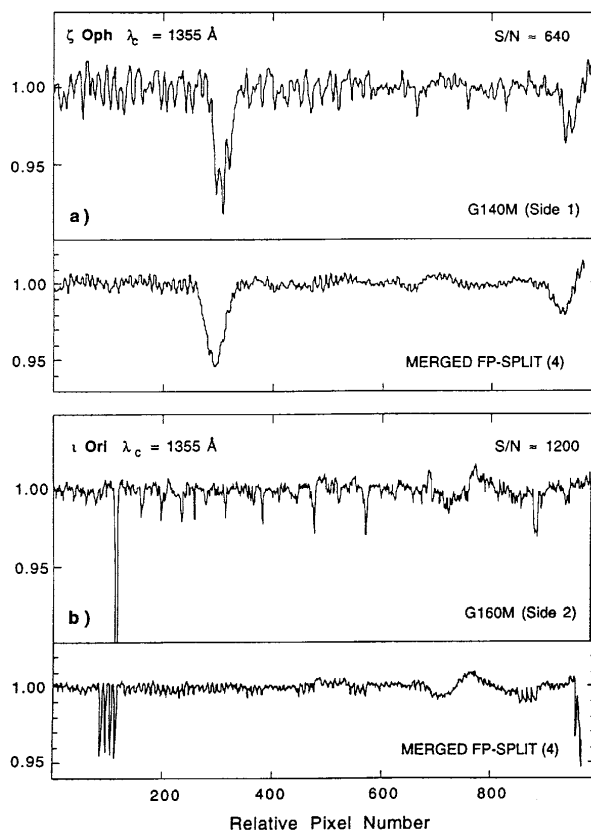


Figure 1: Examples of fixed pattern noise/photocathode granularity spectra derived from data obtained at a setup wavelength of 1355 Å for **a)** G140M (side 1) data of  $\zeta$  Oph and **b)** G160M (side 2) data of  $\iota$  Ori. The S/N values listed represent the values expected from photon statistics. Consequently, essentially all the structure seen in the noise spectra result from fixed pattern and photocathode granularity sources. The bottom panels in both **a)** and **b)** show how the noise would impact science data if the FP-SPLIT subexposures were simply aligned and merged in wavelength space.

*Wavelength-Dependence*

Scratches, blemishes, and non-uniformities in the GHRS detector system are geometrically distributed throughout the 2-dimensional detector window. Consequently, specific noise features present in any observation will be a function of where the spectrum falls on the window. For first order gratings, the spatial location of the spectrum in the direction perpendicular to the dispersion (Y-position) is relatively well fixed, ignoring thermal and magnetic drifts. However, in the echelle modes, each order will have a different Y-position and so the noise structure may change dramatically from one order to the next (different orders are observed by magnetic deflection onto the Digicon detector).

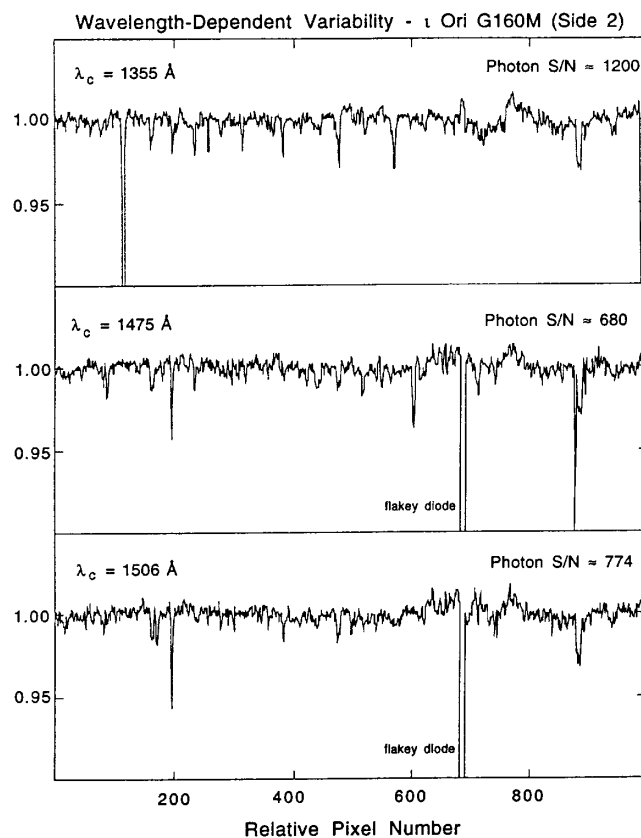


Figure 2: Examples showing the variability exhibited by fixed pattern noise as a function of wavelength for data of  $\iota$  Ori obtained with grating G160M (side 2) at 1355 Å, 1475 Å, and 1506 Å. The S/N values shown have the same meaning as in Figure 1. The bottom two panels indicate that even relatively small changes in the setup wavelength can have profound effects on the noise spectrum.

Figure 2 shows an example of noise spectra obtained at three different setup wavelengths from G160M data of  $\iota$  Ori. The data were obtained with STEP-PATT=4. Close examination shows that with few exceptions (e.g., the broad noise feature near pixel 900) the noise features show considerable variation with wavelength with some varying in strength (e.g., the feature near pixel 200) and others appearing in only one of the spectra (e.g., the feature near pixel 600). Sources of this variation may include wavelength sensitivity of the noise features, Y-position displacement of the spectrum from one wavelength setup to the next, or particulate contamination.

### III. Noise Assessment

#### *Suppression/Removal Procedures*

For an observation obtained at a single grating setup position, the data in Figure 1 show that the best one could possibly hope to do (in regions away from the strong noise features) is about  $S/N \approx 50$  on either side 1 or 2. When the GHRS commanding was designed, an optional procedure called FP-SPLIT was created to specifically to deal with the presence of noise structure.<sup>1</sup> This procedure breaks each requested observation into a number of subexposures (the default is 4), each obtained at a slightly different grating tilt which shifts spectral features relative to the fixed pattern noise. When individual subexposures are aligned in wavelength space, the noise features in each subexposure are offset by about 4.5 diode widths. When the data are merged, the impact of the noise is significantly reduced, as seen in the bottom panels in Figure 1. However, the maximum S/N is still restricted to values less than about 150.

To achieve significantly higher S/N values, one must effectively derive a flat-field template which can be used to significantly reduce the noise structure to at or below that of the photon noise. The procedure we have adopted is shown in a flow chart in Figure 3. It involves an iterative procedure in which 1) a spectrum template is determined by aligning the spectral features and combining the subexposures, 2) the spectral template is divided into the original subexposures, 3) a noise template is determined by aligning the noise features and combining the subexposures, 4) the noise template is divided into the original subexposures, and 5) the process repeats with step 1). This procedure works because in each subexposure, there is a different offset between any particular spectral and noise feature.

An example of the application of the procedure outlined in Figure 3 is shown in Figure 4 for data of  $\iota$  Ori. The first three spectra show the derived noise template, the raw (uncorrected), and the corrected data for the first (left panel) and fourth (right panel) FP-SPLIT subexposure, plotted against pixel number. Note that between the two subexposures, the spectral features have moved in pixel (detector) space while the noise features have stayed essentially fixed in pixel space. Note how well the strong noise features are removed when the data are divided by the template (the same is found for the other 2 FP-SPLIT subexposures). The bottom two spectra are the same in each panel and represent, 1) addition of the four corrected FP-SPLIT subexposures and 2) addition of four separate observations (16 FP-SPLIT subexposures). The S/N values listed were empirically derived from the continuum and are essentially the same as what is predicted from photon statistics.

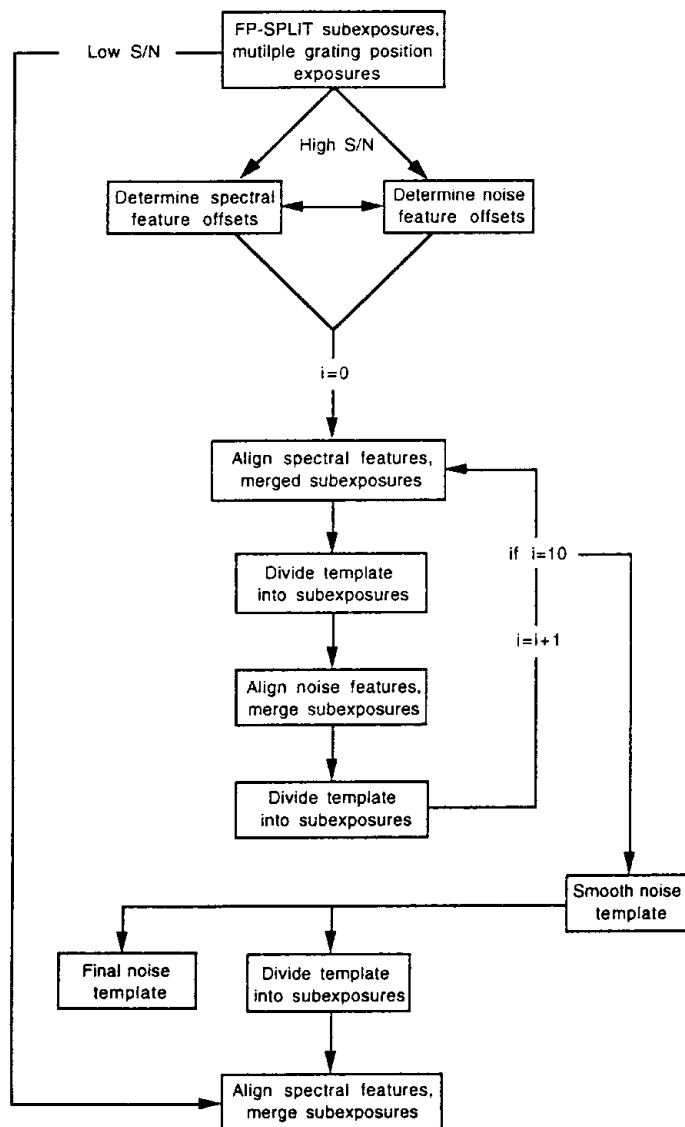
#### *The Impact of Doppler Compensation*

For the small wavelength shifts produced by the procedure FP-SPLIT, no significant change in the noise structure is seen and all noise features should appear fixed in pixel (diode) space. However, because the velocity of the spacecraft relative to the target changes due to orbital motion, a spectrum obtained at some arbitrary grating

---

1. See GHRS Handbook for a discussion of FP-SPLIT and other instrumental settings.

## Fixed- Pattern Noise Suppression/Removal Procedure



For multiple grating tilts, spectral features will appear at a different reference pixel (diode) position in the individual subexposures. In the absence of orbital motion, noise features should appear at the same reference pixel position. However, the required use of the Doppler compensator means that noise features will appear to 'drift' slightly in pixel space. Thus offsets in pixel space of both spectral and noise features must be computed.

The steps outlined here describe the logic behind how the software computes a noise template through an iterative procedure. Analysis of the procedure has shown us that nothing is gained by performing more than 10 iterations.

Smoothing of the noise template is an option open to the user, but should be restricted to  $\leq 1$  spectral resolution element. We have found that smoothing on a larger scale can suppress narrow noise features leading to incomplete removal

In most applications, division by the 'final' noise template sufficiently removes the features so that the final merged spectrum is characterized by photon noise only.

Figure 3: A flow chart showing the logical steps involved in processing GHR data for fixed pattern noise. The low S/N channel can be applied in cases where the desired spectral feature is in a region characterized by 2 – 3 percent deep features *only* and the maximum S/N expected from photon statistics is  $< 150$  (see the bottom panels in Figure 1).

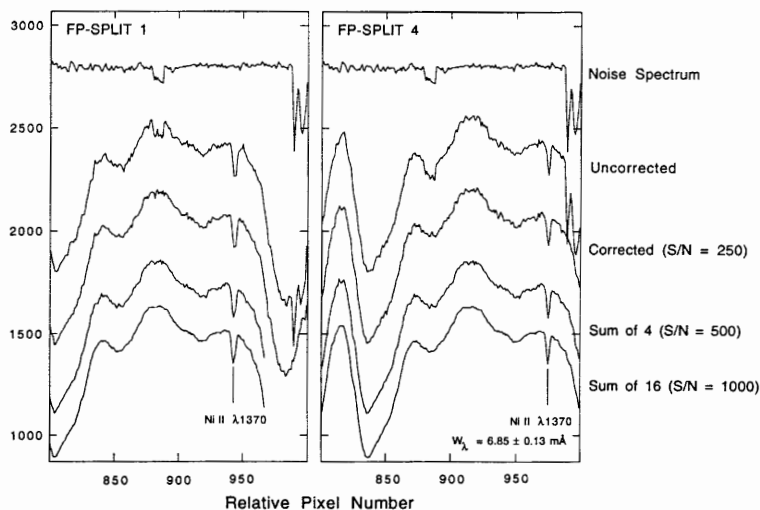


Figure 4: An example of the removal of fixed pattern noise from a portion of 2 FP-SPLIT subexposures of  $\iota$  Ori. The noise template was determined using the steps outlined in Figure 3. The effects of the major noise features are clearly seen in the raw (uncorrected) spectra. The corrected spectra result from dividing the derived noise template into the raw (uncorrected) spectra. The sum of 4 spectra correspond to the merging of the four noise-corrected FP-SPLIT subexposures. The bottom spectra result from merging four separate observations (total of 16 FP-SPLIT subexposure). The S/N values were empirically derived from the continuum and are essentially the same as what is expected from photon statistics.

position can shift by a maximum of  $\pm 8$  km/sec in 80 minutes (about  $\pm 1/2$  diode in intermediate resolution and about  $\pm 2.3$  diodes in high resolution). Since each subexposure is broken into many individual integrations which are dumped into the on-board accumulator bins, the Doppler compensator is used to apply the velocity shifts to each spectral integration prior to it being stored so that the spectral features do not become smeared in wavelength space. In addition to producing a small smearing of the noise features in each subexposure, comparison of the individual subexposures shows that the noise features can exhibit some drift in pixel space (in deriving the noise template, drifts of the noise structure in pixel space are accounted for in the reduction procedure – see Figure 3). This drift is most pronounced in the high resolution echelle mode. An example of this is shown in Figure 5 for Echelle-B data of  $\zeta$  Oph in the neighborhood of a strong interstellar Mn II line. The movement of the spectral line between the FP-SPLITS (and relative to the noise structure) in pixel space is the result of different grating tilts and serves as the basis by which the noise template is derived.

In addition to a small and steady drift in time (the time sequence of the observations runs from top to bottom), the noise features in Figure 5 also show a sudden and substantial jump between the third and fourth subexposure (at FP-SPLIT position no. 2). This jump resulted from a long orbital interrupt of the observing sequence. When the exposure resumed, the velocity of the spacecraft relative to the star had changed by  $-10.5$  km/sec. Had the interrupt occurred *between* subexposures, all of the data would be usable. Unfortunately, the interrupt came with 20 percent of the time remaining on subexposure 3. When the observation continued, the noise features were shifted by  $-10.5$  km/sec which resulted in a significant degradation of

the noise structure in this subexposure relative to the others as can be seen in an examination of the data in panel b).

The data in subexposure 3 cannot be used in deriving the noise template and probably should not be used in the merged spectrum, especially if a major goal is to search for weak lines. In this case we have not lost much since it is only one of eight subexposures. However, the consequences would have been more serious had we only obtained one exposure in each FP-SPLIT position. Fortunately, this problem does not occur very often.

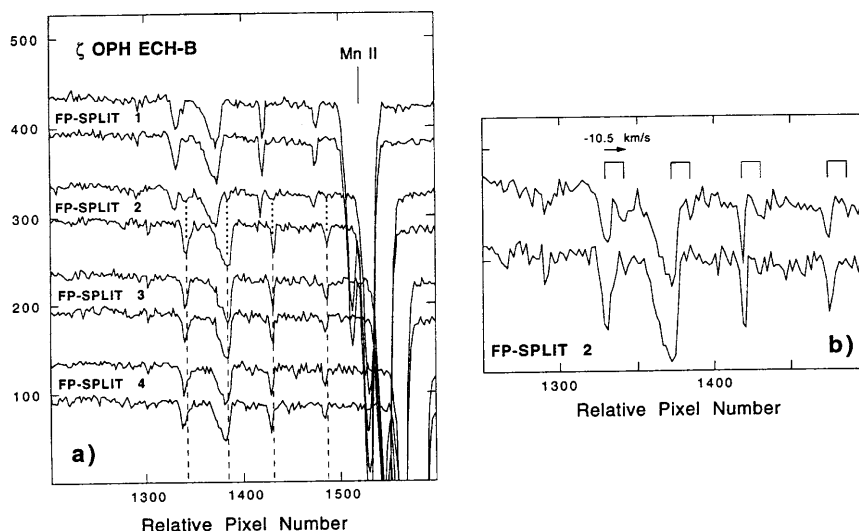


Figure 5: A portion of an echelle-B observation of  $\zeta$  Oph in the neighborhood of a strong interstellar line of Mn II, plotted in pixel space, is shown in panel a). The data were obtained with two subexposures at each of the four FP-SPLIT positions using STEP-PATT=7 (four samples per diode). The apparent movement of the fixed pattern noise features in pixel (detector) space is the result of the Doppler compensator. The jump in the features between subexposures 3 and 4 result from an orbital interrupt prior to the completion of subexposure 3. Panel b) shows that the subexposure resumed at a point in the orbit when the component of the orbital motion in the direction of the star had changed by  $-10.5$  km/sec.

### *High Signal-to-Noise Science Data*

To date, the techniques outlined here have been used on data obtained in a number of different programs to produce high quality spectra with  $300 \leq S/N \leq 1200$ . Some examples of results produced for weak absorption lines are shown in Figure 6. The S/N values were measured from the continuum and are consistent with the data being in the photon limit.

### *Residual Noise Characteristics*

Our statement that our results are essentially in the photon-limit derives from the fact that the empirical S/N values are the same as those obtained from (total counts)<sup>1/2</sup>. To explore this further, it is useful to actually examine the noise structure to see if it behaves according to Poisson statistics (e.g., the noise is characterized by a

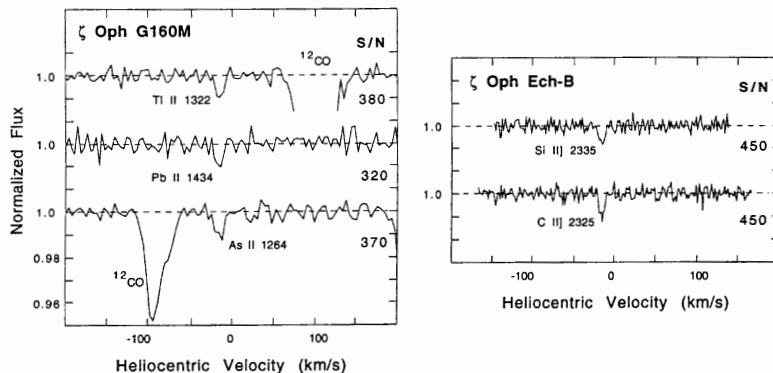


Figure 6: Selected examples of weak lines observed in high S/N Data of  $\zeta$  Oph using both G160M (with four samples/diodes) and Ech-B (with two samples/diode). The S/N values were empirically derived from the continuum and are consistent with what is expected from photon statistics. The data are taken from: Tl II and Pb II (Cardelli & Ebbets 1994); as II (Cardelli et al. 1993a); C II] (Cardelli et al. 1993b); Si II] (Cardelli et al. 1994).

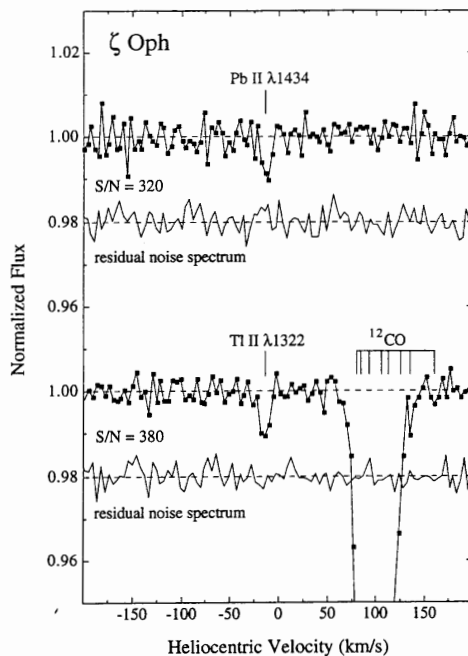


Figure 7: The weak lines of Tl II and Pb II observed toward  $\zeta$  Oph (Cardelli & Ebbets 1994). The data labeled residual noise spectrum were derived by taking the noise-corrected subexposures and running them through the noise extraction routines outlined in Figure 3 for the purpose of determining if residual noise structure is present. No such structure is present and the S/N of these data are the same as the reduced spectra which is essentially the same as that expected from photon statistics.

Gaussian distribution). As a start, we explore how well our noise extraction routines suppress the noise. An example is shown in Figure 7 for the weak line data of Tl II and Pb II obtained toward  $\zeta$  Oph (Cardelli & Ebbets 1994). The lower plot marked residual noise spectrum was determined by running the noise corrected subexposure back through the noise extraction routines outlined in Figure 3. Had our original noise template not sufficiently removed the noise structure (such as would be the case

for the data in Figure 5), we expect that some residual noise structure would be present. However, we see no evidence for this in the data. In fact, the empirical S/N measured in the residual noise spectrum is the same as that for the actual data. This result also gives us confidence that the features we observe are real.

A more definitive method is to explore the nature of the noise distribution about the fitted continuum. For this we use the  $\zeta$  Oph C II]  $\lambda$ 2325 Å data (Cardelli et al. 1993b) obtained with Ech-B. These data are particularly useful because the continuum in this spectral region is relatively flat and featureless which minimizes possible continuum fitting uncertainties. The distribution of the noise about the fitted continuum is shown in Figure 8. Also shown is a fit of a Gaussian function to the data. The Gaussian nature of the noise distribution coupled with the fact that the measure S/N is the same as that obtained from (total counts)<sup>1/2</sup> gives us confidence that the spectrum is dominated by photon noise. (A similar analysis of the data in Figure 7 yields similar results.)

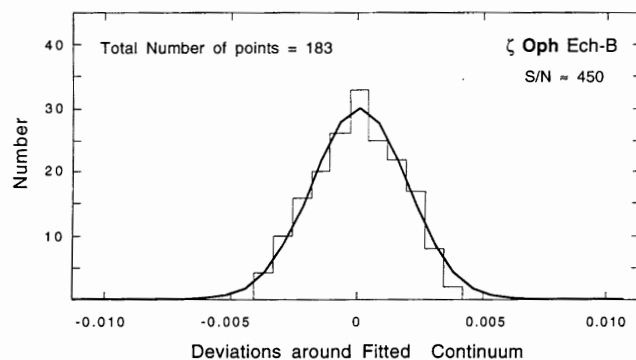


Figure 8: An example of the noise distribution about the fitted continuum of the noise-corrected C II]  $\lambda$ 2325 Å (Cardelli et al. 1993b) shown in Figure 6. As can be seen, the data are consistent with a Gaussian distribution indicating that the data are well represented by Poisson statistics. This quantitatively supports our contention that the empirically derived S/N is consistent with what is expected from photon statistics.

#### **IV. Recommendations**

The techniques outlined here have proven to be highly robust in a number of applications and numerous examples of high S/N results have been published. However, as shown in Figure 5, there are cases where problems do arise. If the desired goal of an observer is to obtain high S/N to measure weak lines or simply to obtain the best possible data, this will be best accomplished if some basic steps are followed. We therefore offer some suggestions and recommendations to ensure the best results.

- Always use the FP-SPLIT option, even if the expected S/N is relatively low. Some noise features are quite strong (see Figure 1) and could corrupt your data.
- Break an observation into multiple exposures to avoid serious data loss due to the possible consequences of orbital interrupts. This also decreases the photon noise contribution of the noise template relative to the individual subexposure.

- For high S/N work, also obtain multiple grating position observations at intervals of 0.5 – 1 Å using FP-SPLIT at each setup wavelength. This will give you a larger baseline from which to derive a noise template and will also increase the randomization of any residual noise features in the final merged spectrum.
- Try to limit the exposure time per readout to  $\leq 4$  minutes. This will decrease the chance of losing data to glitches and will lower the probability of problems associated with orbital interrupts. This also reduces the amount of smearing of the noise features due to Doppler compensation.
- Since the effects of orbital motion produce at most a maximum shift of 1 diode in the intermediate resolution modes, it may be useful to disable the Doppler compensator in the case of weak line work (i.e., where there is more interest in the measurement rather than the profile). This will eliminate the problem of noise feature drifts in pixel space. This is NOT recommended for observations obtained with the echelle modes.
- For intermediate resolution modes, the best results are obtained using STEP-PATT=5 (four samples per diode), especially for weak lines. For the echelle modes, two samples per diode (STEP-PATT=6) will suffice, but four samples per diode (STEP-PATT=7) should be obtained if time permits.
- Limit the smoothing of the noise template to  $\leq 1$  resolution element (one diode). While some smoothing may be necessary to minimize photon noise contributions relative to the individual subexposures, the noise features are not imaged by the gratings and so they are potentially resolvable on scales smaller than the resolution element. Too much smoothing can produce residual noise pings that can appear in the final merged spectrum.

## References

- Cardelli, J. A., & Ebbets, D. C. 1994, in preparation
- Cardelli, J. A., Federman, S. R., Lambert, D. L., & Theodosiou, C. E. 1993a, ApJ, 416, L41
- Cardelli, J. A., Mathis, J. S., Ebbets, D. C., & Savage, B. D. 1993b, ApJ, 402, L17
- Cardelli, J. A., Savage, B. D., & Ebbets, D. C. 1991, ApJ, 383, L23
- Cardelli, J. A., Sofia, U. J., Savage, B. D., Keenan, F. P., and Dufton, P. L. 1994, ApJ, in press.
- Federman, S. R., Sheffer, Y., Lambert, D. L., & Gilliland, R. L. 1993, ApJ, 413, L51
- Hobbs, L. M., Welty, D. E., Morton, D.C., Spitzer, L., & York, D. G. 1993, ApJ, 411, 750
- Lambert, D. L., Sheffer, Y., Gilliland, R. L., & Federman, S. R. 1994, ApJ, in press
- Sheffer, Y., Lambert, D. L., Federman, S. R., & Cardelli, J. A. 1992, ApJ, 397, 482

Editors' Note: A paper was also given by these authors, and presented by Dennis Ebbets, entitled "Calibration and Removal of Scattered Light in the Echelle Modes of the GHRS." A full description of the study appears in the following two published papers: Cardelli, Ebbets & Savage, 1990, ApJ, 365, 789; and Cardelli, Ebbets & Savage, 1993, ApJ, 413, 401.

# A Power Spectrum Method to Remove Fixed Pattern Noise From GHR Spectra

Cheng-Hsuan Lyu<sup>1</sup> and Fred C. Bruhweiler<sup>1</sup>

## Abstract

Recent high signal-to-noise spectra from the Goddard High Resolution Spectrograph (GHR) show a significant fixed pattern noise, including blemish and granularity functions, at up to a 30 percent level. We present a power spectrum method to remove this fixed pattern noise. This algorithm, together with the currently available GHR routines, has been applied successfully to remove the noise resulting from the defects and the nonuniform response in the photocathodes and diodes. We find a significant improvement in the signal-to-noise (S/N) ratio.

## I. The GHR Data

In order to reduce the effects due to the defects and the non-uniform response in the 500 science diodes (e.g. diode-to-diode gain variations) and the photocathodes, in the GHR observing mode, we use FP-SPLIT = 4 to make four independent exposures of the same spectral region. In each observation the carousel position moves and the spectrum shifts in the wavelength direction via a fixed diode spacing. This process can reduce the fixed pattern noise (blemish and granularity functions) in the co-added spectrum by at most a factor of 2. This improvement also applies to the random noise. Note that the blemishes are referred to as the noise with larger depth and/or wider profile (at least at the 5 percent level). In a recent observation in the line-of-sight toward  $\alpha$ Gru, the signal-to-noise is about 250. However, the fixed pattern noise is quite pronounced and serious (see Figure 1). It implies that the GHR data require more extensive data reduction. We need an efficient algorithm to remove this striking noise in our high signal-to-noise spectra.

## II. The Methodology

In order to remove the conspicuous FPN in the high S/N GHR data (see Figures 1 and 2), our algorithm is as follows:

- (a) Remove all the recognizable blemishes and interstellar lines in the GHR data. This is done by weighting these data points with zero values.
- (b) Interpolate across blemishes and interstellar lines with a spline or linear fit.

---

1. Physics Department, Catholic University of America, Washington DC 20064

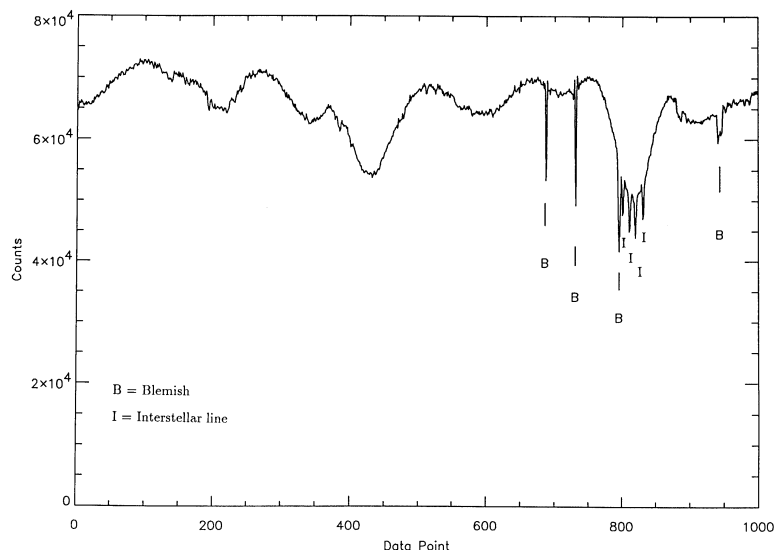


Figure 1: Enhanced fixed-pattern-noise (FPN) and obscured interstellar line(s) in high S/N GHR data. Since the FPN is fixed in the response of the photocathodes and diodes, when we co-add 4 FP-SPLITS in the pixel (or data point) domain directly, we see the enhanced FPN. In addition, among four independent observations (FP-SPLIT=4) of the same spectral region, each spectrum is shifted in the wavelength direction by a constant amount. Thus, in the co-added spectrum in the pixel domain we find that the interstellar lines (IS-lines) appear as four distinct features, separated by  $\sim 10$  data points.

(c) Apply Fast Fourier Transform (FFT) to filter out all the possible high frequency components that appear in the GHR data (see Figure 3). Then, transform the low-pass filtered data back to their pixel-space domain (see Figure 4).

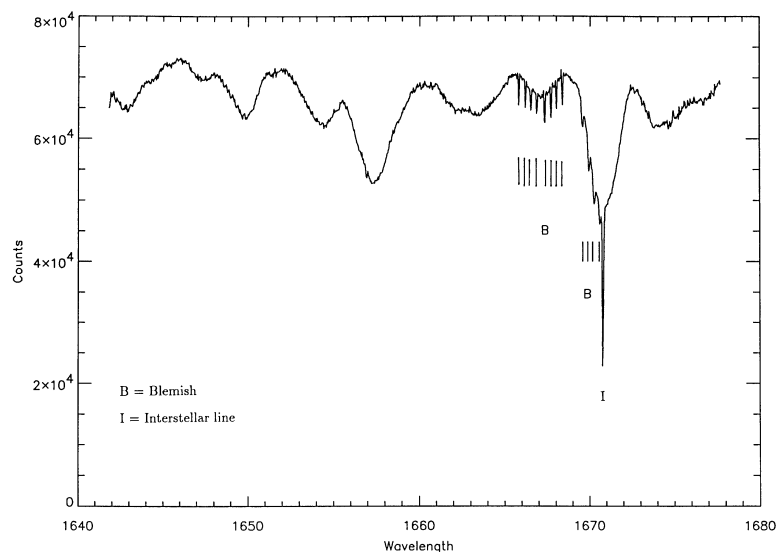


Figure 2: Merged GHR data with obscured FPN. Similar to Figure 1, but before co-adding four independent spectra we correct their respective shifts in pixel space; then we find sharp interstellar line(s), a series of blemishes, and the noise resulting mainly from granularity.

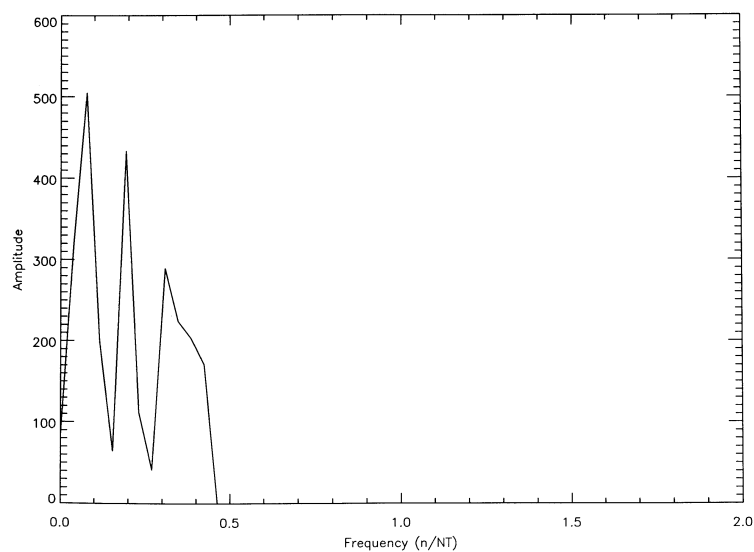


Figure 3: The power spectrum after applying FFT and clipping out high frequency components.

- (d) Use the co-added and enhanced FPN spectrum and the low-pass filtered data to determine the granularity function (see Figure 5). Then, divide the contaminated FP-SPLIT data by this function.
- (e) After correcting for FPN, the individual FP-SPLITS can be merged to yield the final and real high S/N data (see Figure 6).

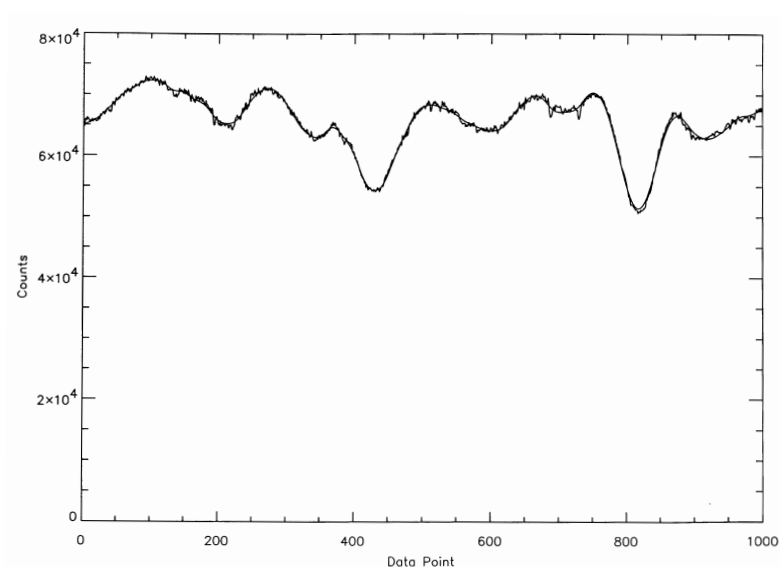


Figure 4: Low-pass filtered spectrum versus unsmoothed co-added spectrum in pixel space.

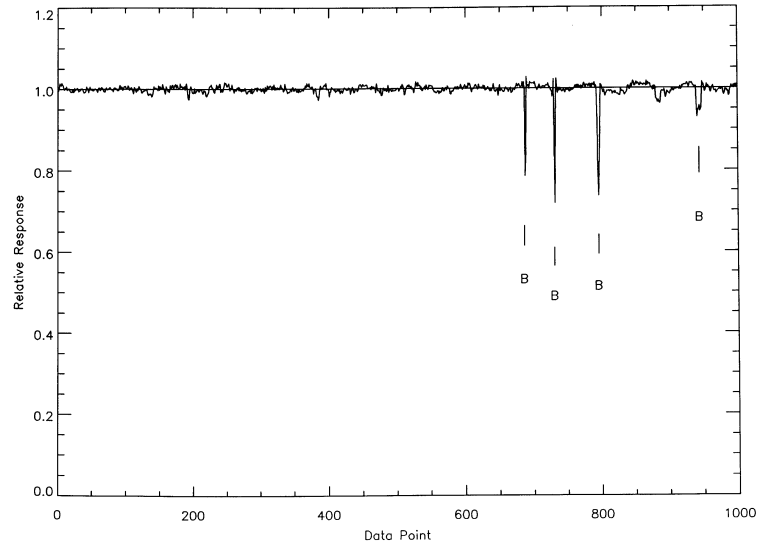


Figure 5: The extracted FPN (combined blemish and granularity functions) vector.

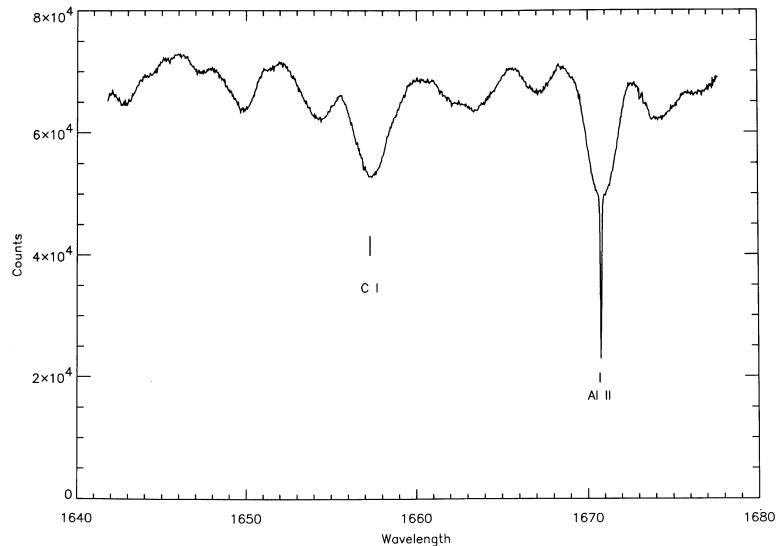


Figure 6: Final reduced corrected high S/N GHR data after taking out FPN. Comparing this spectrum with that in Figure 2, we find a significant improvement in S/N.

### **Concluding Remarks**

Comparing our final reduced data (Figure 6) with the contaminated spectrum (Figure 2), one finds a significant improvement in S/N in our GHR data. This appears to recover the Poisson limited signal-to-noise ratio ( $S/N = 1/\sigma$ ). Besides, our algorithm is very efficient, for we don't need to do an iterative solution as in the case of the so-called tomographic technique (Gilliland 1993, personal communication) and iterative method (Lindler 1993, personal communication). This methodology, however, is limited to stars with large  $v \sin i$ . Stars with low  $v \sin i$  will have larger contributions at high frequencies in the FFT. In any event, one must still inspect each subexposure separately to make certain that we have treated properly all features, both in the source and FPN spectra.

# **An Evaluation of the Performance of SSA ACQ/PEAKUPs<sup>1</sup>**

Stephen J. Hulbert<sup>2</sup> and Wayne E. Baggett<sup>2</sup>

## **Abstract**

This report examines the results of seventeen SSA ACQ/PEAKUP observations executed between 30 June 1993 and 22 October 1993. The SSA ACQ/PEAKUPs using MIRROR-A2 appear to be working well. However, the ACQ/PEAKUPs with MIRROR-N2 show a systematic offset in the final target placement that will be corrected with a change to the PDB aperture center coordinates for this mirror.

## **I. Introduction**

### **SSA ACQ/PEAKUP**

The SSA ACQ/PEAKUP provides GHRS with the means to position a target in the center of the small science aperture (SSA). The original algorithm for accomplishing this centering or “locating” was rendered unusable by the aberrated point spread function. The algorithm was converted to use the technique employed in searching for targets in the large science aperture (LSA). Here, a section of the sky is scanned using a spiral-search pattern that involves moving the telescope through a series of prescribed slews. The telescope finally returns to the dwell point having the greatest flux. In the case of the SSA implementation these slews are about one-quarter of the size of the SSA (0.06 arcsec). The default 3×3 spiral search used for the SSA PEAKUP covers an area approximately 0.37 arcsec by 0.37 arcsec. Consequently, if the initial slew to the SSA puts the target in the SSA, the default PEAKUP should place the target within 0.06 arcsec of the center of the aperture.

### **Preliminary Work on Feasibility of SSA ACQ/PEAKUP**

The Instrument Science Report, GHRS ISR-044, “SSA Spiral Search Tests Results for Centering and Throughput”, described the results of GHRS/CAL programs 3999 and 4462. These tests used MIRROR-A2 and grating G160M to investigate how well we were centering objects in the SSA and how to improve this centering. We found that we were systematically not centering targets in the SSA, having first done an ACQ in the LSA with MIRROR-A2 followed by a blind slew to the SSA. Analyses led to two updates to the PDB for PTLD.DAT tables ZFDEFXNC and ZFDEFYNC which control where a target is centered in the LSA. By tweaking this we control where the subsequent slew to the SSA places that target. A total change of (–1, –5) deflections

1. Originally published as GHRS Instrument Science Report #56.

2. Space Telescope Science Institute, Baltimore, MD 21218

units, corresponding to a change with an absolute value of (0.03, 0.155) arcsec, was made to improve the placement of a MIRROR-A2 acquired object in the SSA.

These tests compared count rates in the LSA with count rates at various points in and about the SSA. Maximum SSA/LSA ratios were found to be about 0.65 for MIRROR-A2 and 0.31 for G160M. Interestingly, the centers were found to differ on the order 0.06 arcsec for MIRROR-A2 and grating G160M. The SSA/LSA ratio for MIRROR-A2 is thought to be high because of the interplay between the shape of the mirror and the sizes of the apertures—the mirror picks off only part of PSF from the LSA; the SSA passes only the central portion of the PSF and subsequently most of this beam is picked up by MIRROR-A2.

### **Failure of First SSA ACQ/PEAKUP Test**

The commanding capability for the use of ACQ/PEAKUPs in the SSA was first tested in June 1993. This first test failed. The nature of the failure was not in the PEAKUP algorithm; we were able to verify that the spiral search was conducted and that the telescope then slewed to the point of greatest flux. The specific problem experienced was that the GHRS was “looking” at the LSA during the SSA procedure. A work-around for this problem was quickly implemented by SESD and subsequently, a more robust solution was implemented. A follow-up to this test was built into the system as a backup. Unfortunately, this test executed prior to the time the work-around was installed. The details of the first test can be found in GHRS ISR-050.

## **II. Data**

Since the end of June 1993 a total of seventeen SSA ACQ/PEAKUPs have executed. Tables 1 and 2 contain a collection of data for 17 pairs of observations: each pair consists of an ONBOARD ACQ in the LSA and an ACQ/PEAKUP in the SSA that executed immediately after the ACQ. Table 1 contains data for observations using MIRROR-N2; Table 2 contains data for observations using MIRROR-A2. Relevant quantities cataloged in these tables are:

- Date of Observation—given as dd/mm/yy
- Observation—the ROOTNAME of the observation
- APERTURE—SSA or LSA
- MAPFND—the map number in which the target was found
- FLUXFND—the flux measurement for the map in which the target was found measured in counts
- ZFLUXM—the flux measurement taken at the conclusion of the acquisition procedure (for both the ACQ and ACQ/PEAKUP) measured in counts. This quantity should be the same as FLUXFND in the SSA case but may be different in the LSA case as the LSA ACQ performs additional centering after finding the target.
- STEPTIME—the exposure time at each dwell point of the spiral search in seconds
- Count Rate—the ratio of the ZFLUXM / STEPTIME in units of counts/s.

**Table 1: LSA ACQ—SSA ACQ/PEAKUP Observation Pairs Using MIRROR-N2**

Observation Date (dd/mm/yy)	Observation	APERTURE	MAPFND	FLUXFND (counts)	ZFLUXM (counts)	STEPTIME (sec)	Count Rate (c/s)
30/06/93	z1e20402t	LSA	1	5775	6237	0.2	31185
	z1e20404t	SSA	9	1437	1419	0.3	4730
30/06/93	z1gx0402t	LSA	6	8235	9295	0.2	46475
	z1gx0404t	SSA	9	15534	16950	1.6	10594
14/09/93	z1gt0102t	LSA	2	10186	15550	0.2	77750
	z1gt0104t	SSA	9	4558	4468	0.2	22340
15/09/93	z1gv0702t	LSA	2	15740	23478	0.3	78260
	z1gv0704t	SSA	9	47133	47249	1.6	29531
18/09/93	z1gu0602t	LSA	2	11189	15679	0.2	78395
	z1gu0604t	SSA	9	4283	4353	0.2	21765
18/09/93	z1gv0b02t	LSA	2	15375	22157	0.3	73857
	z1gv0b04t	SSA	9	17891	17332	1.6	10832
19/09/93	z1gv0102t	LSA	2	18758	24767	0.3	82557
	z1gv0104t	SSA	9	47361	46936	1.6	29335
21/09/93	z1gu0402t	LSA	2	12264	15627	0.2	78135
	z1gu0404t	SSA	9	5835	5954	0.2	29770
27/09/93	z1kz0502t	LSA	2	84564	91904	3.2	28720
	z1kz0504t	SSA	9	2270	2279	0.4	5698
06/10/93	z1kj0302t	LSA	1	5639	5614	0.2	28070
	z1kj0304t	SSA	9	8563	7980	1.6	4988
08/10/93	z1kj0102p	LSA	1	5558	5852	0.2	29260
	z1kj0104p	SSA	9	12969	13322	1.6	8326
08/10/93	z1kj0702p	LSA	1	4850	6021	0.2	30105
	z1kj0704p	SSA	9	13155	13268	1.6	8292
10/10/93	z1kj0502t	LSA	1	5662	5884	0.2	29420
	z1kj0504t	SSA	9	10184	9934	1.6	6209

**Table 2: LSA ACQ—ACQ/PEAKUP Observation Pairs Using MIRROR-A2**

Observation Date (dd/mm/yy)	Observation	APERTURE	MAPFND	FLUXFND (counts)	ZFLUXM (counts)	STEPTIME (sec)	Count Rate (c/s)
23/07/93	z1f40102t	LSA	6	4504	4564	2.75	1660
	z1f40104t	SSA	9	4042	3980	2.75	1447
09/08/93	z1hy0102t	LSA	1	1819	1786	0.2	8930
	z1hy0104t	SSA	8	1628	1613	0.2	8065
27/08/93	z1ix0102t	LSA	1	2030	2246	0.2	11230
	z1ix0104t	SSA	2	15257	14797	1.6	9248
22/10/93	z1ha0202t	LSA	1	8097	8874	0.2	44370
	z1ha0204t	SSA	3	7451	7008	0.2	35040

### III. Analysis

Table 3 contains the following:

- MIRROR—N2 or A2
- Observation—the ROOTNAME of the SSA ACQ/PEAKUP observation
- MAPFND—the map number in which the target was found
- SSA/LSA Ratio—the ratio of the SSA Count Rate (from Table 2) to the LSA Count Rate (from Table 1)

Examination of Table 3 shows a scatter of map numbers in which the target was located for MIRROR-A2. As mentioned before, the default SSA ACQ/PEAKUP covers an area of 0.37 arcsec by 0.37 arcsec. Except for the case where the object is exactly centered in the SSA after the slew, we would expect to find the object at the “edge” of our search. It appears then that MIRROR-A2 is successfully centering the target in the SSA.

**Table 3: SSA ACQ/PEAKUP Observations**

MIRROR	Observation	MAPFND	SSA/LSA Ratio	
A2	z1f40104t	9	0.87	
	z1hy0104t	8	0.90	
	z1ix0104t	2	0.82	
	z1ha0204t	3	0.79	
	Average		0.84	
	Standard Deviation		0.05	
N2	z1e20404t	9	0.15	
	z1gt0104t	9	0.29	
	z1gu0404t	9	0.38	
	z1gu0604t	9	0.28	
	z1gv0104t	9	0.36	
	z1gv0704t	9	0.38	
	z1gv0b04t	9	0.15	
	z1gx0404t	9	0.23	
	z1kj0104p	9	0.28	
	z1kj0304t	9	0.18	
	z1kj0504t	9	0.21	
	z1kj0704p	9	0.28	
	z1kz0504t	9	0.20	
		Average		0.28
		Standard Deviation		0.09

In the case of MIRROR-N2, however, the target was located in map #9 in every instance. Clearly something is not quite right for this mirror. It is important to keep in mind the iterative process that took place in the preliminary work on the SSA AQC/PEAUP described in section 1.3. Recall that this work resulted in improved centering for MIRROR-A2 but that MIRROR-N2 was not examined (due to lack of data). It appears appropriate at this time to undertake a similar iterative process to improve centering with MIRROR-N2. Figure 1 shows that the map #9 position is in the positive x- and y-directions. As the step sizes are 0.06 arcsecs this is approximately equal to 2 deflection steps in each direction. We can accomplish an offset to compensate for this by initially centering somewhat “off-center” in the LSA.

Since we always find the target off in the positive directions we will want to initially center in the LSA in the same direction. Following the successful prescription of the previous work on MIRROR-A2 we should adjust the centering of the target in the LSA by about +0.06 arcsec in both the x- and y-directions. Figure 1 shows the coordinate system in which the spiral search is made. The numbers in the circles indicate the sequence of dwell points.

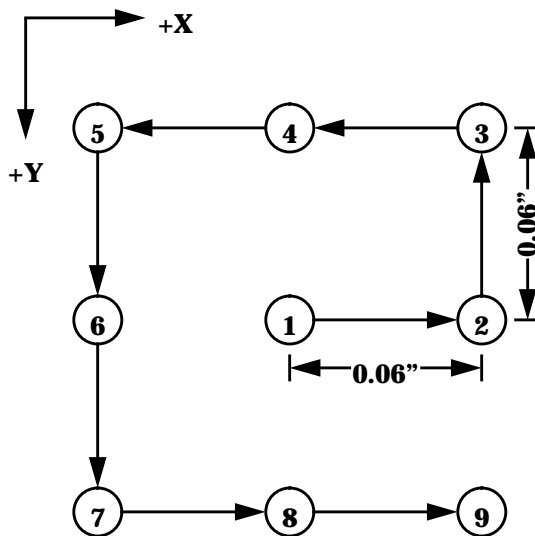


Figure 1: Default SSA spiral search geometry.

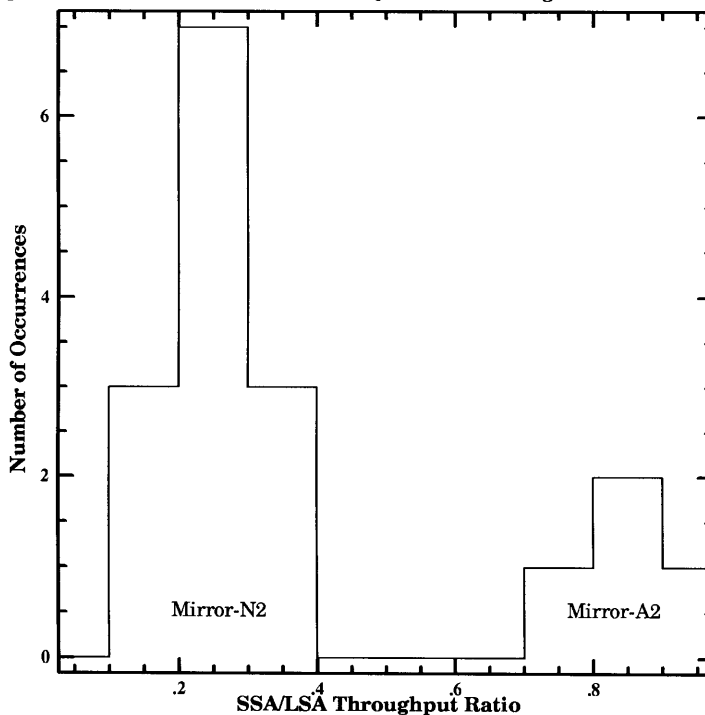


Figure 2: SSA/LSA Ratios for SSA ACQ/PEAKUPS using Mirrors-A2 and -N2

Further examination of Table 3 shows that the throughput ratios for MIRROR-A2 are on average equal to 0.80—previous work on this mirror had shown a maximum ratio of 0.65. It appears that the current SSA ACQ/PEAKUP is doing a better job at centering targets in the SSA than the previous analysis had led us to expect. The SSA/LSA ratio for MIRROR-N2 averages 0.26. At this time it is not possible to evaluate this ratio since we have already concluded that we are not producing an optimum centering using MIRROR-N2. Figure 2 shows the distribution of SSA/LSA throughput ratios for all of the SSA ACQ/PEAKUPS in Table 3.

#### **IV. Conclusion**

The SSA ACQ/PEAKUP using MIRROR-A2 is working well. However, analysis of the MIRROR-N2 data indicates that a change must be made in the centering of objects in the LSA prior to slewing to the SSA when using this mirror. Consequently, we will initiate a PDB-change request to modify the PTL.DAT file. For MIRROR-N2 we will change both ZFDEFXNC and ZFDEFYNC by +2 deflection steps. These changes will compensate for the offset in (x, y) of (+0.0625, +0.0625) arcsecs (equal to an offset in (U2,U3) of (0, +0.088) arcsecs). Until we can demonstrate that this change will improve the centering we recommend the use of a 5x5 spiral search when using MIRROR-N2 to do an SSA ACQ/PEAKUP.